Study of effect of processes on microstructure and precipitation in age-hardenable aluminum alloys

時効硬化型アルミニウム合金のミクロ組織と析出に及ぼす種々の工程の影響に関する研究

Table of contents

1. Introduction

1.1 Age hardenable aluminum alloys

Aluminum alloys belong to the group of the most used metals in our daily lives and also many applications in industry due to the low density and good mechanical properties. Pure aluminum is very soft and lacking in strength, its application is largely limited to packaging and foil, electronic conductors [1]. In order to make use of aluminum as construction materials or in application as an engineering material for lightweight constructions, the strength of the Al-based materials must be increased [1,2]. It is well known that the pure aluminum can be strengthened by four physical mechanisms: (1) dislocations (work hardening); (2) grain boundaries; (3) alloying elements in solid solution; (4) precipitation hardening [2,3]. All the four mechanisms that can increase the strength are based on the effect of hindering dislocations from gilding.

Solute elements are usually added to the pure aluminum and make it gain age-hardenability, these alloys can achieve their highest strengths by heat treatment to promote precipitation of the major alloying elements. the formation of a large amount of dispersed nanometre-scaled precipitates during aging treatment can effectively impede the moving dislocations [4]. With the Mg and Si addition, Al-Mg-Si alloys are an important class for structural applications due to the combination of medium strength, good formability and corrosion resistance. At the same time, as the lightest metal found in the nature, lithium addition to aluminium alloy can reduce the density and also make the aluminum heat treatable, Al-Li alloys are attractive especially for aerospace applications, because they offer interesting combinations of high specific strength and

high specific modulus [5]. For the Al-Li alloys, Mg and Cu are usually added for getting higher strength.

1.2 Precipitation during heat treatment in age hardenable alloys

As a heat treatable alloy, to maximize strength, the heat treatment of the Al-Mg-Si alloys mainly consists of three stages: (1) a solution treatment at elevated temperature, (2) quenching to room temperature, and (3) an aging treatment at lower temperature (170°C-200°C). During aging treatment, the precipitation development from the super saturated solid solution (SSSS) and till the equilibrium phase forms is given as a precipitation sequence, the precipitation sequence of the metastable phase depends on the content of the Mg and Si in the alloy as follows [6-15]:

In the case of Mg/Si > 2,

Atomic clusters → GP zones → β″ → β′→ β.

In the case of Mg/Si < 2,

Atomic clusters → GP zones → β″ → β′, Type-A, Type-B, Type-C → β, Si. (Type-A, Type-B, Type-C also called U1, U2 and B', respectively).

All the metastable precipitates in the Al-Mg-Si alloys have needle/lath/rod morphologies with longest dimension oriented along $<100>_{Al}$ directions, in which the precipitates are fully coherent with the matrix [9]. Among them, β″ is the main phase that forms in the peak aged condition of the Al-Mg-Si alloys. The coarse β′ phase generally appear after over aging, associated with a decrease in hardness. With the excess of Si, in addition to β′, Type-A, Type-B and Type-C also appear in the matrix of over-aged condition [12]. Since the precipitates of Type-A, Type-B and Type-C in the excess Si

alloys have a similar morphology as the β′ phase, all these precipitates were considered as β′ phase before 1995 [13].

The Al-Li alloys have been strengthened by dispersion of fine precipitates. The precipitation sequence of the Al-Li alloys is reported as follows [16]:

$$SSSS \rightarrow \delta' (Al_3Li) \rightarrow \delta (AlLi)$$

In Al-Li alloys, Mg addition enhances the precipitation of δ' phase due to Mg lowers the solubility of Li in the α-Al solid solution and incorporates into the δ' phase itself [17], two phases are known in Al-Li-Mg alloy, δ' phase and equilibrium cubic S_1 phase (Al_2MgLi) [18,19]. Furthermore, the addition of Cu leads to precipitates, T_1 (Al_2CuLi) and θ' (Al_2Cu) phases. It is known that δ', T_1 and θ' precipitates are responsible for the strengthening of Al-Li alloys [20]. Silcock firstly identified T_1 phase as an important constituent in the Al-Li-Cu system and verified the orientation relationship as (0001)//(111); T_1 phase is generally consider as hexagonal, of symmetry P6/mm, and forms as platelets on the {111}Al planes of the matrix with a unit cell of dimensions a=b=4.95Å and c=9.327Å [21].

In addition to aging treatment, homogenization is also a process where precipitation may take place. In industry, the applications of Al-Mg-Si alloys can be found in rolled products and extrusions. Many complex components, i.e, door pillars and door sills, are produced using extrusion as the main manufacturing method. The general processing sequence for the Al-Mg-Si alloys involves casting, homogenization, billet re-heating, high temperature extrusion, solution heat treatment (optional for many Al-Mg-Si serious alloys) and artificial aging [22].

Homogenization is an essential process in extrusion technology of the Al-Mg-Si alloys, because homogenization can reduce the chemical segregation of the cast. During homogenization cooling, the precipitates may also form in the matrix, controlling precipitation behaviour during cooling stage is important, because the shape and size of the precipitates can affect the subsequent processing [23]. Thus, controlling precipitation is important to the extrudability or even the final mechanical properties.

Homogeneous precipitation during homogenization cooling has been extensively studied in the Al-Mg-Si alloys, one of the most important processes which takes place during homogenization is the dissolution of Mg-Si particles. The dissolution of Mg-Si particles can increase the Mg and Si content of the matrix, Furthermore, during cooling after homogenization Mg–Si precipitates may form again, which decreases the Mg and Si solute content [24-27]. Compared to isothermal aging treatment, the homogeneous nucleation of equilibrium phases or over-aged phase are easy during homogenization cooling. The type and dimension of the precipitates depend on the chemistry of the alloy and the cooling rate, there are many papers focused on the effect of cooling rate on the precipitation process during homogenization cooling.

Milkereit et al. used five kinds of excess Si type Al-Mg-Si alloys to investigated how the cooling rate affect the precipitation by means of differential scanning calorimetry (DSC), all the investigated alloys shown similar precipitation behavior, which consists of the high-temperature precipitation of at least the Mg_2Si and the low-temperature precipitation of presumably β' and/or B' (Type-C) [24]. Zajac et.al investigated the influence of homogenization cooling rate on the microstructure and extrudability of AA6082 and AA6063 alloys, his results have shown that the equilibrium fcc β-Mg_2Si

precipitates when the cooling temperature after homogenization is above 400 °C and hexagonal β′ at lower temperatures [25]. They concluded that billets with the β′ particles, which form at lower temperatures, give low flow stress at extrusion temperature. Also, step -cooling was proposed to suppress the formation of stable β phase, and instead produce the metastable β′ platelets. Birol has carried out a series of work to study the effect of cooling rate on precipitation during homogenization cooling in Al-Mg-Si alloys. His results shown that the β and β′ phase were the main precipitates formed during homogenization cooling and their amount increased with decreasing the cooling rate [26-28]. Du et al. also proposed a model to predict the competitive nucleation and growth of the β and β′ particles during homogenization cooling process, the model predictions are in good agreement with the microstructure characterization results in the AA6082 and AA6061 alloys [29]. As written above, under over-aged condition of the excess Si type Al-Mg-Si alloys, except β′, Type-A, Type-B and Type-C also exist and exhibit rod/lath-shape in the matrix, in addition, some of the Si phase can also exhibit a similar shape. Thus, it is difficult to distinguish these precipitates by shape. However, until now, all the precipitates in the published papers are characterized by indirect methods, i.e. DSC, XRD or even the shape, there is no directly characterization or observations of the type of the precipitates.

Although homogeneous precipitation during homogenization cooling has been extensively studied, the heterogeneous precipitation behavior is still unclear, especially when the precipitates nucleate on the dislocations, which forms during homogenization cooling. Actually, in the work of Birol [26-28], many “boundaries” frequently appeared within the grains in his samples, especially when the cooling rate was higher than 200 °C/h [27], however, there is no reports about this phenomenon. At the same time, how the

cooling rate and different precipitates formed during homogenization cooling affect the final properties are not fully understood. At the same time, many papers focused on the effect of homogenization on the extrudability, few reports about how homogenization affect the microstructure and precipitation during final aging treatment.

1.3 Precipitation during aging treatment with deformation induced strains

In industrial practice, the products often have to experience a certain degree of deformation, such as straightening and forming, before final aging treatment, in this case, low amount of strains are introduced into the matrix. Meanwhile, unlike the non-heat-treatable Al-Mg and Al-Mn alloys, which are strengthened mainly by working them at room temperature to induce strain hardening. The strength of the heat-treatable alloys may be increased by combination of strain hardening (grain refinement) and precipitation hardening. With increasing the strains, the microstructure evolution of the pure aluminum was shown in Fig. 1, It can be seen that the microstructure follows: (1) dislocation accumulation occurs, (2) sub-grain boundaries form, (3) some dislocations are annihilated at sub-grain boundaries to increase the misorientation angels and (4) finally balance is established between generation of dislocations and absorption of dislocations at grain boundaries [30].

Following solution treatment, deformation introduced strains has a strong effect on precipitation behavior during final aging treatment. With low amount of strains, the aging behavior with the presence of dislocations has been investigated extensively. It is generally accepted that the introduced dislocations can provide heterogeneous nucleation sites that may change the precipitation kinetics and the precipitation sequence. Matsuda et.al showed for the first time that in the presence of dislocations, a string-like precipitate,

together with an elongated type and Type-C precipitates, are formed along the dislocation [31,32]. Yassar et.al investigated the precipitation behavior of a 6022 alloy during differential scanning calorimetry experiments by TEM. It was also shown that the β″ phase is not formed in the presence of dislocations [33]. Teichmann et.al reported that the introduced dislocations prior to aging has a profound effect on the precipitation behavior, the microstructure, local distribution and type of the precipitates are altered. Under peak aged conditions, the precipitates type changes from predominantly β″ in the undeformed samples to over aged precipitates in the pre-deformed samples [34]. Lai et.al concluded that when the slight deformed Al-Mg-Si alloys aged at 250°C, the majority of the dislocations-induced complex precipitates are multiphase composite precipitates, including polycrystalline U2 precipitates, B′/U2 and β′/U2. Also, they explained the parallel growth of the precipitates is owing to the that all the nuclei orient their easy-growing directions parallel to the associated dislocation lines[35].

With high strains introduced by severe plastic deformation (SPD), the Al-Mg-Si alloys exhibit reduced aging hardenings or significant age softening. Hirosawa et.al concluded that the cold rolled and HPT processed 6022Al-Mg-Si alloy exhibits reduced aging hardenings or significant age softening, failing to take advantage of the excellent age-hardenability of this alloy. This is because heterogeneous nucleation of coarsened over-aged precipitates becomes predominant at dislocations and grain boundaries in place of the main strengthening β″ phase [36].

Above all, for the Al-Mg-Si alloys, the age-hardenability reduces under different strains due to the lack of strengthening phase β″ and the over-aged precipitates can easily nucleate at dislocations or grain boundaries. At the same time, the distribution of the

needle/rod shaped precipitates along the dislocation is altered, the precipitates form along the dislocations tend to line up and parallel to each other.

For the Al-Li-(Cu, Mg) alloys, deformation has a different effect on the precipitation behaviors. Adamczyk et.al reported that the equal channel angular extrusion (ECAP) and hydrostatic extrusion (HE) processed binary Al-Li alloy cannot be strengthened by aging treatment, even the aging temperature is 100°C [37]. However, with the Cu addition, deformation is usually introduced due to the nucleation of T_1 precipitates strongly depends on the application of plastic deformation prior to ageing [38]. More recently, the combined processing of SPD and aging treatment for strengthening the 2091 Al-Li alloys has been achieved [36,39]. When the 2091 alloy process by HPT, a further increase in hardness was achieved by aging the alloys at 100°C and 150°C, however, the effect of Cu and Mg is still unclear during aging treatment under SPD condition.

In this study, following solution heat treatment, conventional cold rolling (CR), asymmetric rolling (ASR) and High-pressure torsion (HPT) are used to introduce low, middle and high amount of strains. As shown in Table 1, the diameter of the rollers is the same under the conventional cold rolling condition. For producing large-scaled sheets or plates with good mechanical properties, ASR has been proposed by Buxton and Browningt in 1972 [40]. The schematic illustration of ASR is shown in Table 1. In ASR, the peripheral speeds of the two rolls at the contact surface are different, consequently the material is exposed to an extra shear deformation in addition to the compression deformation. Under the same rolling reduction, the effective plastic strains reached by ASR are larger than those obtained by CR, thus the ASR process could refine the grains [41]. Among SPD processes, HPT is popular because it can continuously introduce a large

amount of strain into material. The first concept of HPT was introduced by P. W. Bridgman in 1935 [42]. And, HPT have much attention during last 3 decades because of its excellent grain refinement ability, HPT is a powerful method for grain refinement of metallic materials, hard-to deform materials, ceramics and intermetallic materials [43-50]. The schematic illustration of HPT is shown in Table 1 and equivalent strain (ε) is calculated by quoted equation (2).

In this work, ASR were adopted to introduce middle amount of strains to the Al-Mg-Si alloy, the effect of ASR on microstructure and precipitation behaviours was studied. At the same time, in order to compare the effect of deformation on microstructure and aging behaviors in different age-hardenable alloys, Al-Li-(Cu, Mg) alloys were used due to lithium addition to aluminium reduces the density, and makes the aluminum obtain combinations of high specific strength and high specific modulus. In previous studies, the combined processing of SPD and aging treatment for strengthening the 2091 Al-Li alloys has been achieved, however, the effect of Cu and Mg is still unclear under SPD conditions. In the present work, except ASR, conventional CR and HPT were also used to introduce low and high amount of strains to the Al-Li alloys, the effect of deformation on microstructure and aging behavior of the Al-Li-(Cu, Mg) alloys was investigated.

1.4 Objectives

The aim of this work is to study the effect of different processes on microstructure and precipitation in age-hardenable aluminum alloys. Firstly, the effect of homogenization cooling rate on the microstructure and precipitation behavior after homogenization, extrusion and solution treatment was investigated in the Al-Mg-Si alloys; Second, following solution treatment, the effect of deformation on microstructure and

precipitation behaviors during aging treatment in Al-Mg-Si alloys was studied. To compare and better understand the effect of deformation on aging behavior in different age-hardenable alloys, in addition to Al-Mg-Si alloys, Al-Li-(Cu, Mg) alloys were also used.

The objectives of this work are the following:

(1) To investigate both the homogeneous and heterogenous precipitation behavior of the Al-Mg-Si alloys during homogenization cooling stage, especially try to clarify what causes the formation of “boundaries” inside the grains during homogenization cooling stage.

(2) To investigate the effect of homogenization on the microstructure and precipitation after extrusion, solution treatment and during aging treatment in the balanced and excess Si type Al-Mg-Si alloys.

(3) To study how the strain introduced by deformation affects the microstructure and precipitation behavior during aging treatment in the Al-Mg-Si and Al-Li-(Cu, Mg) alloys. Also, to classify the effect of Cu and Mg on the microstructure and aging behaviors of the Al-Li alloys under different strains.

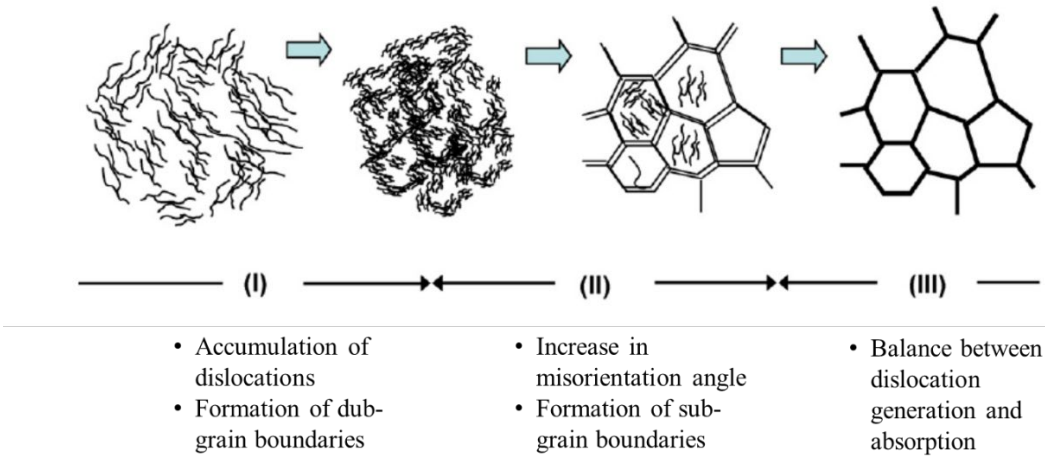

Fig. 1 Schematic illustration of microstructural evolution with straining of pure aluminum. Thin double lines represent low angle boundaries with some extension of boundary width and thick lines in region III represent high angle boundaries.

Cold rolling (CR)	Asymmetric rolling (ASR)	High-pressure torsion (HPT)
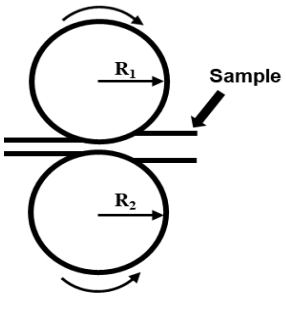	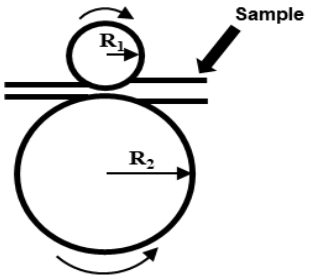	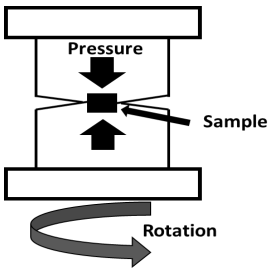
$R_2/R_1=1$	$R_2/R_1=2.4$	
$\varepsilon = -\frac{2}{\sqrt{3}}\ln\frac{h}{h_0}$	Equation 1	$\varepsilon = \frac{2\pi rN}{\sqrt{3}h}$

Table 1 Schematic illustrations of deformation methods

2. Methodology

2.1 Materials and heat treatments

The composition of the used alloys is shown in Table 1, all the alloys were prepared by laboratory casting. Two different Al-Mg-Si alloys with the composition of Al-0.31Mg-0.68Si wt% (excess Si type) and Al-0.64Mg-0.32Si wt% (balanced alloy) were used in this work. The diameter of the Al-Mg-Si billets is 4 cm. The composition of the Al-Li, Al-Li-Cu and Al-Li-Mg alloys is also shown in Table 1.

For the Al-Mg-Si alloys, after casting, the heat treatment processes were shown in Fig. 2. The Al-Mg-Si samples for homogenization cooling experiments were cut from the cast billets with a length of 5 cm, then the samples were divided into three groups. The first group was extruded directly. The samples for homogenization experiments were homogenized at 575 ^{o}C for 2 h. After that, the samples were cooled in the air and furnace, respectively. The cooling rate in the furnace was 20 ^{o}C/h (~0.33 ^{o}C/s) and the furnace-cooling process was stopped when the temperature decreased to 200 ^{o}C. For the samples cooled in the air, the cooling rate was about 830 ^{o}C/h (~14 ^{o}C/s). To investigate how the precipitates form during homogenization cooling stage, the samples were taken out the furnace and quenched into water at the temperature. As shown in Fig. 3, after holding at 575 ^{o}C for 2 h, the first group samples were taken out the furnace and quenched into water directly. Then, as the temperature decreased to 450 ^{o}C and 350 ^{o}C, the other two group samples were also taken out of the furnace, respectively.

After homogenization, the billets were re-heated to 405 ^{o}C, then the billets were extruded to sheets with a cross section of thickness of 15 mm wide and 1.5 mm thick. The

	Li (wt%)	Cu (wt%)	Mg (wt%)	Si (wt%)	Al
Al-Mg-Si(excess Si)	-	-	0.31	0.68	Bal.
Al-Mg-Si(Balance)	-	-	0.64	0.32	Bal.
Al-Li	2.7	-	-	-	Bal.
Al-Li-Cu	2.5	2	-	-	Bal.
Al-Li-Mg	2.7	-	1.9	-	Bal.

Table 2 Chemical composition of the used alloys

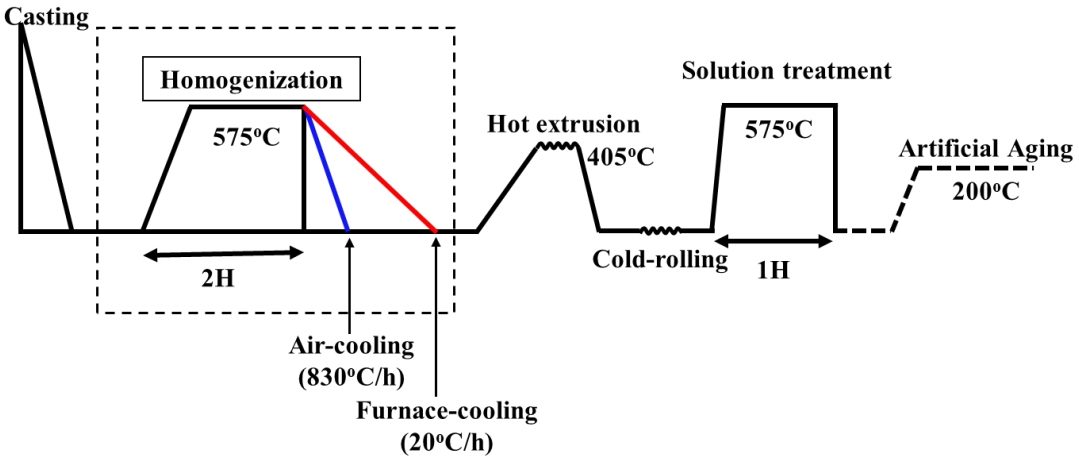

Fig. 2 Schematic showing the various processing stages for the Al-Mg-Si alloys studied in this work.

samples were heated up to 575 ºC and hold at this temperature for 1 H to achieve a single phase, then, the samples were quenched in chilled water. The aging treatment was performed at 200 ºC in an oil bath. For TEM observation, the sheets after hot extrusion was cold rolled to 0.2 mm.

2.2 Deformation and aging treatment

The samples of the Al-Mg-Si alloys for ASR experiment was cut from the as-cast billets. The dimension of the samples is 60×20×6 mm. Before ASR, the samples were solution treatment at 575 ºC for 1 h, then, the samples were rolled at room temperature with a thickness reduction of 30%, 50% and 80%. Aging treatment was performed at 150 ºC and 200 ºC.

For the Al-Li-(Cu, Mg) alloys, before deformation, all the Al-Li, Al-Li-Mg and Al-Li-Cu alloys were solution treated at 560 ºC for 1 h and quenched in water. Deformation and heat treatment conditions are shown in Table 3. ASR was carried out using different roll diameters with the ratio of 2.4, Samples with a dimension of 60×20×6mm was rolled several times to about 60% thick reduction at room temperature, approximately reduction in thickness of 10% was given to the sample through every pass. The thickness of the Al-Li alloy was reduced from 6 mm to 2.2 mm after six passes, for the Al-Li-Cu and Al-Li-Mg alloy, the thickness of the sheet was reduced from 6mm to 2.65 and 2.45 mm, respectively. As shown in Table 3, the ASR was stopped at different thickness reduction in order to avoid cracks. The ε was calculated using the follow eq (1) [51,52]:

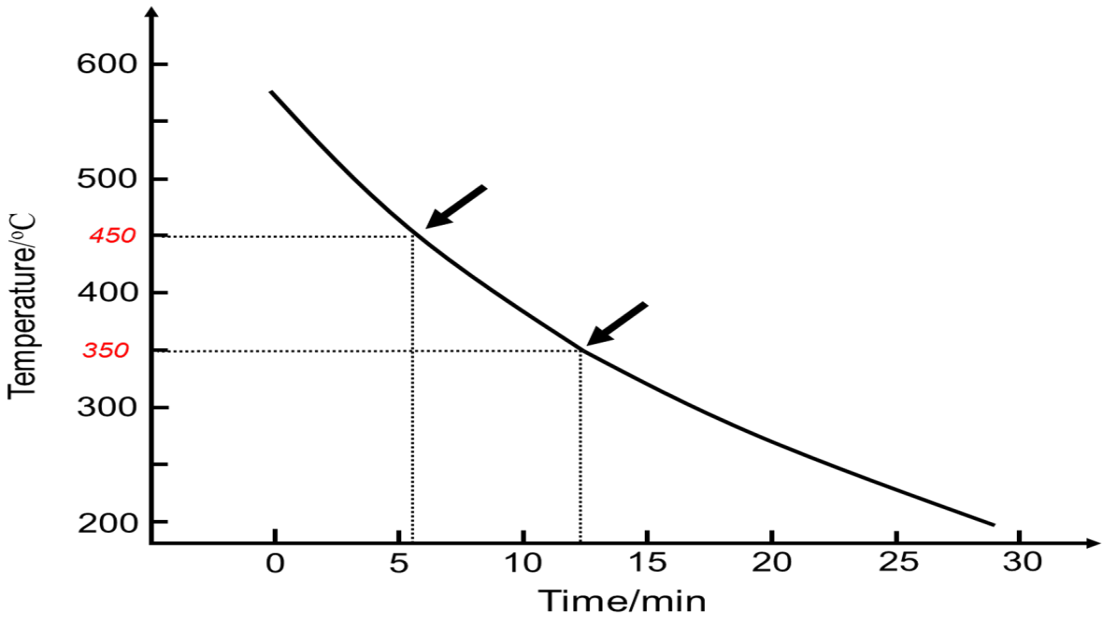

Fig. 3 Cooling curve of the homogenization air-cooling process

Samples	Solution treatment	Deformation	Aging temperature
Al-Mg-Si (Balance)	575 °C 3.6 ks water quenched	ASR: 30%,50%, 80%	150 °C/200 °C
Al-Li	560 °C 3.6 ks water quenched	CR: 10%,30%,60% ASR: 63%,80% HPT: 5 turns	CR/ASR: 200 °C HPT: 150 °C
Al-Li-Cu		CR: 10%,30%,60% ASR: 60%,72% HPT: 5 turns	
Al-Li-Mg		CR: 10%,30%,60% ASR:55% HPT: 5 turns	

Table 3 Deformation and aging treatment conditions

$$\varepsilon = \frac{\sqrt{2}}{3}\left[6\left[\ln\left(1-\frac{hi-hf}{hi}\right)\right]^2 + \frac{6}{(hi+hf)^2}\times\right.$$

$$\left.\left[R_1\cos^{-1}\left(\frac{2R_1-(hi-hf)}{2R1}\right) - R_2\cos^{-1}\left(\frac{2R_2-(hi-hf)}{2R_2}\right)\right]^2\right]^{1/2} \quad (1)$$

where h_i and h_f are the initial and final sheet thickness, R_1 and R_2 correspond to the radius of the upper and bottom roll.

For the CR experiment, the samples were cut from the hot and cold rolled sheet with a dimension of 10×8×3mm. Then, the samples were rolled to the final thickness of 1.2 mm with total thickness reduction of 60%.

For the HPT experiment, the as-homogenized ingot was rolled to sheet through hot and cold rolling processes, then the samples for HPT were cut from the sheet in the form of disks 10 mm in diameter and 1 mm thick. The disc samples were processed for N=5 turns with a rotation speed of 1.0 rpm at room temperature under a selected pressure of 6 GPa. The ε is calculated using the follow eq (2):

$$\varepsilon = \frac{2\pi rN}{\sqrt{3}h} \qquad \text{eq. (2)}$$

where r is the distance from the disk center, N is the number of rotations and h is the thickness of disk after HPT processing. The aging treatment and TEM observation samples of HPT processed alloys were made along radial directions from the disc center toward the edge in the range of 2-4 mm.

2.3 Sample characterization

Microhardness of HPT and CR processed samples was measured using a hardness tester (Mitutoyo HM-101, load:100 g, duration time:15 s). The hardness measurements of HPT samples were made along radial directions from the disc center toward the edge in the range of 2-4 mm. Hardness of the ASR processed samples were taken with microhardness tester (Struers, Duramin 5, load:200 g, duration time:15 s) on the RD-ND plane.

The microstructures of the Al-Mg-Si alloys after casting and homogenization were studied by optical microscopy (OM, Olympus BX51M) and scanning electron microscopy (SEM, Hitachi S3500). OM and SEM samples were prepared by electropolishing with an electrolyte consisting of 1/9 perchloric acid ($HClO_4$) and 8/9 ethanol (C_2H_5OH) at 15 V. TEM investigations of all the investigated alloys in the present work were carried out on a TOPCON EM-002B operated at 120 kV. TEM disks with a diameter of 3 mm were punched out from the as-homogenized foils previously thinned to around 70 μm using mechanical polishing. The disks were electropolished in a twin-jet polishing machine using a solution of 1/3 nitric acid (HNO_3) and 2/3 methanol cooled to approximately − 25 °C.

3. Experimental results

3.1 Effect of cooling rate on microstructure after homogenization treatment

3.1.1 As-cast microstructure

Fig. 4 and Fig. 5 show the dimensions and microstructures of the as-cast Al-Mg-Si alloys used in this work. As seen in Fig. 4(a), optical microscopy (OM) pictures revealed that there were many particles formed after casting in the Al-0.31Mg-0.68Si wt% Alloy. The SEM images with the corresponding elemental mappings were shown in Fig. 4(c)-(e), it is clearly seen that Mg-Si and Si-rich particles formed in the matrix after casting. Meanwhile, as shown in Fig. 5(b), many particles can be observed in the as-cast billets of Al-0.64Mg-0.32Si wt% alloy. The SEM images with the corresponding elemental mappings reveal that only Mg_2Si particles exist in the matrix after casting.

3.1.2 Cooled in the furnace

Fig. 6 shows the OM images of the excess Si and balance alloys after homogenization furnace-cooling. As seen in Fig. 6(a) and (b), furnace-cooling results in the recrystallization of grains and a more homogeneous distribution of precipitates within the grains. Most of precipitates exhibit rod/lath-shaped morphologies, the length is in the range from a few micrometers to as long as 30 μm. In addition, liquid-like grain boundary (GB) phase can only be found in furnace-cooled samples. The wetting phase transition of grain boundaries has been studied by Straumal [53-55]. His results show that there is a minimum temperature (T_{wmin}) for wetting phase transition, T_{wmin} is the wetting temperature for a GB with maximal energy. Obviously, during homogenization furnace cooling (20 ºC/H), the wetting transition occurred and incompletely wetted GBs are visible. It implies that the T_{wmin} for the investigated alloy is lower than 848K.

Fig. 6(c) and (d) show the microstructures of the balanced alloy after homogenization. When the samples were cooled in the furnace, as shown in Fig. 6(c), coarse Mg_2Si particles can be observed in the matrix. Fig. 6(d) is the magnified region in Fig. 6(c). It can be seen that many small rod or lath-like precipitates appeared in the matrix parallel to each other. The length of these fine and high number density precipitates is shorter than 10 μm.

Fig. 7 shows the TEM bright field images and SAED patterns of the precipitates in the furnace-cooled excess Si samples. Fig. 7(e)-(h) are SAED patterns taken from the marked areas in (a)-(d). As shown in Fig. 7(e) and (f), the precipitates are with two different orientations with respect to the Al matrix and fit well to the TYPE-A [13,56,57]. As seen in Fig. 7(b), Type-A can grow to at least 5 μm. Si phase was also confirmed in the matrix with two orientations relationships with respect to the Al matrix [15,58]. As seen in the Fig. 7(b) and Fig. 9, most of the Si phase exhibited lath shape after furnace-cooling.

Fig. 8 shows the bright field images of the precipitates in the furnace-cooled balance alloy, which correspond to Fig. 6(c). As shown in Fig. 8(a), many precipitates exhibit a lath-shaped morphology and are aligned parallel to each other along the same direction. Fig. 8(b) shows the cross sections of coarser precipitates, the size of the cross sections can be as long as 80 nm. The enlarged cross sections of the precipitates along the line are shown in Fig. 8(c) and (d). It can be seen that except for the β′ phase, a combination of β′ phase and Type-B is also observed in the furnace-cooled samples [59].

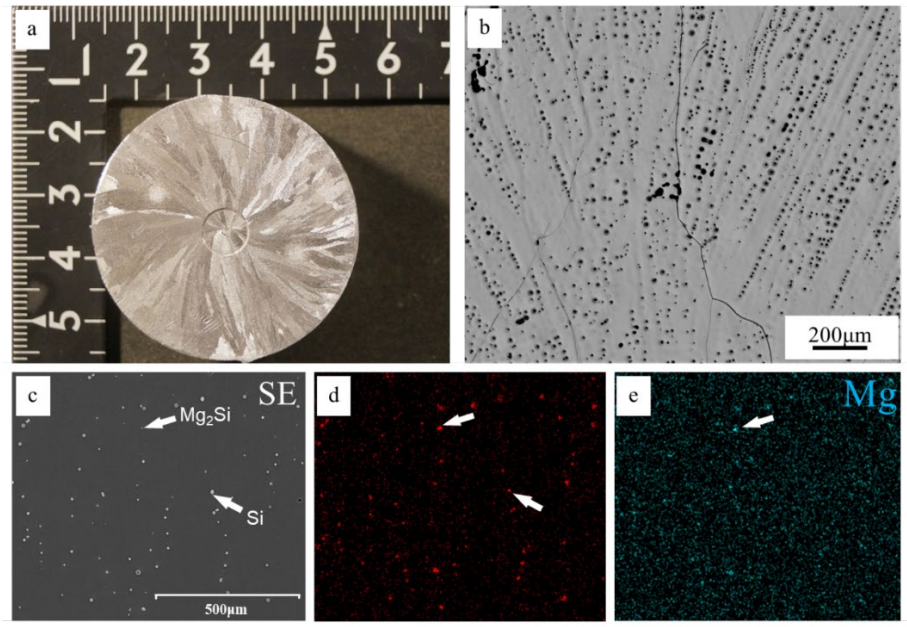

Fig. 4 The dimensions and microstructure of the as-cast excess Si alloy: (a) the dimension and grains size of the as-cast billet, (b) OM images of the as-cast billet, (c) SEM image and (d)-(e) the corresponding elemental mappings of the as-cast alloy.

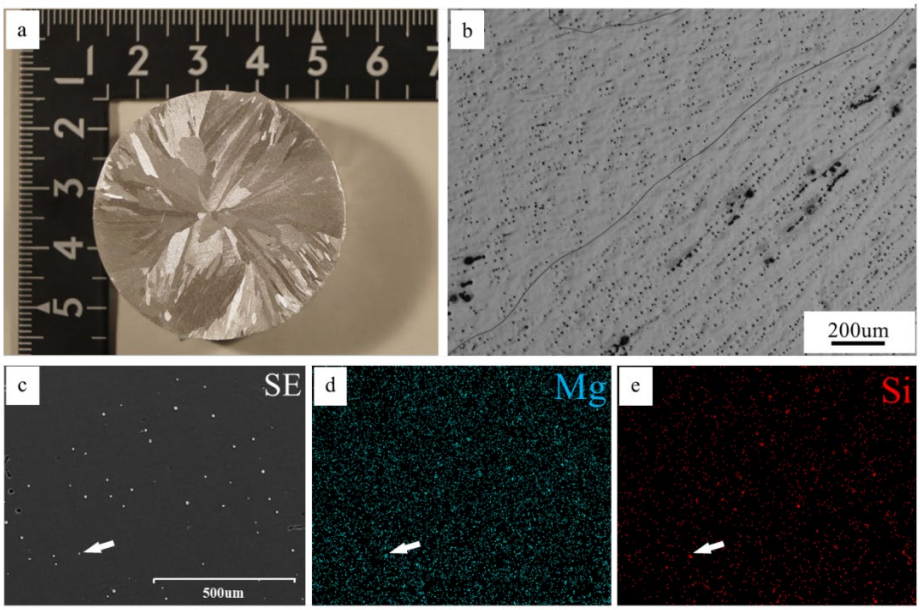

Fig. 5 The dimensions and microstructure of the balanced alloy: (a) the dimension and grains size of the as-cast billet, (b) OM images of the as-cast billet, (c) SEM image and (d)-(e) the corresponding elemental mappings of the as-cast alloy.

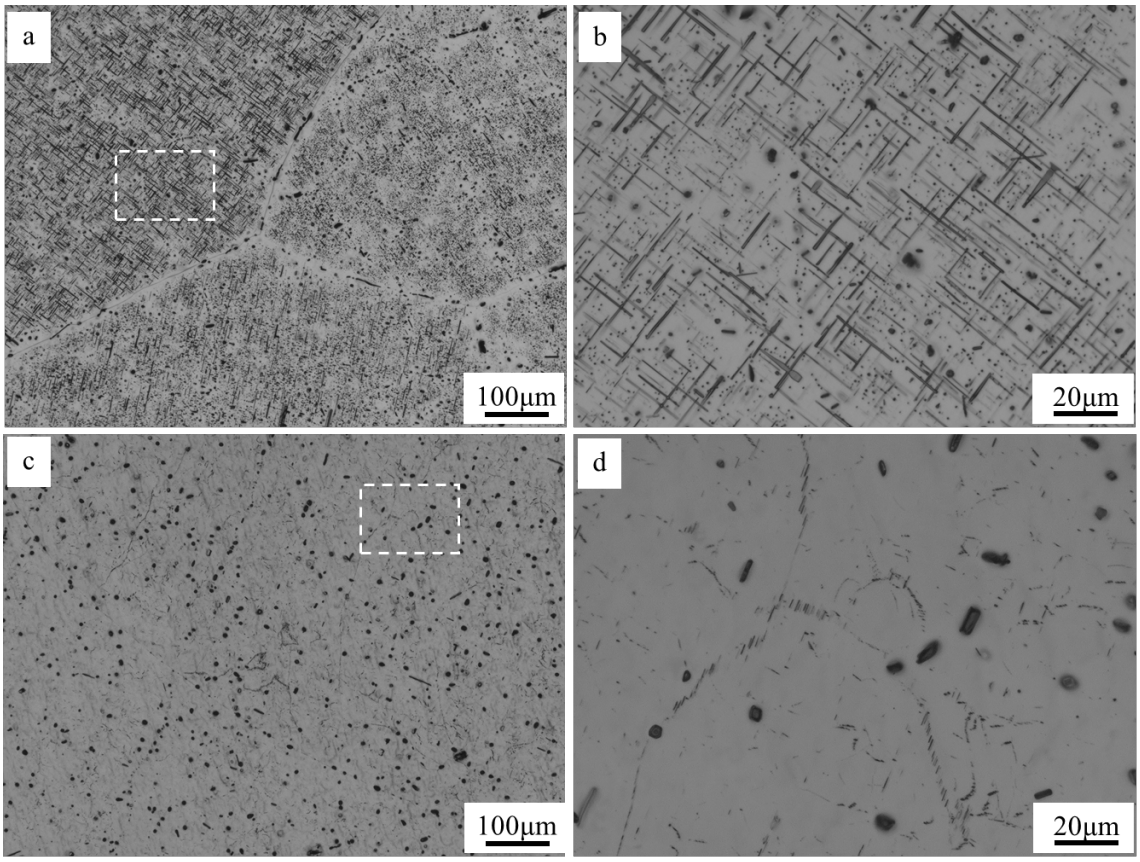

Fig. 6 Optical micrographs of the (a-b) excess Si and (c-d) balanced alloys after homogenization furnace-cooling: (b), (d) are magnified regions of (a), (c).

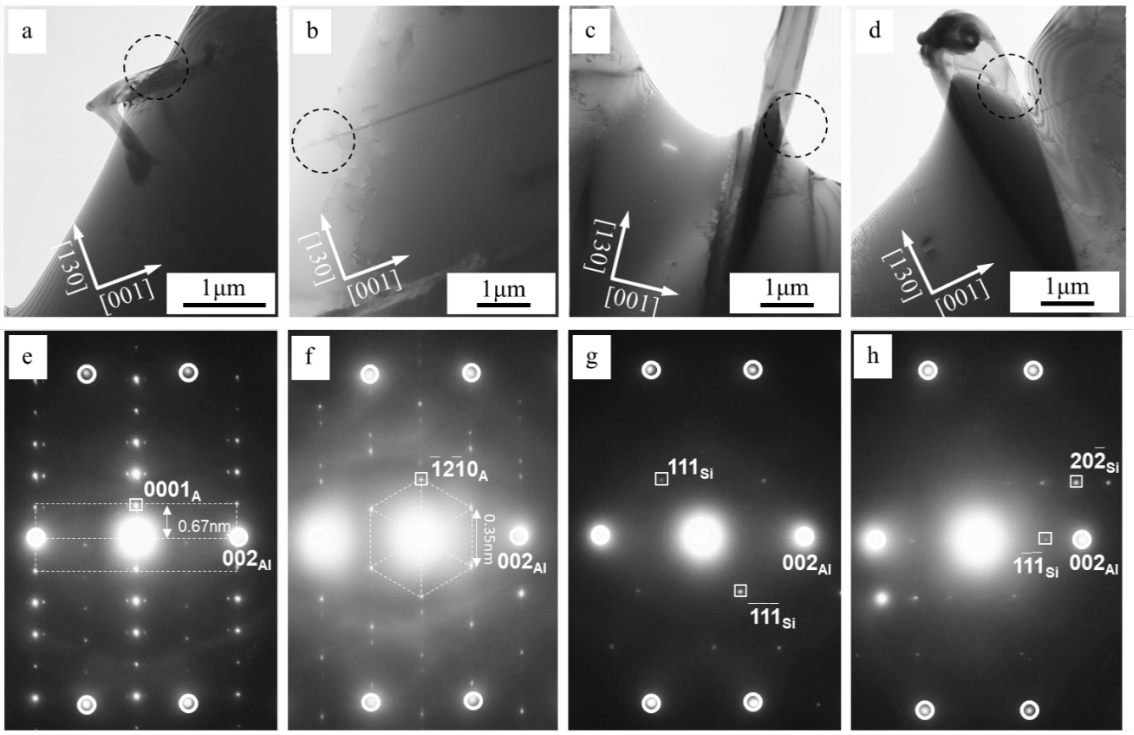

Fig. 7 TEM bright filed images and SAED patterns of the precipitates formed during homogenization furnace cooling. (e)-(h) are taken from the marked regions in (a)-(d). The incident beam direction is parallel to $[3\bar{1}0]_{Al}$.

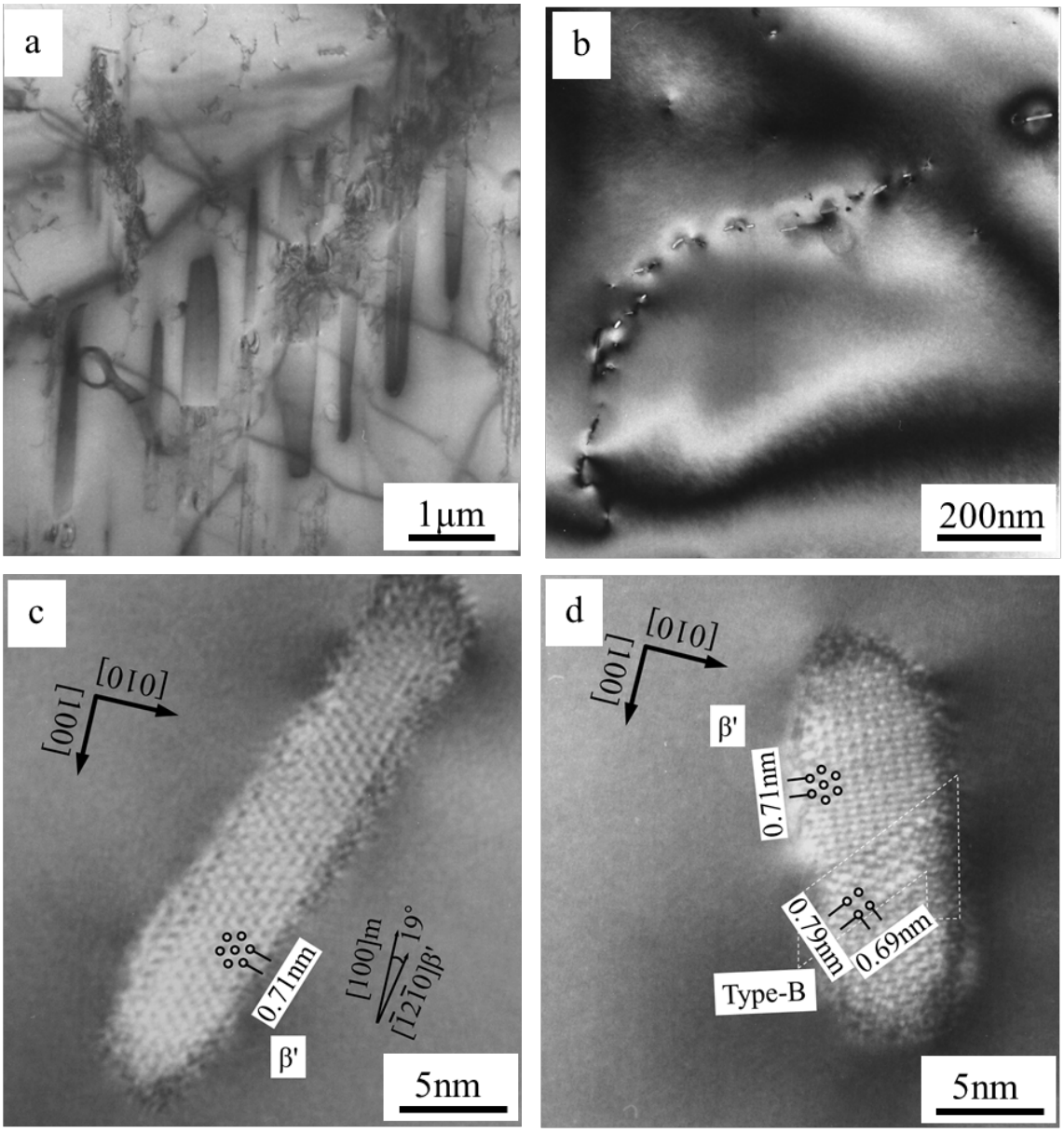

Fig. 8 Heterogenous precipitates formed in balanced alloy after homogenization furnace-cooling, (a) bright field image and enlarged photograph of the rod-section.

3.1.3 Cooled in the air

Fig. 9 shows the OM images of the samples after homogenization air-cooling. As can be seen, when the samples were cooled in air, the grains are still dendritic and few precipitates can be found, regardless of the alloy composition. This means that the dissolution of Mg_2Si and Si was complete when homogenization was carried out at 575 ^oC for 2 H. Meanwhile, the air-cooling rate was high enough to trap the Mg and Si atoms in the solution.

However, after air-cooling, many "boundaries" are visible within the grains, as shown in Fig. 9(b), small precipitates can also be observed along these "boundaries". For the balance alloy, unlike the furnace-cooled samples, no obvious rod/lath-like precipitates could be observed along these "boundaries", as shown in Fig. 9(d).

Fig. 10 show the TEM bright filed images of the air-cooled samples. The "boundaries", which were found in the Fig. 9, were confirmed in both of the excess Si and balance alloys. As shown in Fig. 10(a), two "boundaries" are visible and the precipitates only tend to distribute along the right one in two visible $[100]_{Al}$ and $[010]_{Al}$ directions. The misorientation angle of the left one is about 6^o and the right one is lower than 1^o. It can be suggested that the right one is not real boundary but caused by the precipitates formed along dislocations. Fig. 10(b) is the magnified part of the Fig. 10(a) in which the precipitates were apparently observed to heterogeneously nucleated on the right boundary along two perpendicular Al directions. According to the diffraction patterns in the upper right, Type-C and β′ can be detected along the dislocation. For the balance alloy. As seen in Fig. 10(b), in contrast to the precipitates formed in the furnace-cooled samples, the small precipitates grow along the $[100]_{Al}$ and $[010]_{Al}$ directions with

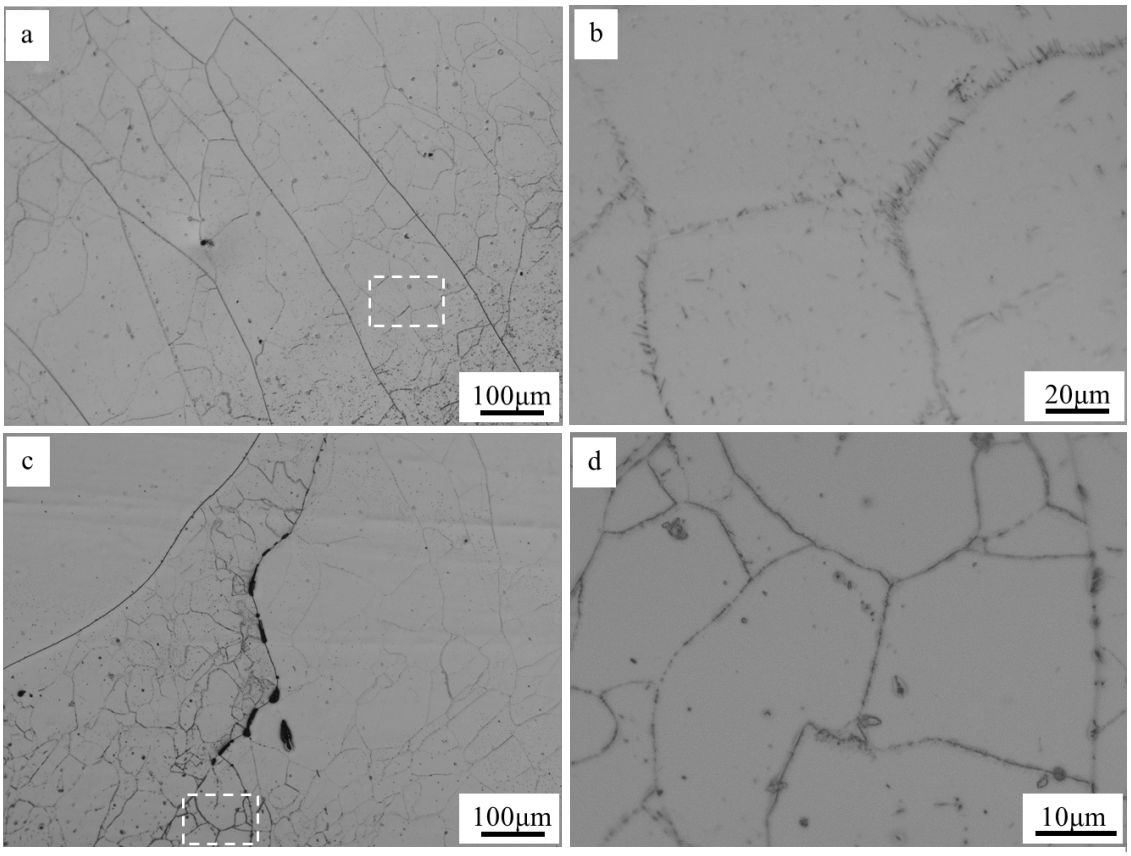

Fig. 9 Optical micrographs of the (a-b) excess Si and (c-d) balanced alloys after homogenization air-cooling. (b), (d) are magnified regions of (a), (c).

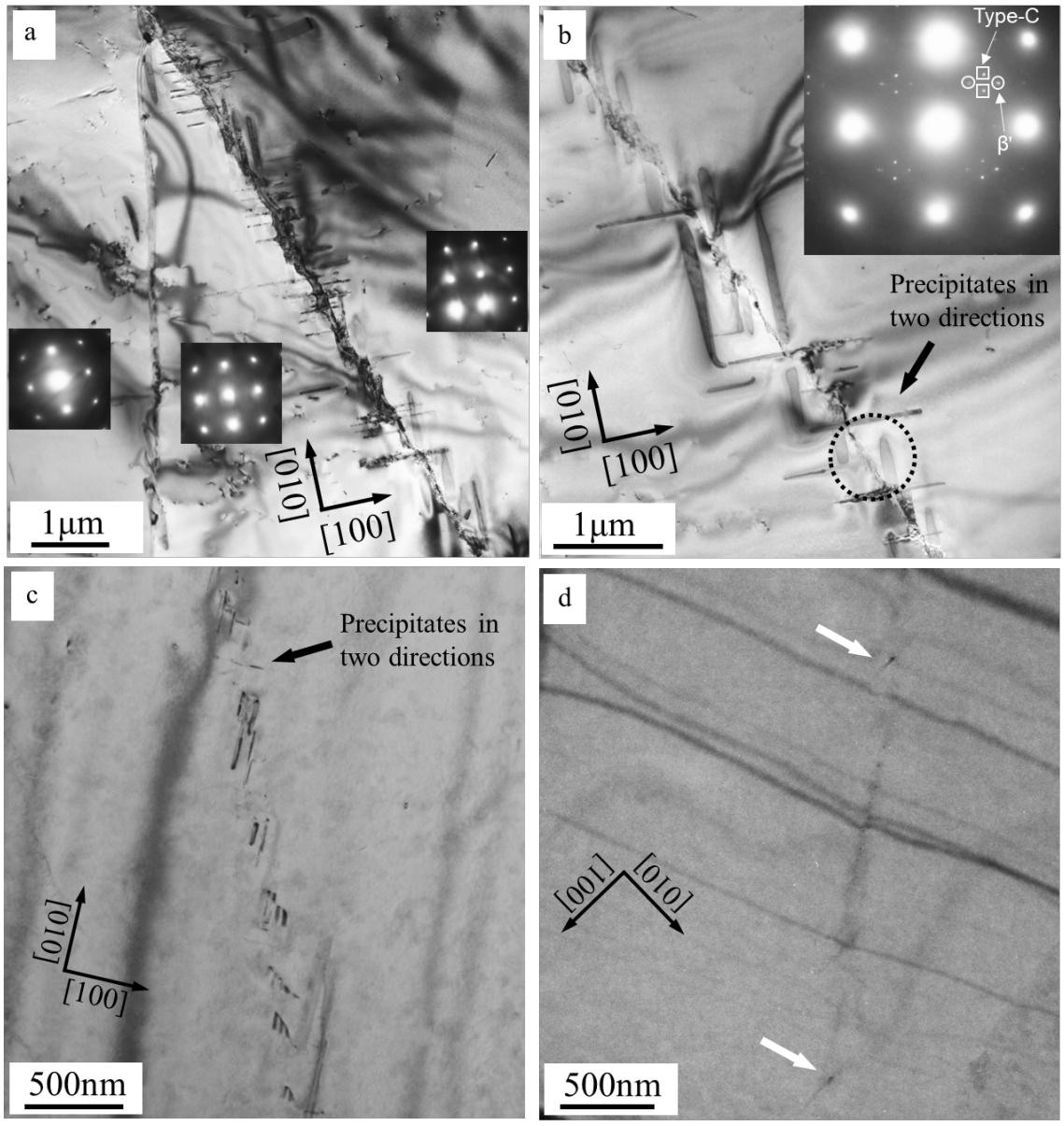

Fig. 10 TEM bright field images of the heterogenous precipitation in (a-b) excess Si and (c-d) balanced alloys after homogenization air-cooling. (b), (d) are magnified regions of (a), (c).

lengths shorter than 300 nm. it is obvious that the precipitates in the air-cooled samples are smaller than those in the furnace-cooled samples.

However, different to the precipitates from along the dislocation in which the dislocations are lined up and parallel to each other. These precipitates are found to tend to distribute in two directions. This behavior of the precipitates is frequently observed in the studied two alloys after air-cooling.

Fig. 11 shows the cross-sections of the heterogeneously nucleated precipitates in the matrix of excess Si alloy. The magnified cross-sections are shown in Fig. 11(b)-(d). It can be found that the over-aged composite precipitates of Type-C/Type-B and Type-A/Type-B together with the under-aged string-like precipitates on the dislocations [12,31].

Fig. 12 shows the TEM bright field images of the air-cooled samples with the incident beam directions along $<001>_{Al}$ for all the images, the precipitates formed along the dislocations are shown in Fig. 12(a) and (b), which should be responsible for the "boundaries". Fig. 12(a) is the magnified region along the dislocation line in Fig. 9(d). As can be seen, precipitates have nucleated along a line in the matrix. The string-like precipitates can always be found between the other precipitates along the dislocations [30,31]. As indicated with arrows in Fig. 12(b) and (c), the angles between the direction of string-like precipitates and the [100] matrix direction are 30-40°.

Fig. 12(d) and (e) are magnified region along the dislocation line in (a). As marked in a dashed circle in Fig. 12(a), the string-like precipitates consist of many small precipitates. Meanwhile, as shown in Fig. 12(e), even when the cooling rate was high (~830 °C/H), the β′/Type-B composite precipitates could be observed along the dislocations in the air-cooled samples.

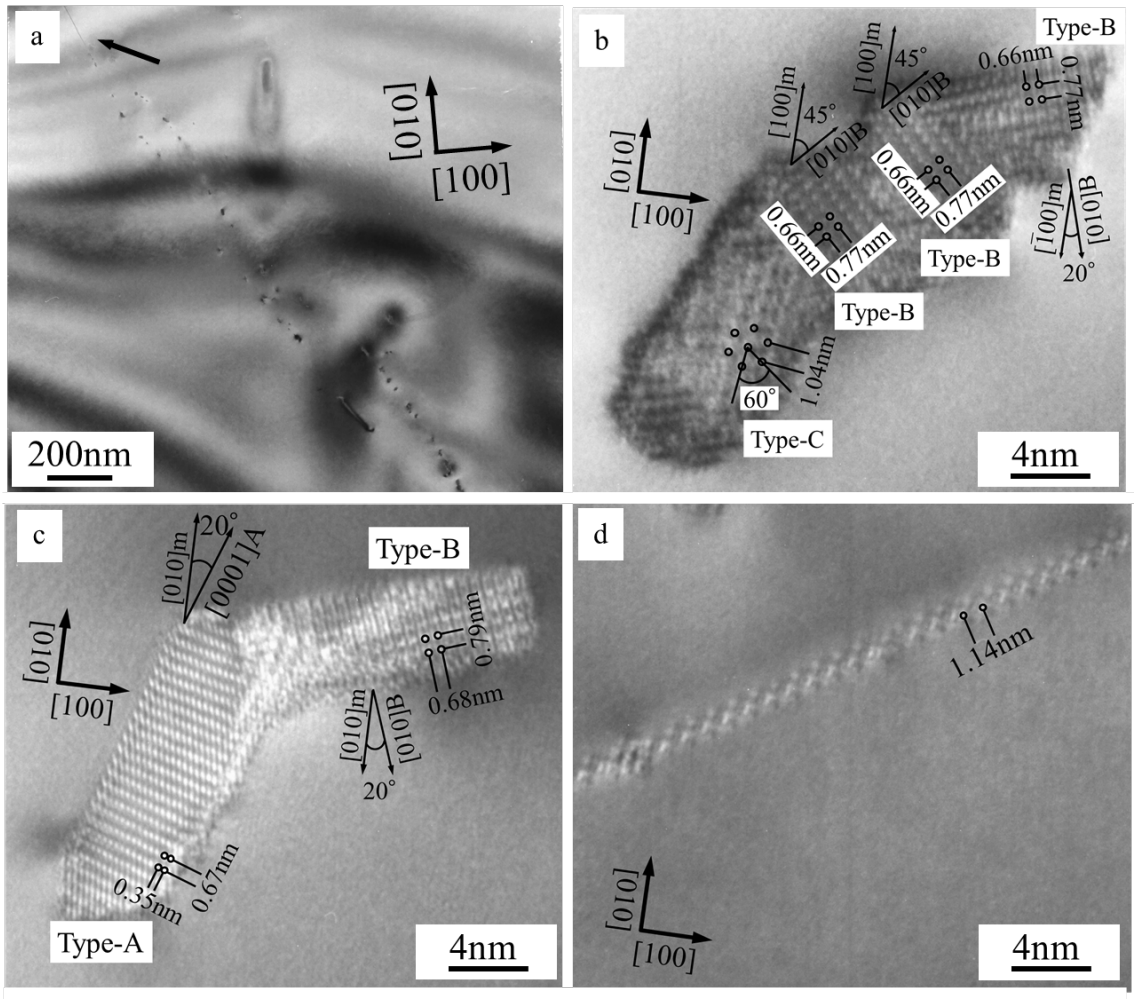

Fig. 11 TEM bright field images and the SAED patterns of the air-cooled excess Si alloy. (b) is the magnified region of (a), the SAED pattern was taken from the marked area with dashed circle. (c-f) are the cross-sections of the precipitates found in the matrix. The incident beam direction for all the pictures is $<100>_{Al}$.

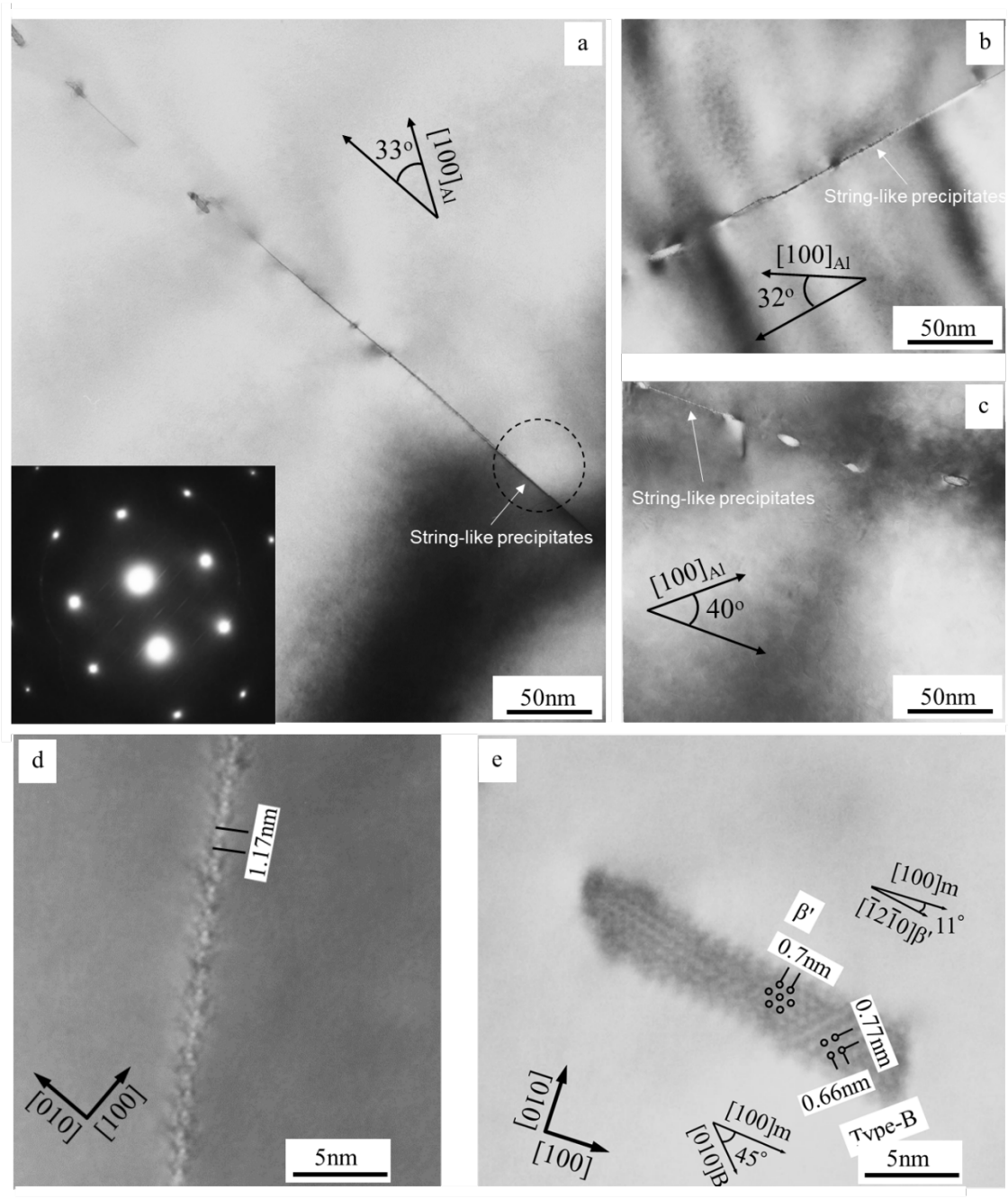

Fig. 12 TEM bright field images and the SAED pattern of the balanced alloy after homogenization air-cooling. (a) is the magnified region of Fig. 9(d), the diffraction pattern in the lower left was taken from the marked area with dashed circle. (b) and (c) are the similar microstructures found in the matrix. (d) and (e) were magnified from the (a).

3.1.3.1 Mechanism of heterogeneous precipitation during homogenization air-cooling

It is well known that with the presence of dislocations, the precipitates in the Al-Mg-Si alloys are lined-up and parallel to each other during aging treatment [30,31,60-62]. However, in the present work, the dislocation-induced precipitates grow along $[100]_{Al}$ and $[010]_{Al}$ directions, as shown in Fig. 10.

In order to classify how the precipitates form along the dislocations during homogenization cooling stage and why they are different to the precipitates under the isothermal aged conditions, the air-cooled samples during homogenization cooling were stopped at different temperatures. The samples were divided into three groups. The first group was quenched in chill water directly after homogenized at 575 °C for 2 H. The other two groups were taken out from the furnace at the temperature of 450 °C and 350 °C, respectively.

Fig. 13 shows the OM images of the samples during air-cooling stopped at different temperature. As seen in Fig. 13 (a) and (b), when the samples stopped at 450 °C, there is no boundaries can be observed within the grains, however, as the temperature continues to decrease to 350 °C, the boundaries, which are similar to the Fig. 9, are visible within the grains. As shown in Fig. 13 (e) and (f), the precipitates can also be found along the dislocations, this means that the precipitates have nucleated on the dislocations at this temperature.

Fig. 14 shows the SEM and EBSD micrographs of the balance alloy cooled to 350 °C, the region of Fig. 14 corresponds to the Fig. 13(d). Obviously, there is no sub-boundaries inside the grains, all the “boundaries” are caused by precipitates along the

dislocations.

Fig. 15 shows the microstructure of the two Al-Mg-Si alloys after homogenized at 575 ºC for 2 H and quenched in water. It can be seen that many dislocations formed in the matrix. Since the cooling rate is high when quenching the billets in water, these dislocations may due to the cooling strain or have formed in the matrix before quenching.

The microstructures of the excess Si alloys cooled to 450 ºC are shown in Fig. 16, similar to the as-quenched state, the dislocations also can be found in this group. At the same time, the precipitates are not observed along the dislocations, which corresponds to the Fig. 13, no “boundaries” can be found within the grains. This suggests that it is difficult for the precipitates nucleate on the dislocation when the samples were taken out of the furnace at this temperature. It should be note that when the temperature decreased to 450 ºC, the dislocation exhibits a wavy contrast, as shown in Fig. 16(d), it is due to the climb/glide of the dislocations under high temperatures.

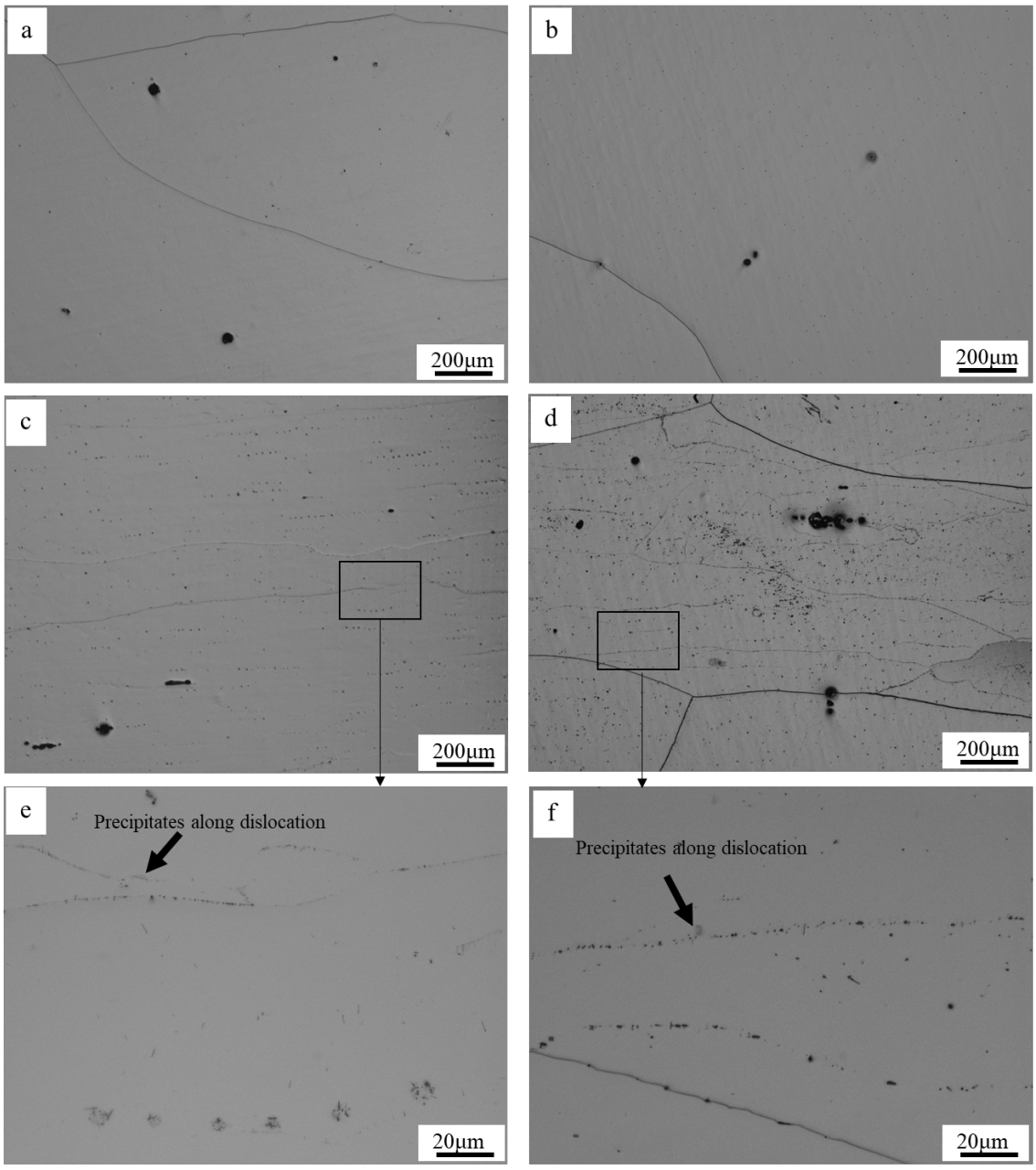

Fig. 13 Optical micrographs of the (a,c,e) excess Si and (b,d,f) balanced alloys during homogenization air-cooling stopped at (a)-(b) 450 ºC and (c)-(f) 350 ºC. (e) and (f) are magnified region of (c) and (d).

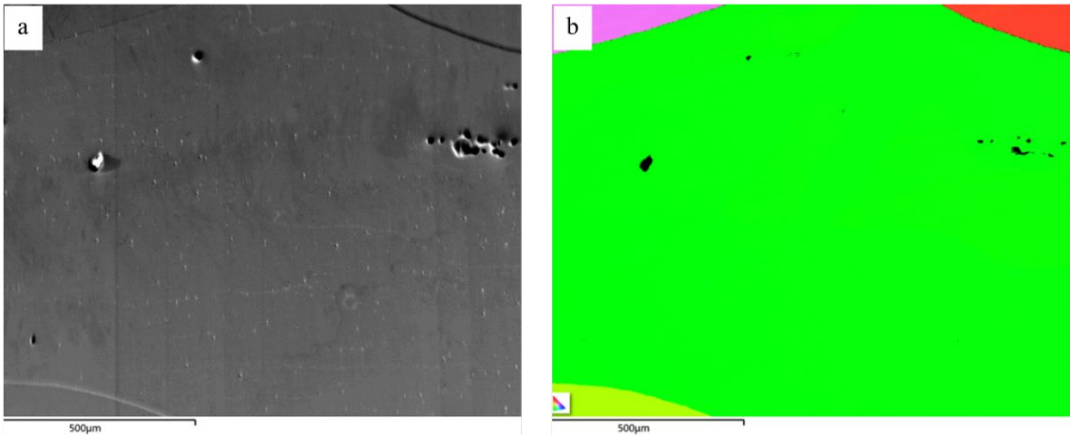

Fig. 14 SEM and EBSD micrographs of the balanced alloy cooled to 350 ºC. The region corresponds to Fig. 13(d).

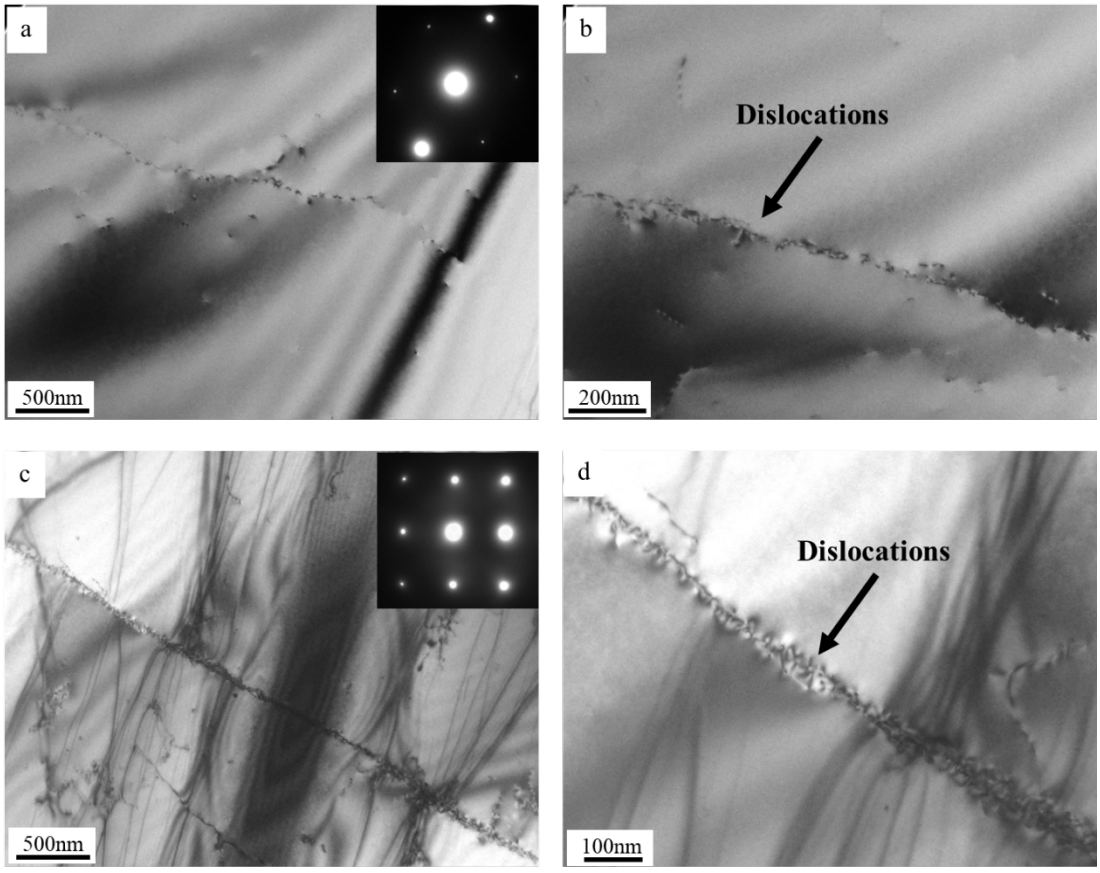

Fig. 15 TEM bright field images of the (a-b) excess Si and (c-d) balanced alloys after homogenization at 575 ºC for 2 H and quenched in water. (b) and (d) are magnified region along the dislocations of (a) and (c).

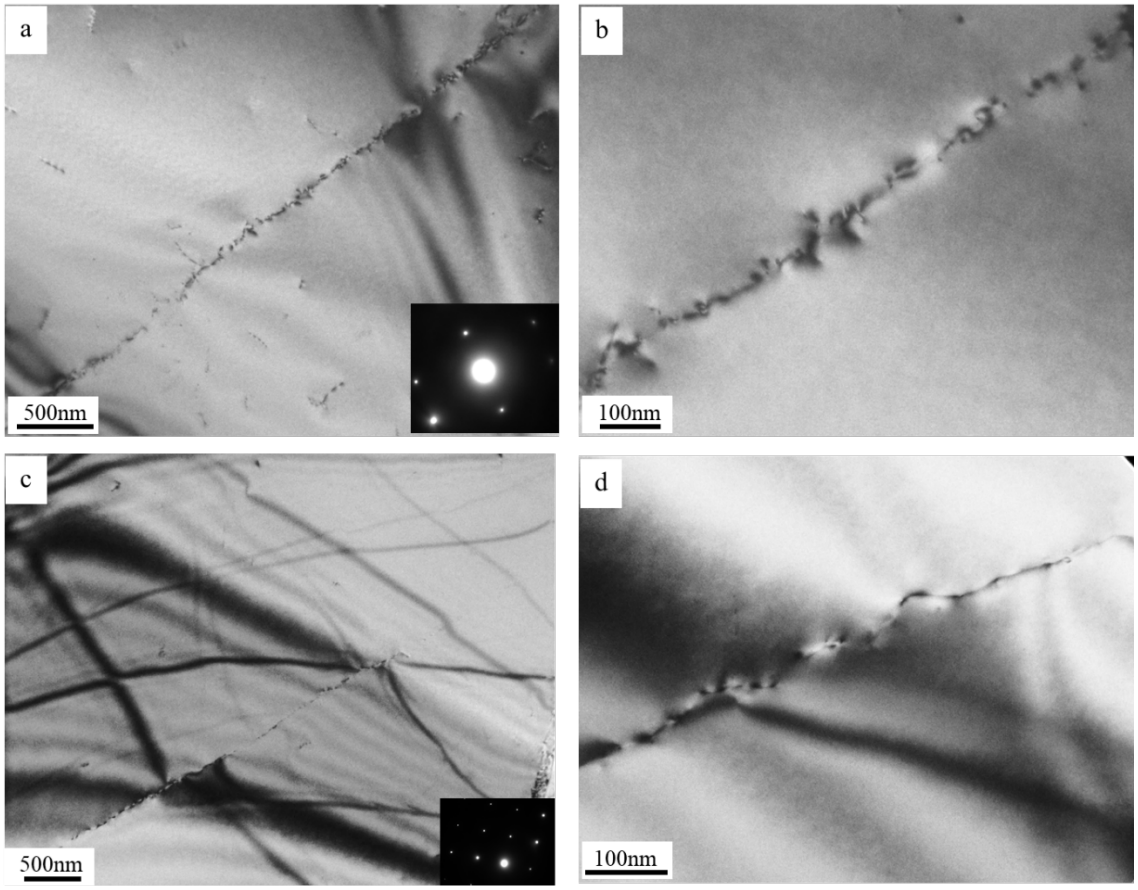

Fig. 16 TEM bright field images of the excess Si alloy during homogenization cooling stopped at 450°C. (b, d) is magnified region along the dislocations of (a, c).

Fig. 17 shows the microstructures of the excess Si alloy during homogenization cooling stopped at 350 ºC, as seen in Fig. 17(a), when the incident beam direction is along $<112>_{Al}$ zone axis, there is two equivalent $<100>_{Al}$ directions. However, the precipitates only along one [100] direction can be observed. This indicates that the precipitates nucleate on the dislocations during cooling was not along three $<100>_{Al}$ directions. As shown in Fig. 17(b), the dot-like precipitates near the dislocations can also be found, it is the precipitates along the $[001]_{Al}$ direction. Under this condition, the precipitates form along the dislocations along two $<100>_{Al}$ directions. Meanwhile, as shown in Fig. 17(c), under the same condition, dislocations without precipitates can be found in the matrix, which is similar to that when the temperature decreases to 450 ºC.

Fig. 18 shows the microstructure of the balance alloy when temperature decreases to 350 ºC. The incident beam directions are near the $<100>_{Al}$ zone axis for all the images. As shown in Fig. 18(a), it is clearly seen that the precipitates formed along the dislocations along two directions. However, in the Fig. 18(b), the precipitates formed along the dislocations were found to along three $<100>_{Al}$ directions, as indicated by the arrows.

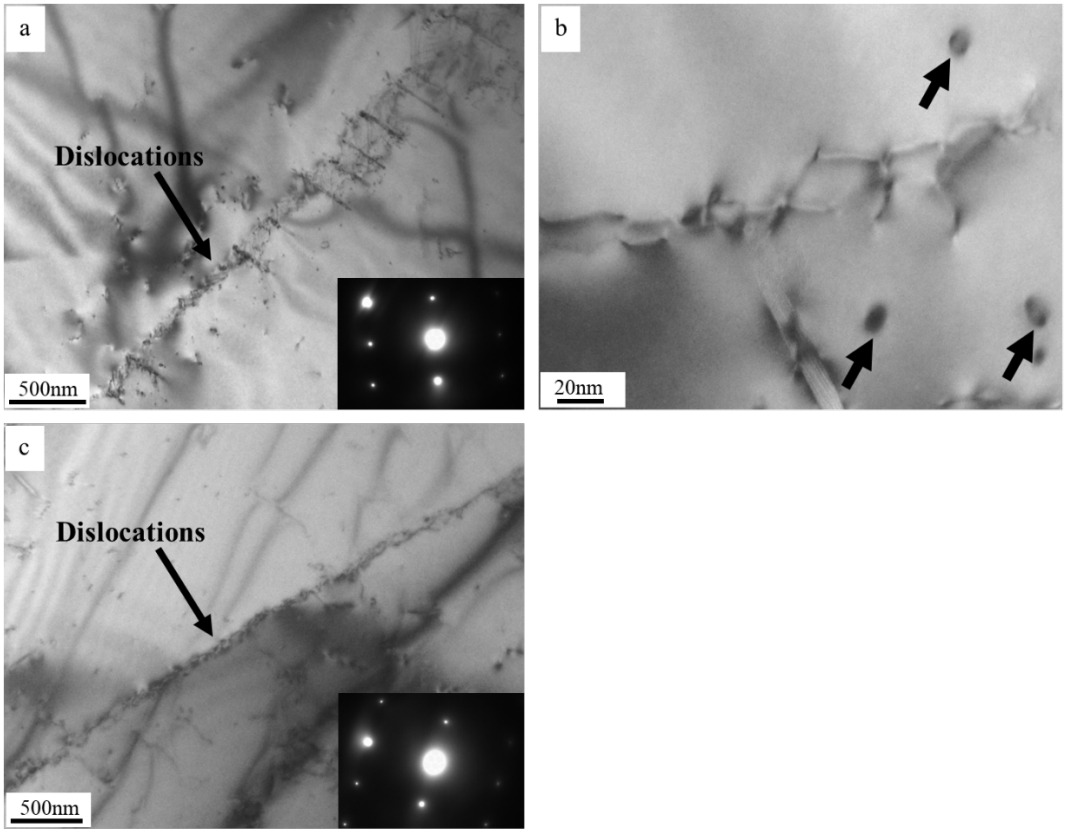

Fig. 17 TEM bright field images of the (a-b) excess Si alloy during homogenization cooling stopped at 350 ^{o}C. (b) is magnified region along the dislocations of (a).

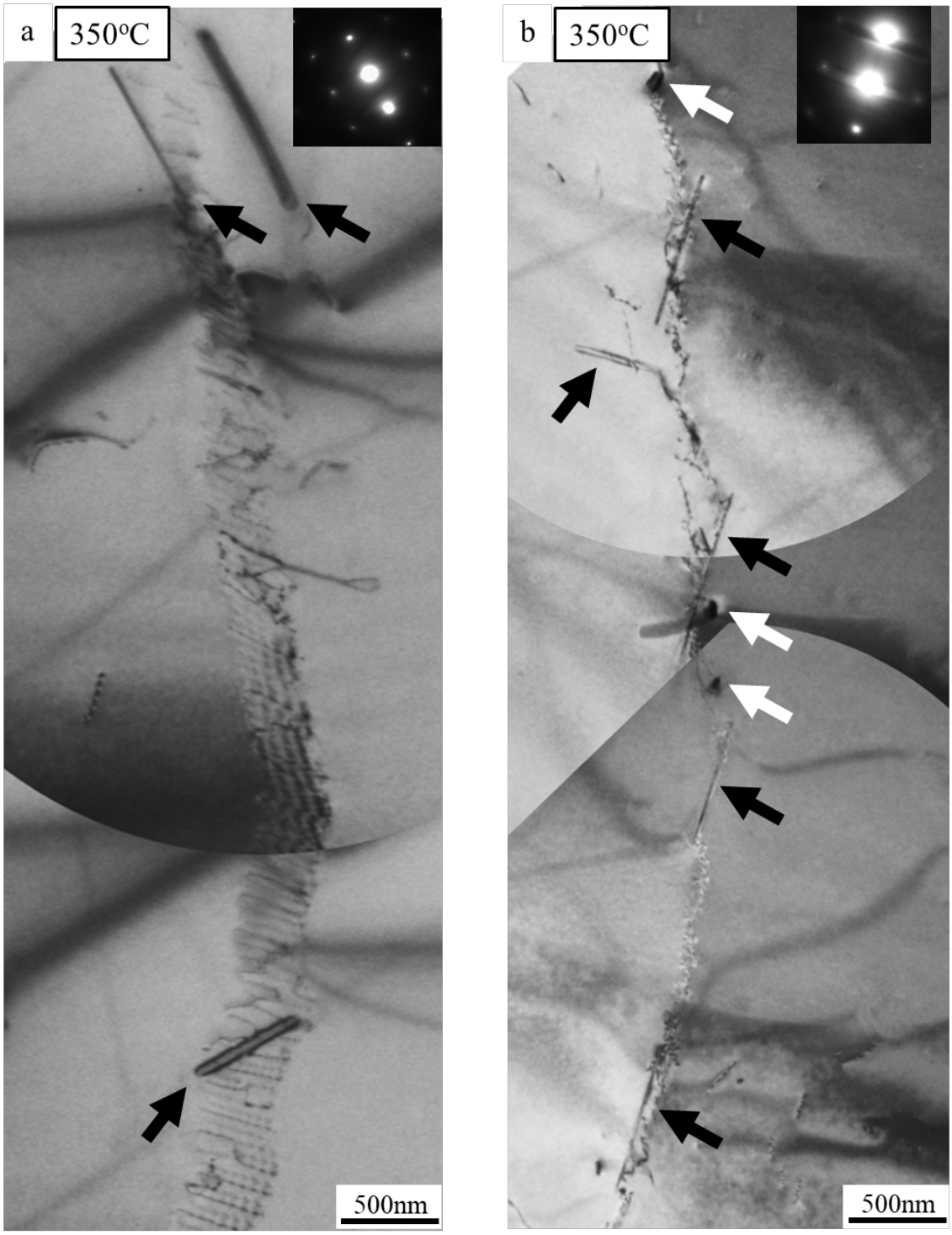

Fig. 18 TEM bright field images of the balanced alloy during homogenization cooling stopped at 350 °C. (a) and (b) are different dislocations found in the matrix.

3.2 Effect of homogenization on microstructure and precipitation after extrusion and solution treatment

3.2.1 After hot extrusion

Fig. 19 shows the OM and EBSD images of the as-extruded excess Si type alloy with different homogenization treatment. Form the OM images, as shown in Fig. 19(a), it can be seen that the grain size is uniform in the as-extruded samples without homogenization. However, for the samples with homogenization, the distribution of the grain size is not uniform, some big grains together with very small grains can be observed after extrusion, especially in the air-cooled samples, it is clearly that there are some big grains, and also in some areas along the extrusion direction, there are some small grains. EBSD confirmed the uneven distribution of the grain sizes. At the same time, as can be seen from Fig. 20, this phenomenon was also found in the balanced alloy, the distribution of the grain sizes in the samples without homogenization is more uniform than that in the samples with homogenization. This suggests that the distribution of the grain size is not sensitive to the alloy composition, but to homogenization treatment.

Fig. 21 shows the OM images at high magnification, for the excess Si alloy, many as-cast particles remained in the matrix of the samples without homogenization. When the samples cooled in the furnace, the rod-lath like precipitates broken and distribute along the rolling direction. However, for the samples cooled in the air, the precipitates are not clearly. Fig. 21(d)-(f) shows the OM images of the balanced alloy. As seen in (e), Coarse particles of Mg_2Si can be observed in the furnace-cooled samples. Meanwhile, it looks like many small particles in the air-cooled samples after hot extrusion.

Fig. 22 shows the TEM images of the as-extruded microstructure of the excess Si alloy,

as shown in Fig. 22(a), after homogenization, the distribution of particles in the samples without homogenization are not uniform, in particular, near the Si particle areas. In the region 1, there is almost no particles, however, in the region 2, many particles can be observed. Although the grain size distribution is uniform in the samples without homogenization, however, the distribution of the Si and/or Mg_2Si particles is not uniform in the matrix. As shown in Fig. 22(d), for the air-cooled samples, many small particles are visible, many of the particles at the sub-grain boundaries. The region in Fig. 22(d) corresponds to the area with a small grain size in Fig. 19. According to the shape the particles, most of them are Si. The microstructure of the furnace-cooled samples is shown in Fig. 22(e), the remained big particles of Si can be found, during extrusion, the Si particles or the Type-A, broken and remained. However, the Si particles are not too much, which can be found in the matrix of the No-homogenized and air-cooled samples. because the cooling rate after homogenization furnace cooling is low (20 ^{o}C/H), the precipitates have completely precipitated, the rod-like precipitates are due to the remained precipitate, which formed during homogenization furnace-cooling.

3.2.2 After solution heat treatment

Fig. 23 shows the microstructure after solution heat treatment, it can be seen that many particles remained in the matrix of the excess Si samples without homogenization, also some particles can be found in the furnace-cooled samples. however, when the samples cooled in the air, all the particles dissolved and almost no precipitates remained after solution treatment. In the case of balanced alloy, many coarse particles remained, for air-cooled samples, these particles disappeared. It should be note that air-cooled samples exhibit the largest grain size among the three group samples.

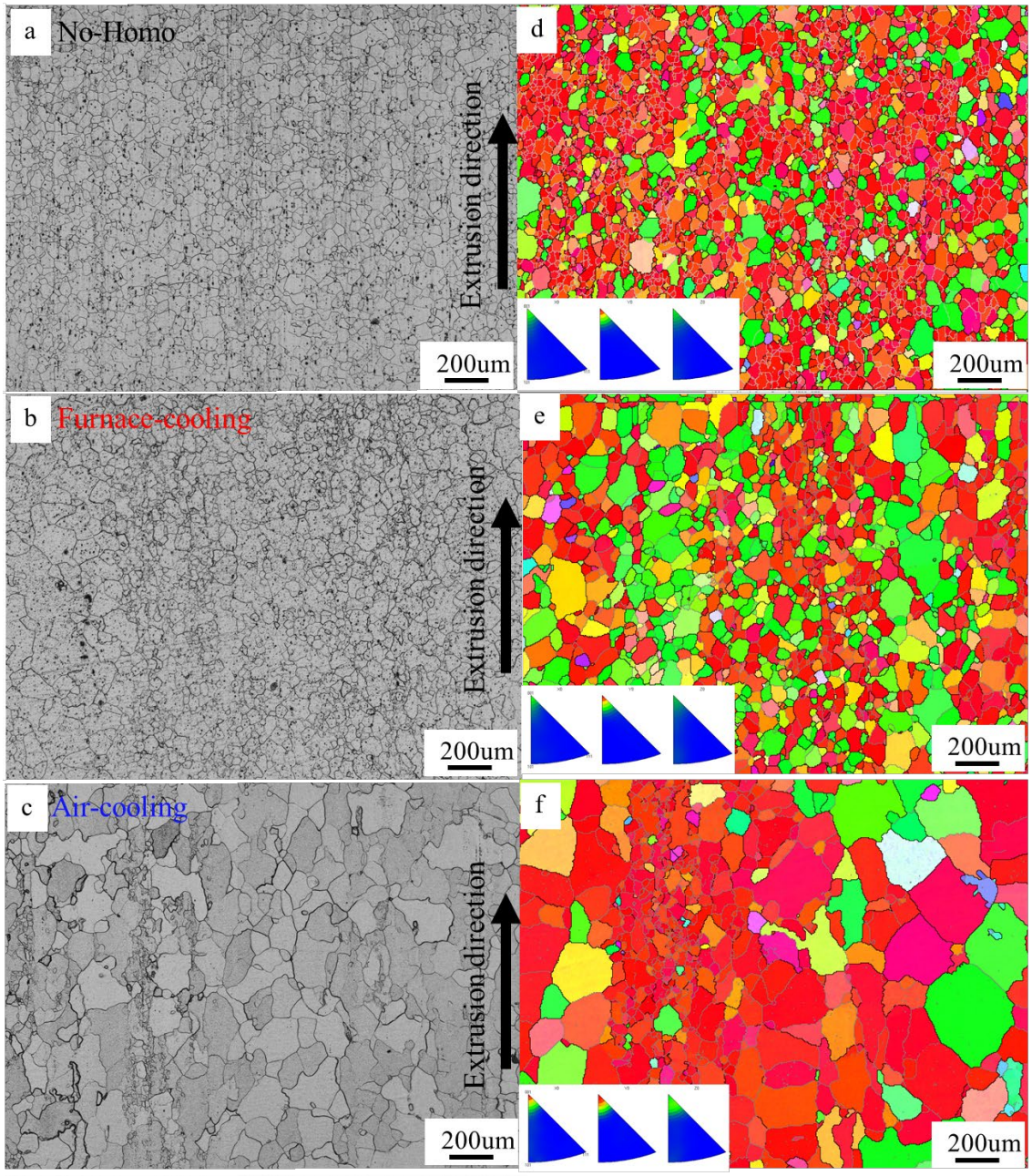

Fig. 19 OM and EBSD images of the as-extruded excess Si alloy with different homogenization treatments: (a, d) without homogenization, (b, e) cooled in the furnace, (d, f) cooled in the air. The corresponding inverse pole figures are shown in the lower left of the EBSD images.

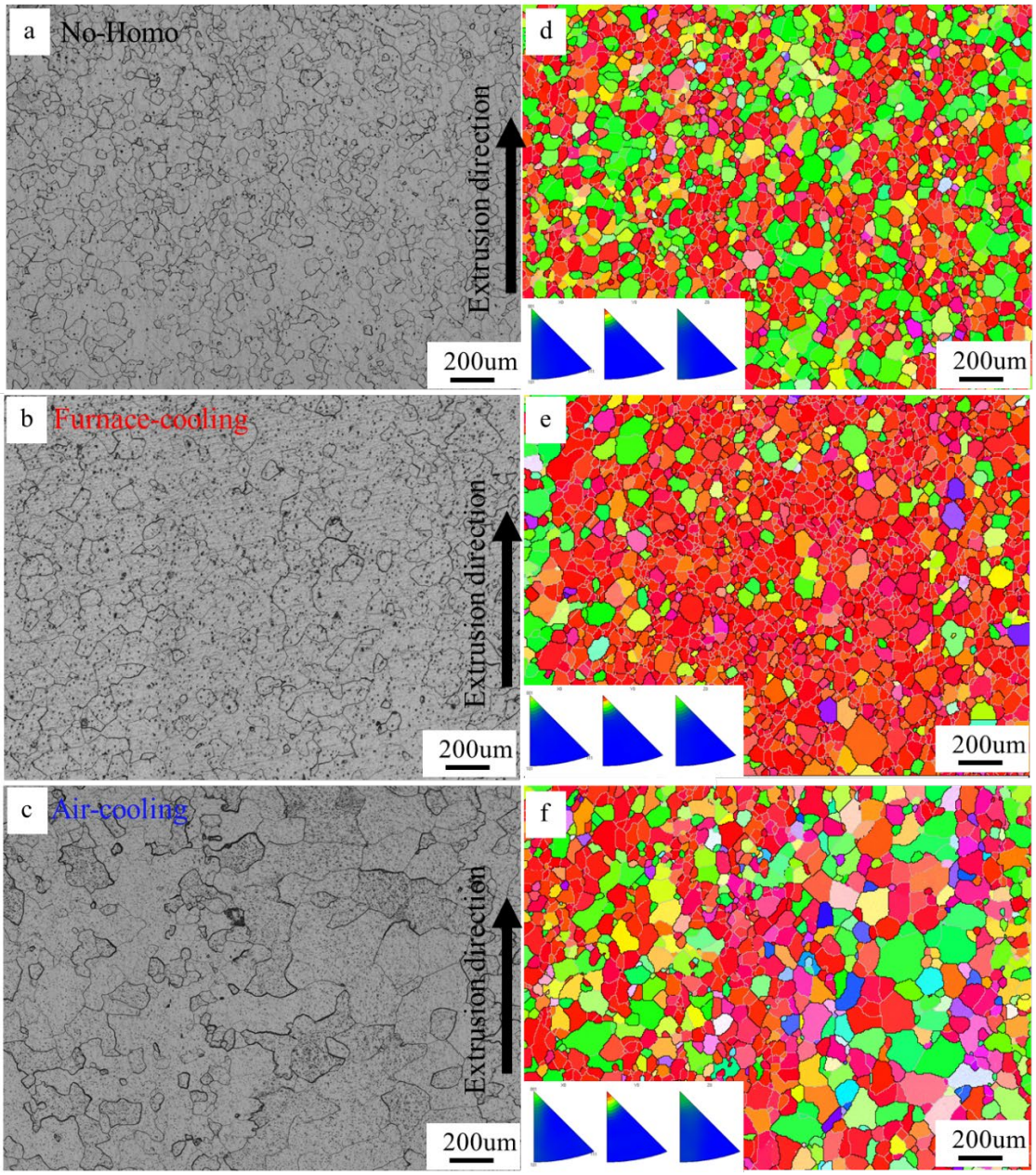

Fig. 20 OM and EBSD images of the as-extruded balanced alloy with different homogenization treatments: (a, d) without homogenization, (b, e) cooled in the furnace, (d, f) cooled in the air. The corresponding inverse pole figures are shown in the lower left of the EBSD images.

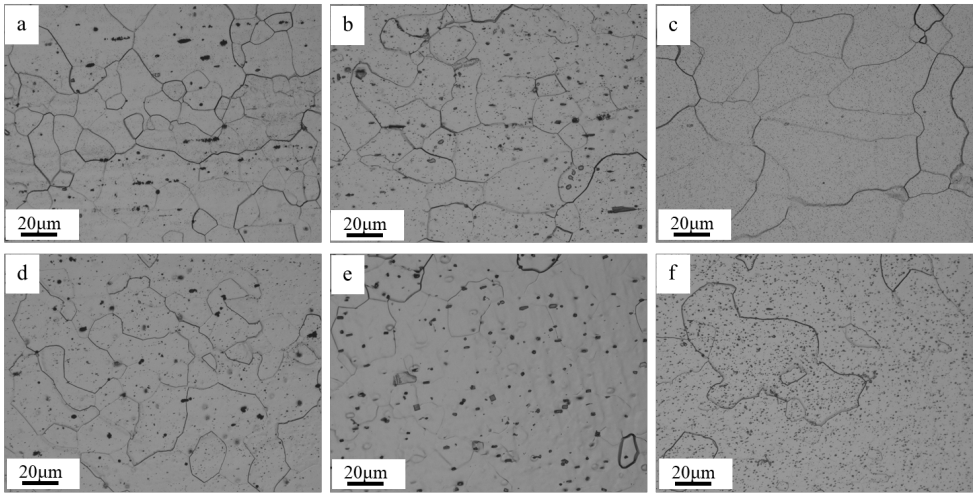

Fig. 21 OM images of the as-extruded (a-c) excess Si and (d-f) balanced alloys with different homogenization treatments: (a, d) without homogenization. (b, e) cooled in the furnace. (d, f) cooled in the air.

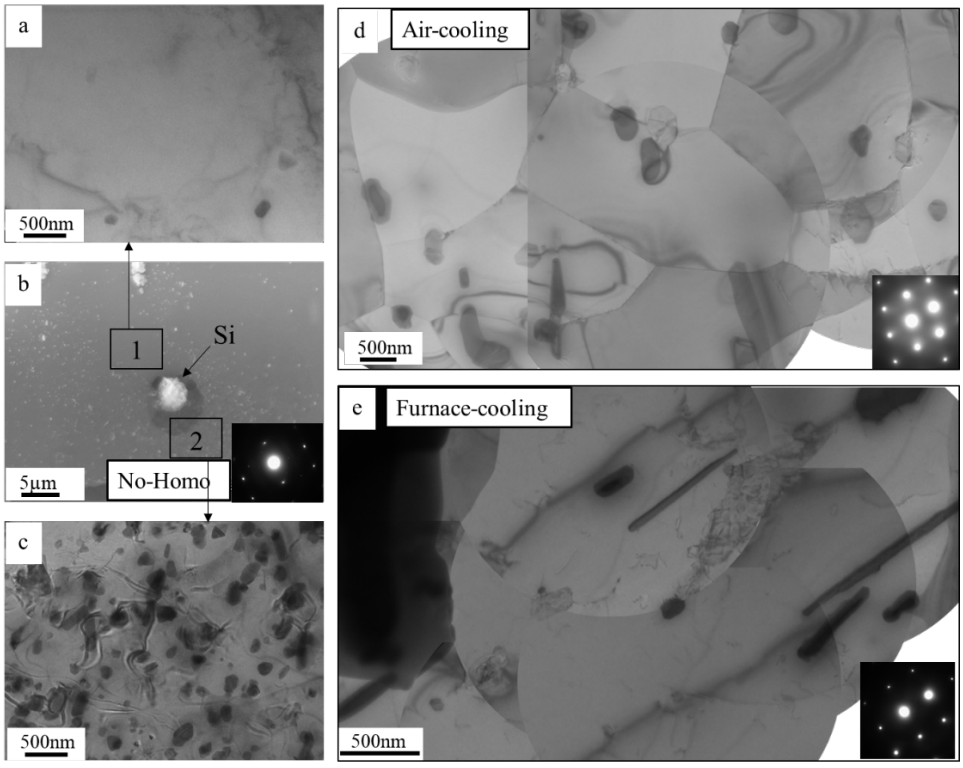

Fig. 22 SEM and TEM images of the as-extruded excess Si alloy with different homogenization treatments: (a-c) without homogenization. (d) cooled in the furnace. (e) cooled in the air. (b) is SEM image under low magnification.

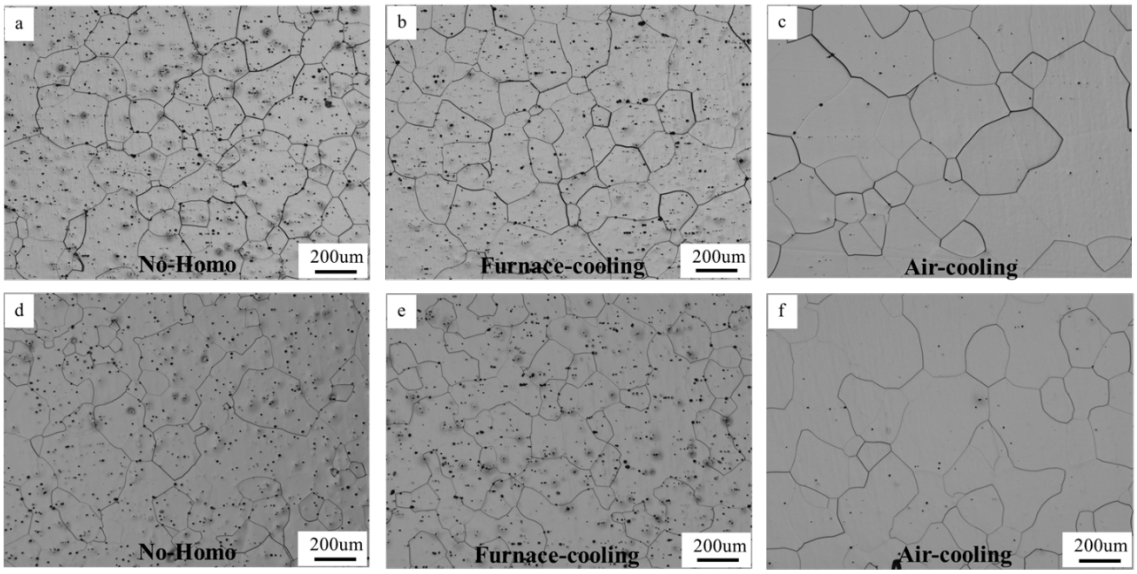

Fig. 23 OM images of the as-quenched (a-c) excess Si and (d-f) balanced alloys with different homogenization treatments: (a,d) without homogenization, (b,e) cooled in the furnace, (c,f) cooled in the air.

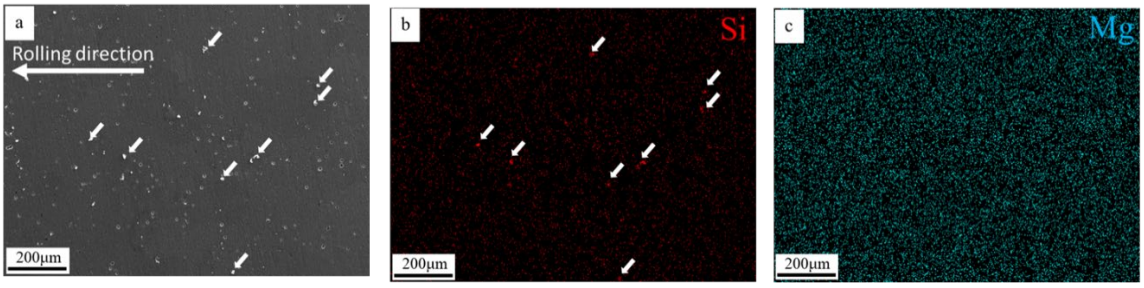

Fig. 24 SEM images and elemental mappings of Si (b), and Mg (c) of the as-quenched excess Si alloy without homogenization treatment.

SEM images and elemental mappings of Si and Mg of the as-quenched excess Si alloy without homogenization treatment is shown in Fig. 24, the elemental mappings confirmed that the Si remained in the samples without homogenization.

Fig. 25 shows the OM images of the air-cooled excess Si samples after solution treatment. As shown in Fig. 25(a), many particles remained, like the water quenched condition. However, under high magnification, rod-like precipitates formed along the rolling direction near the Si particles. This suggests that the distribution of solute atoms is not uniform in the samples without homogenization. For the furnace-cooled or air-cooled samples with homogenization treatment, this phenomenon is not obvious.

For the balanced alloy, as shown in Fig .26, because all the particles are Mg_2Si, compared to the Si particles, the Mg_2Si is relatively easy to dissolve into the matrix, thus, only in the furnace-cooled samples with some coarse Mg_2Si, the heterogenous distribution of the precipitates can be observed.

Fig. 27 shows SEM and TEM images of the air-cooled excess Si samples after solution treatment and cooled in the air, from Fig. 27(a), it can be seen clearly that some precipitates formed along the rolling direction near the Si particles. As shown in Fig .27(c), Si phase can be confirmed, some of the precipitates along the $<100>_{Al}$ directions should be Si phase or Type-A. This suggests that the distribution of the solute atoms, especially the Si atoms, are not uniform in the matrix of the samples without homogenization treatment.

3.3 Effect of homogenization on precipitation behavior during aging treatment

The aging curves of the two alloys during aging at 200 °C was shown in Fig. 28, as can be seen, the air-cooled samples exhibit the highest peak hardness among the three groups, although there is a small difference between the different samples. The lower hardness of the samples without homogenization is due to the remained Si particles in the matrix after solution treatment.

Fig. 29 shows the TEM bright filed images of the peak aged samples without homogenization. As can be seen in Fig. 29(a), all the needle-like precipitates orient in the $<100>_{Al}$ direction, Fig. 29(b) and (c) are magnified region of the marked area in (a), it is obliviously that the length and number density of precipitates are different. As shown in Fig. 29(b) and Fig. 29(c), the precipitates in the area 1 are much coarser while those in the area 2 are much finer.

Fig. 30 shows the comparation of precipitates in the samples with different homogenization treatments. Under the peak aged condition, the distribution of precipitates is similar between the air and furnace cooled samples. Compared to the microstructure of the samples without homogenization, as seen in Fig. 30(a), a denser distribution of precipitates was found in the air/furnace cooled samples. The air-cooled samples contain higher number density of precipitates ($330/um^2$) than the sample without homogenization ($150/um^2$).

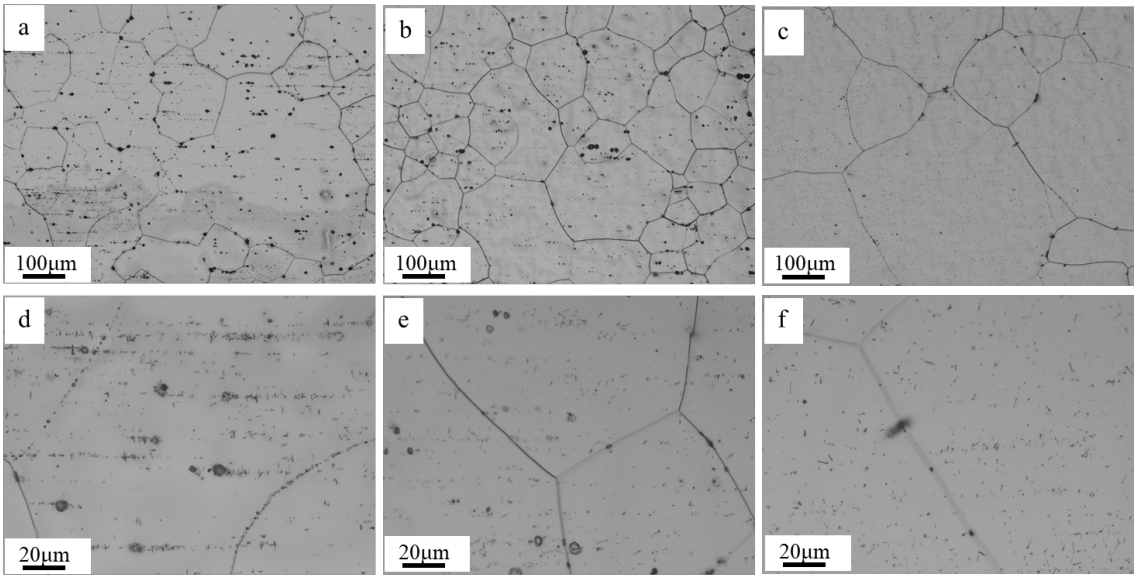

Fig. 25 OM images of the air-quenched excess Si alloy with different homogenization treatments: (a) without homogenization, (b) cooled in the furnace, (c) cooled in the air.

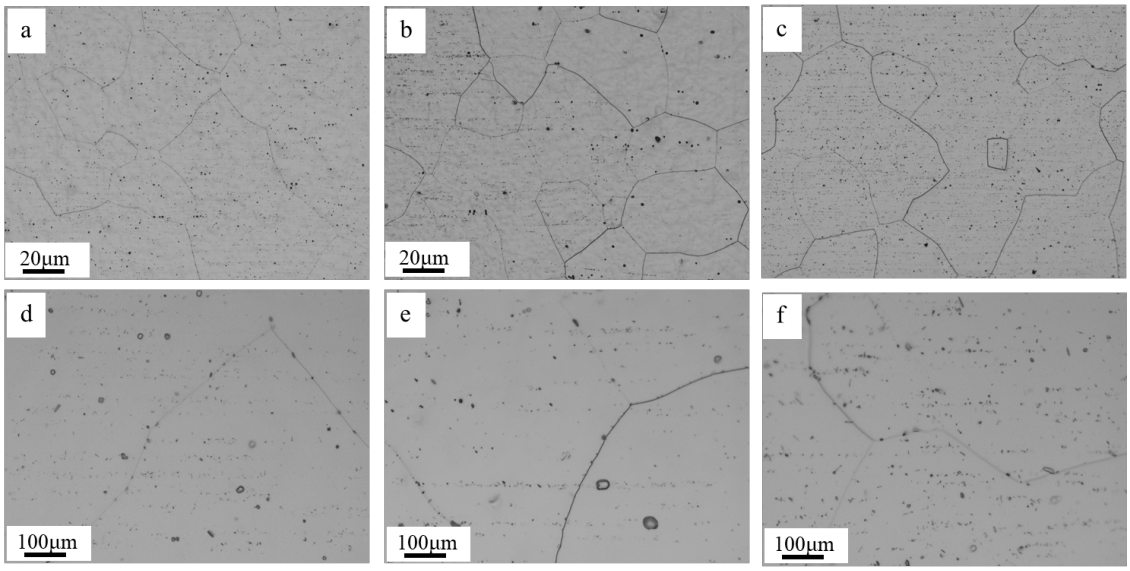

Fig. 26 OM images of the air-quenched balanced alloy with different homogenization treatments: (a) without homogenization, (b) cooled in the furnace, (c) cooled in the air.

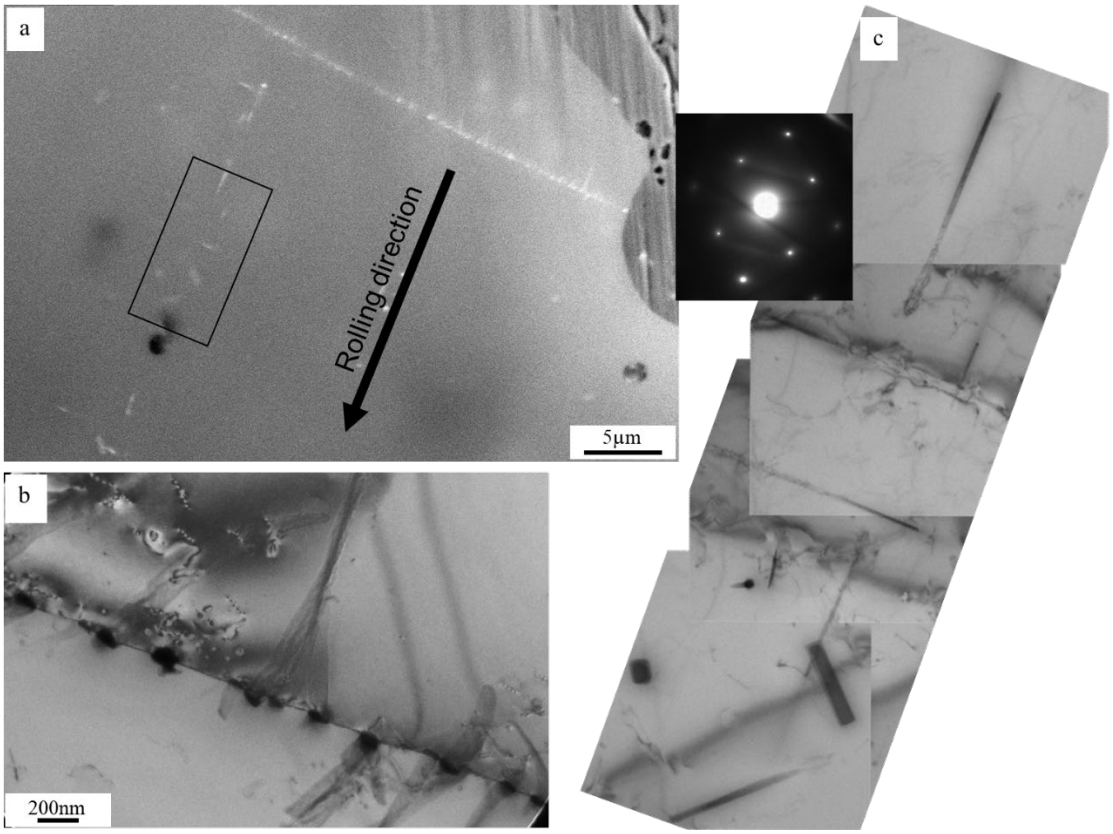

Fig. 27 SEM and TEM images of the air-cooled excess Si alloy without homogenization: (a) SEM image under low magnification, (b) TEM images of the boundary in (a), (c) is magnified region of the marked area in (a).

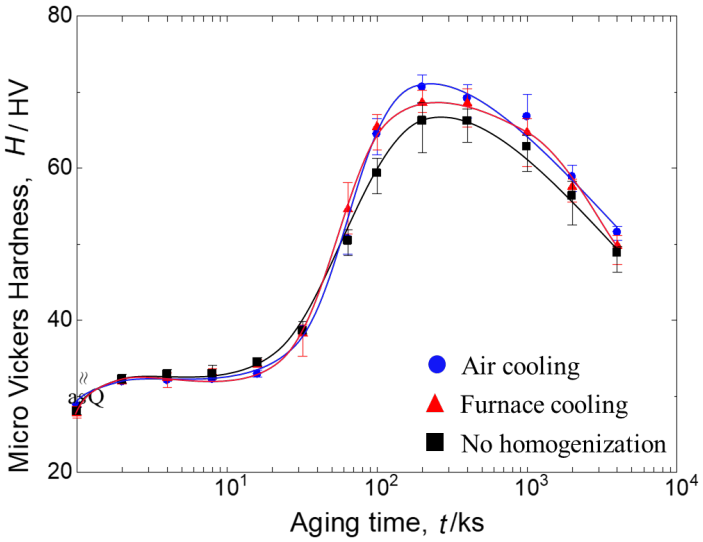

Fig. 28 Hardness curves of the excess Si alloy with different homogenization treatments.

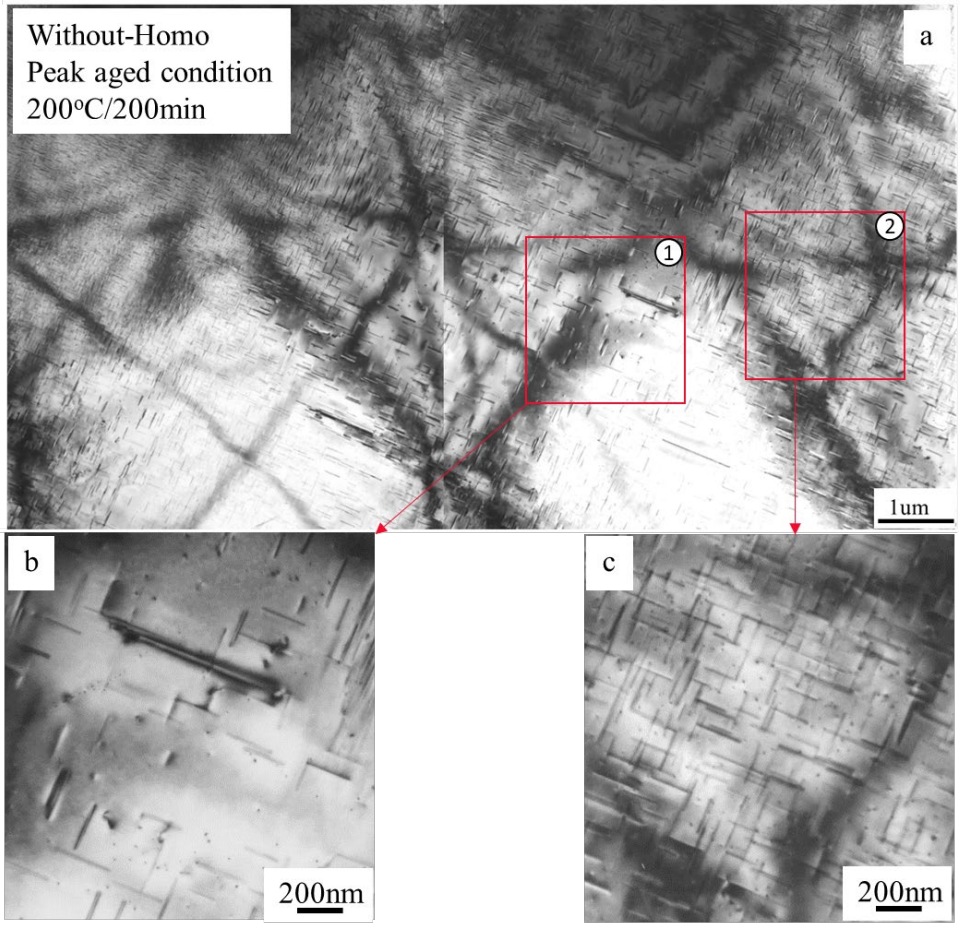

Fig. 29 TEM bright field images of the peak aged excess Si alloys without homogenization treatment

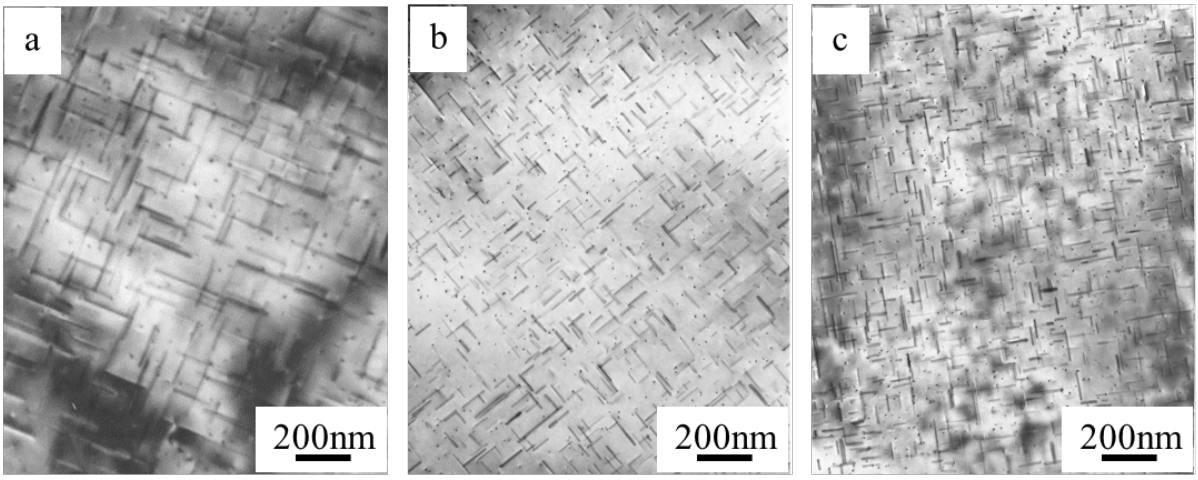

Fig. 30 TEM bright field images of the peak aged excess Si alloys with different homogenization treatments under the same magnification.

3.4 Effect of deformation on microstructure and aging behavior of the Al-Mg-Si and Al-Li-(Cu, Mg) alloys after solution treatment

3.4.1 Al-Mg-Si alloy

The aging curves of the ASR processed samples with different thickness reductions were shown in Fig. 31, when the samples processed by ASR, the peak hardness increases as compared to the as-quenched samples without deformation. with a thickness reduction of 80%, the sample exhibits the highest as-deformed hardness. When aged at 150°C, the highest hardness of the ASR processed sample obtained. While aged at 200°C, the samples reach the peak hardness quickly.

The as-rolled microstructure was shown in Fig. 32, as can be seen, when the samples processed by ASR with the thickness reduction of 80%, the dislocations or sub-boundaries formed in the matrix, from the diffraction patterns, most of the boundaries formed are low angle boundaries.

Fig. 33 shows the microstructure of the ASR processed balanced alloy aged at 200 °C for 16min. As can be seen, the low angle boundaries are visible in the matrix, some coarse precipitates together with the string-like precipitates can be observed within the sub-grain.

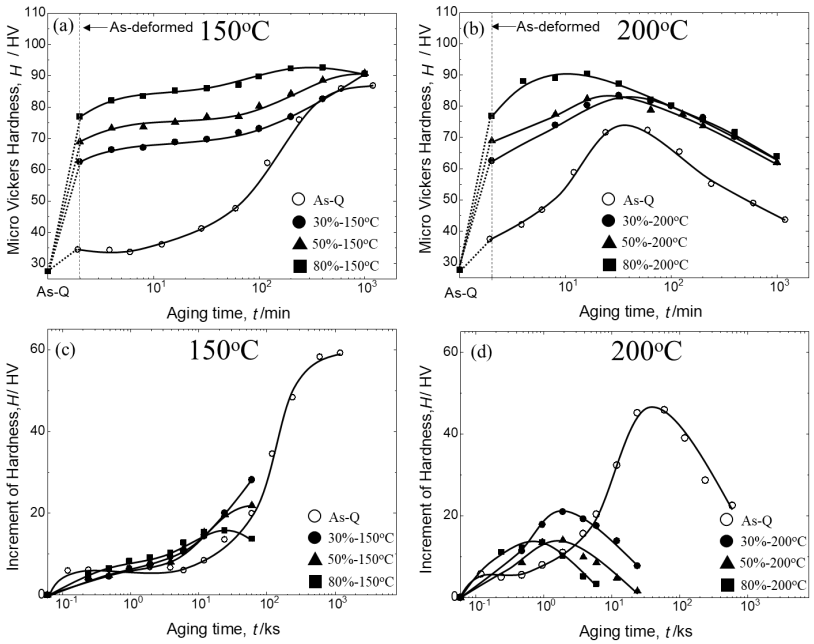

Fig. 31 Age hardening behavior of the ASR processed balanced alloy with different thickness reductions.

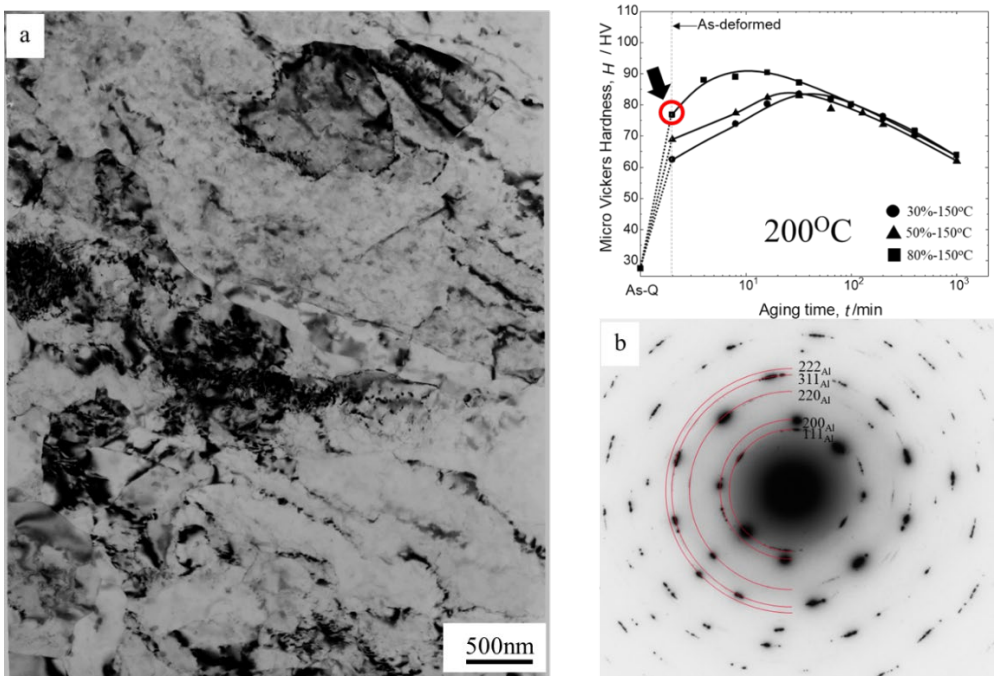

Fig. 32 TEM images of the ASR processed balanced alloy with a thickness reduction of 80%.

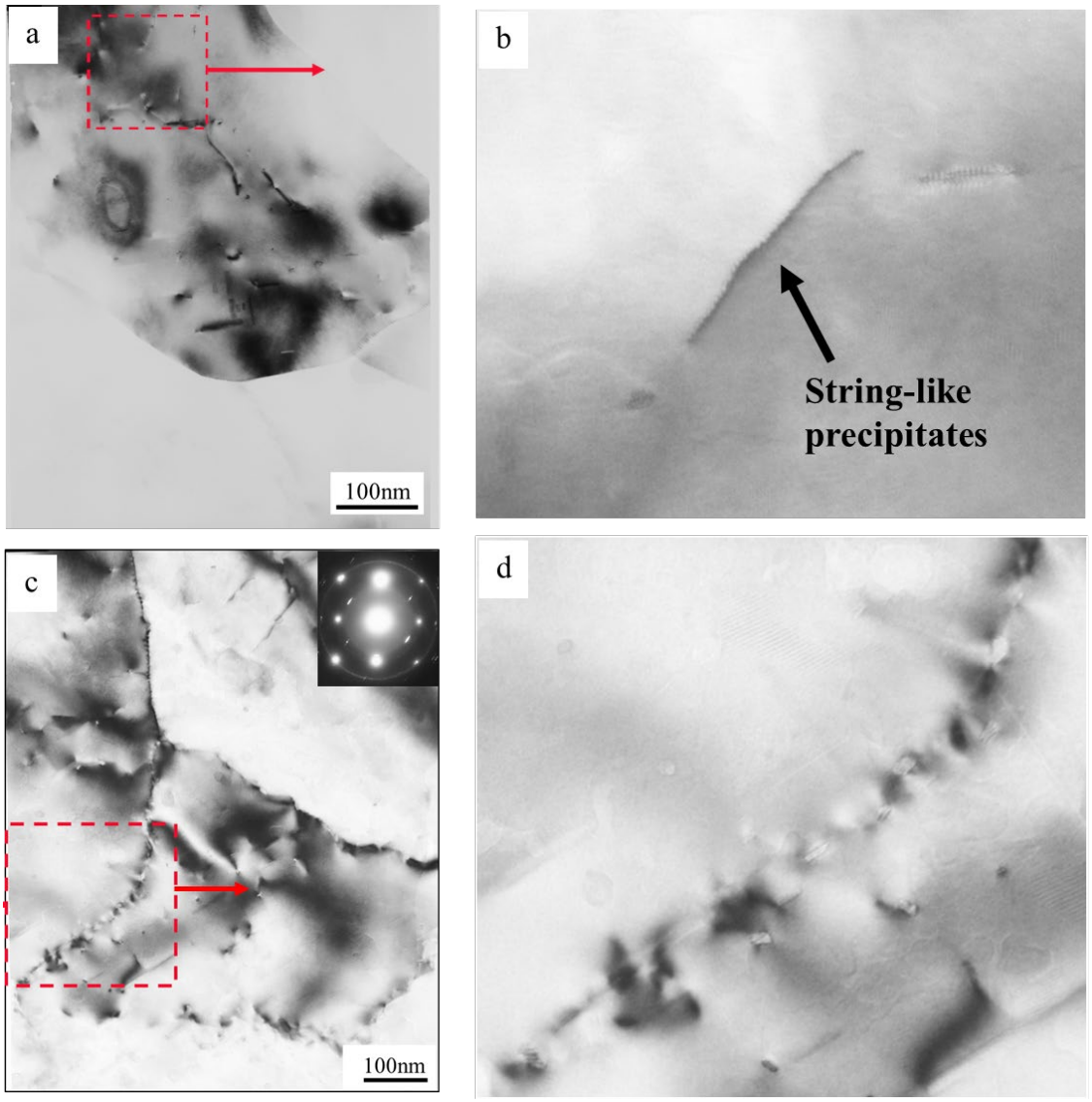

Fig. 33 TEM images of the as-deformed balanced alloy after aging at 200°C/16min: (b), (d) are magnified region from (a), (c).

Also, along the dislocations and inside the grains, many rod-like precipitates grow along the same needle direction. As shown in Fig. 33(c), the precipitates tend to form along the dislocations in one direction.

3.4.2 Al-Li-(Cu, Mg) alloys

Fig. 34 shows the hardness of the three alloys processed by different deformation methods. It can be seen that the as-quenched hardness of the Mg and Cu added alloys was higher than that of Al-Li alloy. The as-deformed hardness of all alloys increased with increasing the ε and finally saturated to the steady state at large strains where the hardness remained unchanged with further straining. Addition of alloying element also increased the hardness under the same ε, Al-Li-Cu alloy showed the highest hardness among alloys. As shown in Fig. 34, under the same thickness reduction, the ε introduced by ASR is higher than CR and the ASR samples showed higher as-deformed hardness level than the CR samples, i. e., the hardness of the Al-Li-Mg alloy after ASR was about 125 HV, while the hardness after CR was about 103 HV. Compared to ASR and CR, the HPT significantly increased the hardness after deformation, in particular, for the alloys with addition of Cu or Mg.

As shown in Table 3, the aging temperature for the cold rolled and asymmetric rolled samples was 200 ^{o}C, however, for the HPT processed samples, the aging temperature was 150 ^{o}C, as can be seen in Fig. 35, the increment of the hardness decreased with increasing the aging temperature, when the samples were aged at 70 ^{o}C, although a higher increment of the hardness can be obtained, it takes a long time to reach the peak condition(for example, 277 days for the Al-Li-Mg alloy), in order to get higher age-hardenability, 150 ^{o}C was chosen to age the HPT processed samples and observe the microstructures.

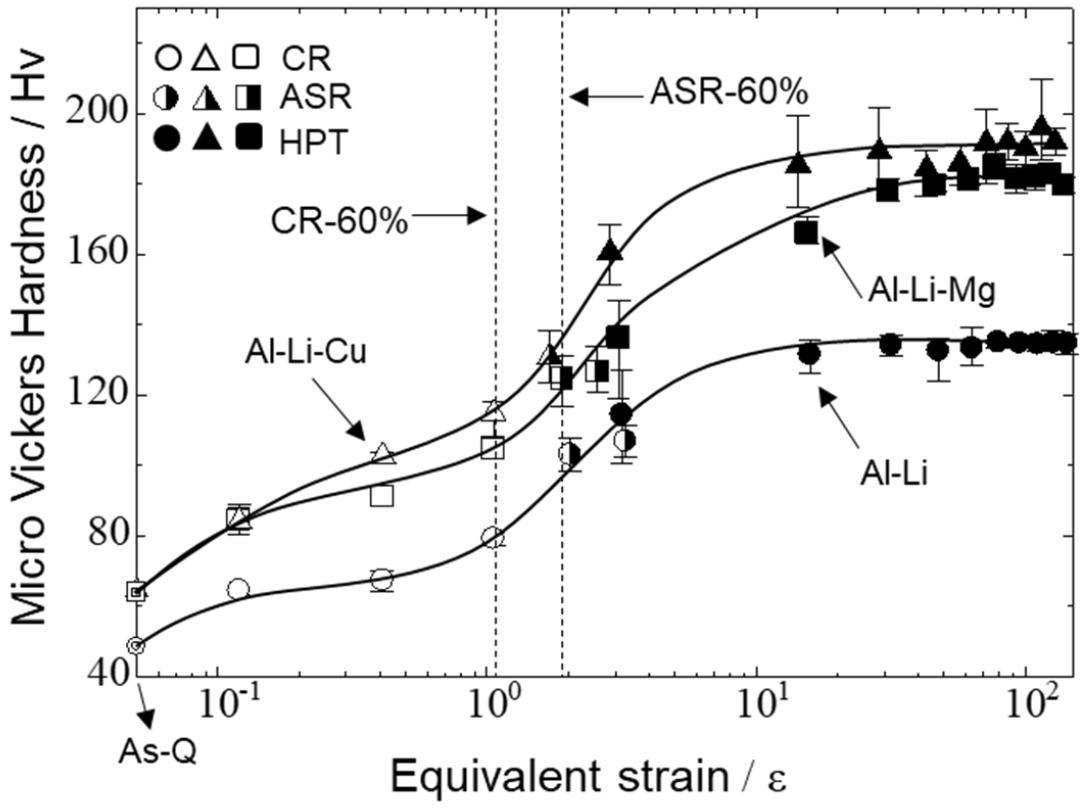

Fig. 34 Micro Vickers hardness as a function of the equivalent strain (ε) in the CR, ASR and HPT processed samples.

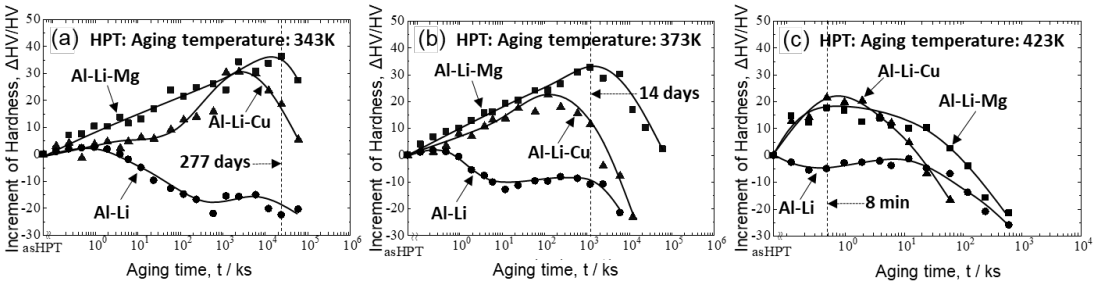

Fig. 35 Aging hardening abilities of the HPT processed Al-Li, Al-Li-Mg and Al-Li-Cu alloys aged at 70 ºC, 100 ºC and 150 ºC.

Fig. 34 shows the age hardening behavior of the three alloys with and without deformations. The aging temperature for the undeformed, ASR and CR samples was 200 ºC and for the HPT sample was 150 ºC. In Fig. 36(a), the as-HPT sample showed a high initial hardness value (127 HV), however, aging at 150 ºC decreased the hardness. For the ASR and CR samples, there was a significant increase in hardness during aging. The peak hardness value of the ASR samples was 140 HV, which was higher than that of the peak-aged sample without deformation (117 HV) and samples processed by HPT. It is noteworthy that the ASR sample exhibited the highest peak hardness in the Al-Li binary alloy. As shown in Fig. 36(b), the peak hardness of the Al-Li-Mg alloy reached almost the same level as that of the Al-Li alloy under the undeformed condition, hardness of all the deformed Al-Li-Mg samples can be increased by aging treatment and the peak-hardness increased with increasing the ε. Addition of Mg not only increased the as-deformed hardness but also made the HPT processed samples obtained age-hardenability. The aging behavior of the Al-Li-Cu alloy was shown in Fig. 36(c), with the addition of Cu, the peak-hardness of the undeformed samples was higher than the undeformed Al-Li and Al-Li-Mg alloys. Different to the Al-Li-Mg alloy, there was a small difference between the peak hardness of the ASR and CR samples in Al-Li-Cu alloy. For all alloys, the peak hardness of deformed samples was higher than that without deformation, regardless of the alloy composition. Also, the peak hardness occurred earlier in the deformed samples. In contrast to the Al-Li alloy, the highest peak-aged hardness for Al-Li-Mg, Al-Li-Cu and Al-Li-Cu-Mg alloys was obtained by HPT and subsequent aging treatment.

Fig. 37 shows the age-hardenability of the alloys with and without deformations, the age-hardenability was evaluated by the increment of the hardness, as can be seen, the as-

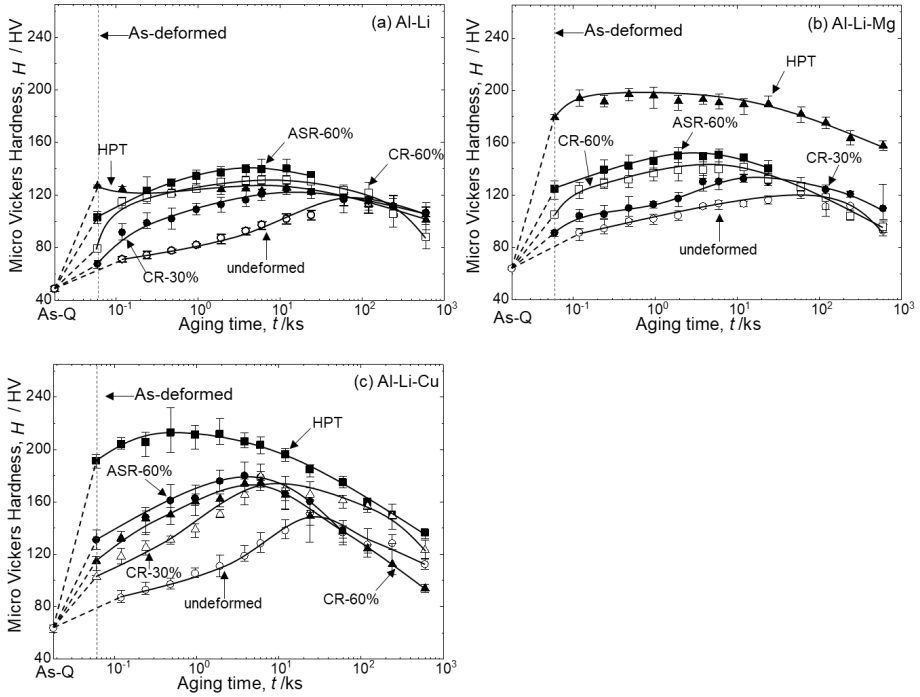

Fig. 36 Age hardening behavior of the (a) Al-Li, (b) Al-Li-Mg and Al-Li-Cu alloys with and without deformations.

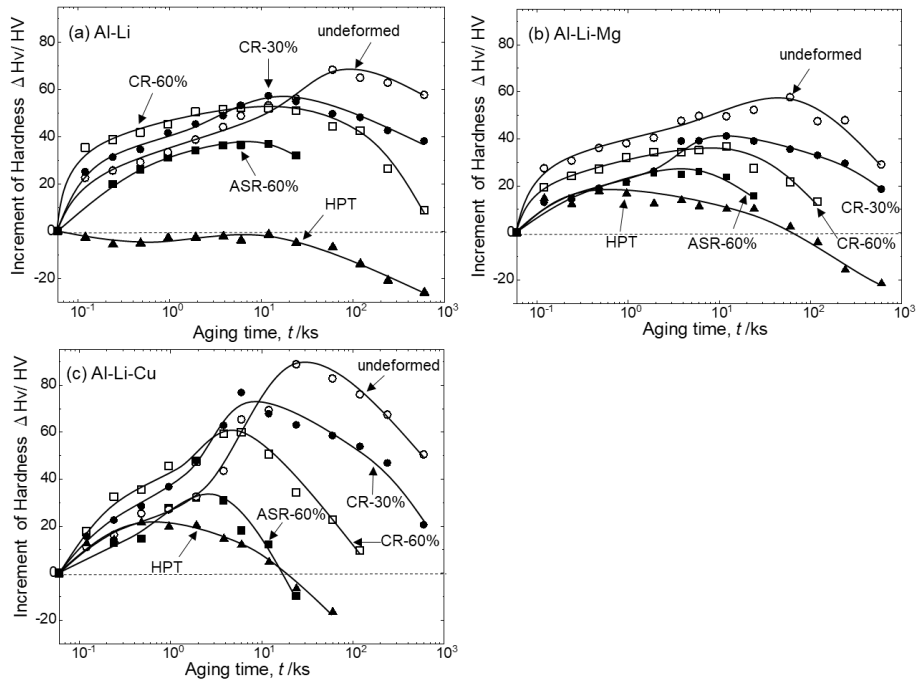

Fig. 37 Aging hardening abilities of the (a) Al-Li, (b) Al-Li-Mg and Al-Li-Cu alloys with and without deformations.

quenched alloys possessed the largest age-hardenability in all the alloys. However, as shown in Fig. 36 (a) and (c), before 3.84 ks, the age-hardening rate in CR processed Al-Li and Al-Li-Cu alloys was higher than that after quenching. Although high values of hardness were achieved by HPT processing, the age-hardenability of the HPT processed alloys was the lowest.

Fig. 38 shows TEM images of the as-quenched and peak-aged samples. It can be found that relatively small δ' phase formed in the matrix of all the alloys during quenching or immediately after quenching, as shown in Fig. 38(a), (e) and (i). The metastable δ' phase has an L12 superlattice crystal structure and is coherent with the matrix [16]. Previous investigations have shown that the δ' phase already precipitates in the as-quenched stage due to the δ' phase small lattice misfit and low interfacial energy [16]. The reported behaviors are in agreement with the results obtained here for the three alloys containing more than 2wt%-Li. In the as-quenched state, the number density of the δ' phase was about 5400/μm^2, 7000/μm^2 and 5100/μm^2 in the Al- Li, Al-Li-Cu and Al-Li-Mg alloys, after aging treatment, the number density of the peak-aged alloys decreased to about 680/μm^2, 470/μm^2 and 600/μm^2, respectively.

As shown in Fig. 38(c), (g) and (k), the spherical δ' phase was observed in all the peak-aged alloys. The average size of the δ' phase in the Al-Li and Al-Li-Cu alloys was about 28nm. With the addition of Mg, the size of the δ' phase increased to about 31 nm under the peak-aged condition. In addition, T_1 (Al_2CuLi) and θ'

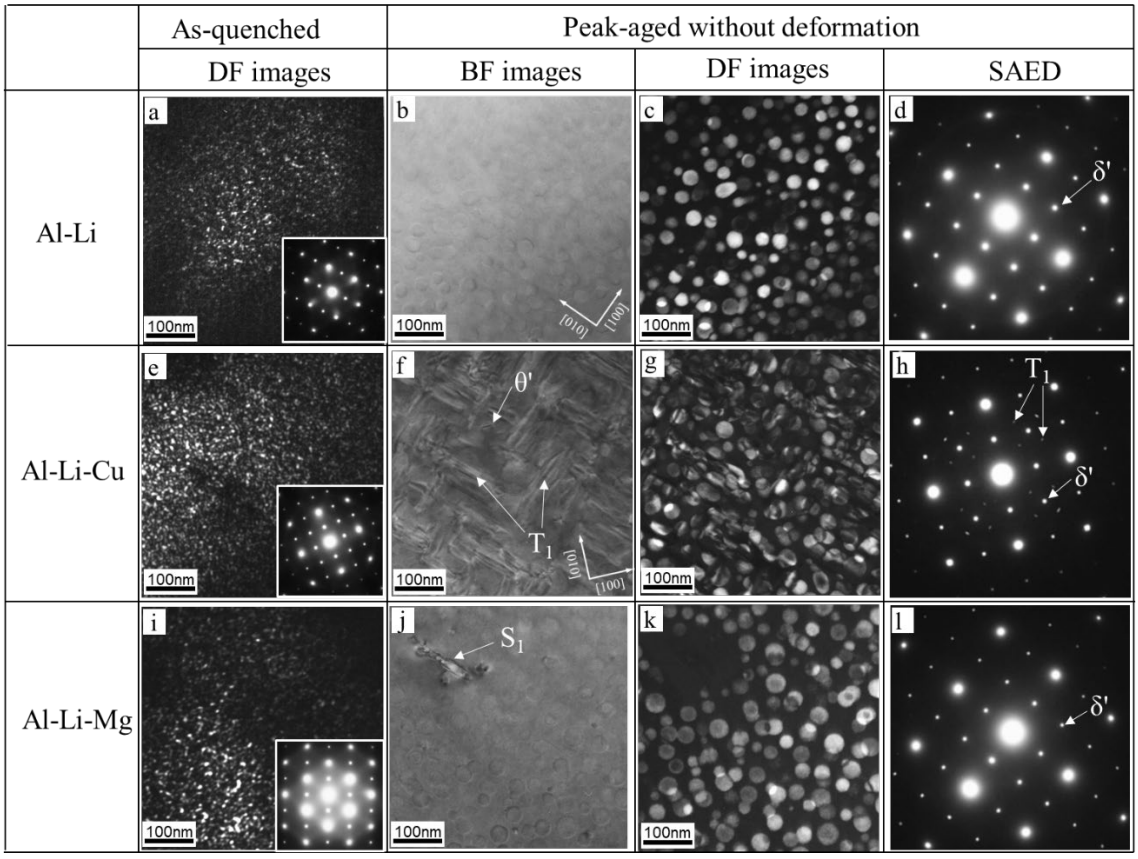

Fig. 38 TEM images of the as-quenched and peak-aged samples of (a-d) Al-Li, (e-h) Al-Li-Cu and (i-l) Al-Li-Mg alloys. Aging condition for the Al-Li and Al-Li-Cu alloys was 200 °C/60ks, for the Al-Li-Cu was 200 °C/24ks.

(Al_2Cu) phases also precipitated from the matrix of Al-Li-Cu alloy during aging. The θ' precipitates are rarely observed, in which the δ' and T_1 phase were the two main strengthening precipitates types. For the Al-Li-Mg alloy, the stable S_1 (Al_2MgLi) phase was occasionally found in the peak-aged condition, as marked with arrow in Fig. 38(j). From the dark filed image, Fig. 38(k), it is clear that the S_1 phase was surrounded by δ'-precipitate-free zones (PFZ).

The as-deformed microstructure of the HPT and ASR samples is shown in Fig. 39. As seen from Fig. 39(a)-(c), equiaxed ultrafine grains formed during HPT process. The average grain size of the Al-Li, Al-Li-Mg and Al-Li-Cu alloy was about 210 nm, 150 nm and 120 nm, respectively. Thus, the addition of Mg or Cu promoted the formation of a finer grain structure during HPT process. Fig. 39(d)-(f) shows the microstructure after the ASR. Due to the introduced equivalent strain by ASR is lower than HPT, it is not shown the fully recrystallized structure like the HPT processed microstructure. It is possible to observe some sub-grains and dislocation cell (or tangled dislocation).

Fig. 40 shows the selected area electron diffraction (SAED) patterns of the three alloys after deformations. Based on Fig. 40(a), (b) and (c), most of these grains in ASR processed alloys were separated by low-angle boundaries due to the ASR introduced ε was low. However, the SAED pattern of the HPT processed Al-Li alloy in Fig. 40(d) exhibited rings indicative of grains separated by boundaries having high angles of misorientation. Also, the δ' phase can be detected from all the deformed samples, it means that δ' phase existed in the as-deformed alloys.

Fig. 41 shows the microstructures of the three alloys after deformation and subsequent aging treatment. The dark filed images revealed that, under the peak-aged

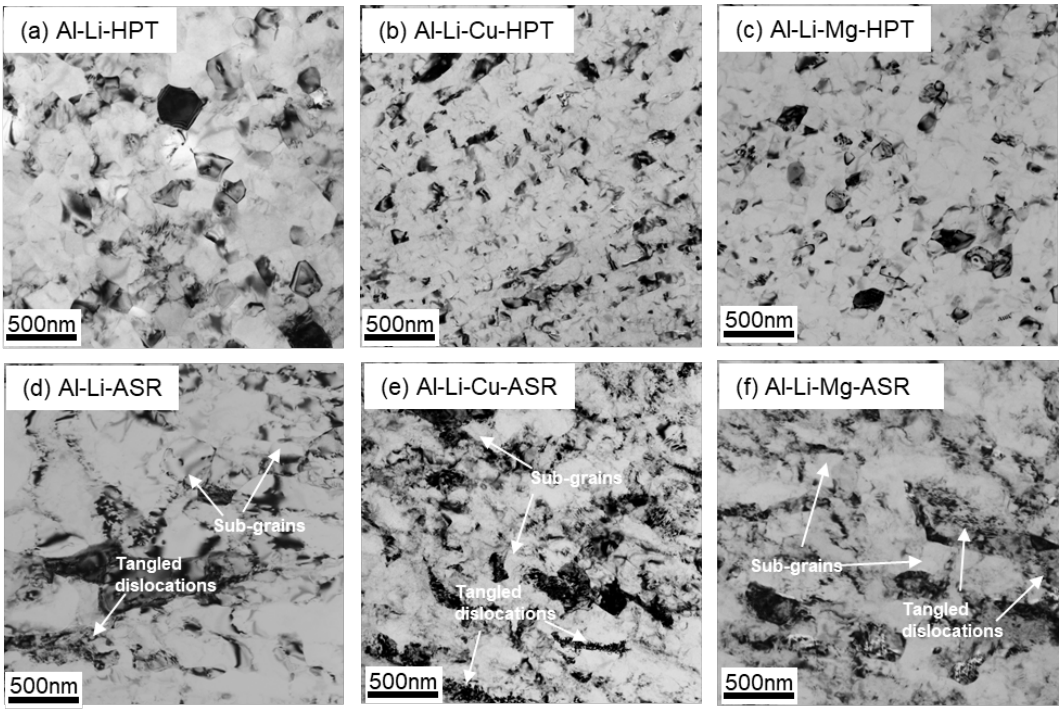

Fig. 39 TEM micrographs of the Al-Li, Al-Li-Cu and Al-Li-Mg alloys processed by (a-c) HPT and (d-f) ASR.

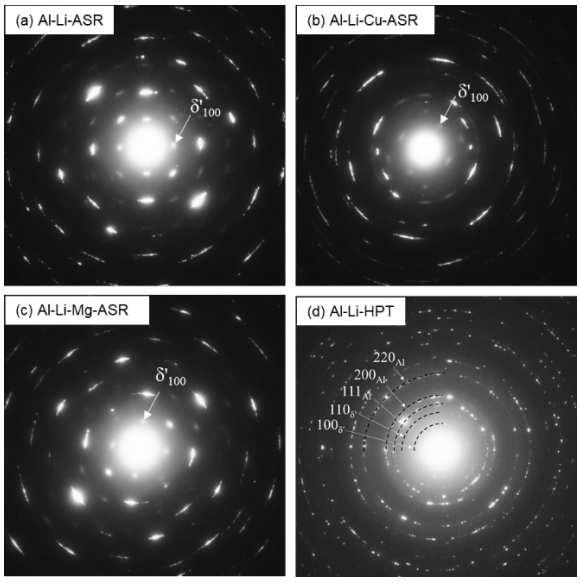

Fig. 40 SAED patterns of the ASR processed (a)Al-Li, (b) Al-Li-Cu, (c) Al-Li-Mg alloys and (d) HPT processed Al-Li alloy. (a), (b), (c) and (d) is the corresponding SAED patterns of Fig. 22 (d), (e), (f) and (a).

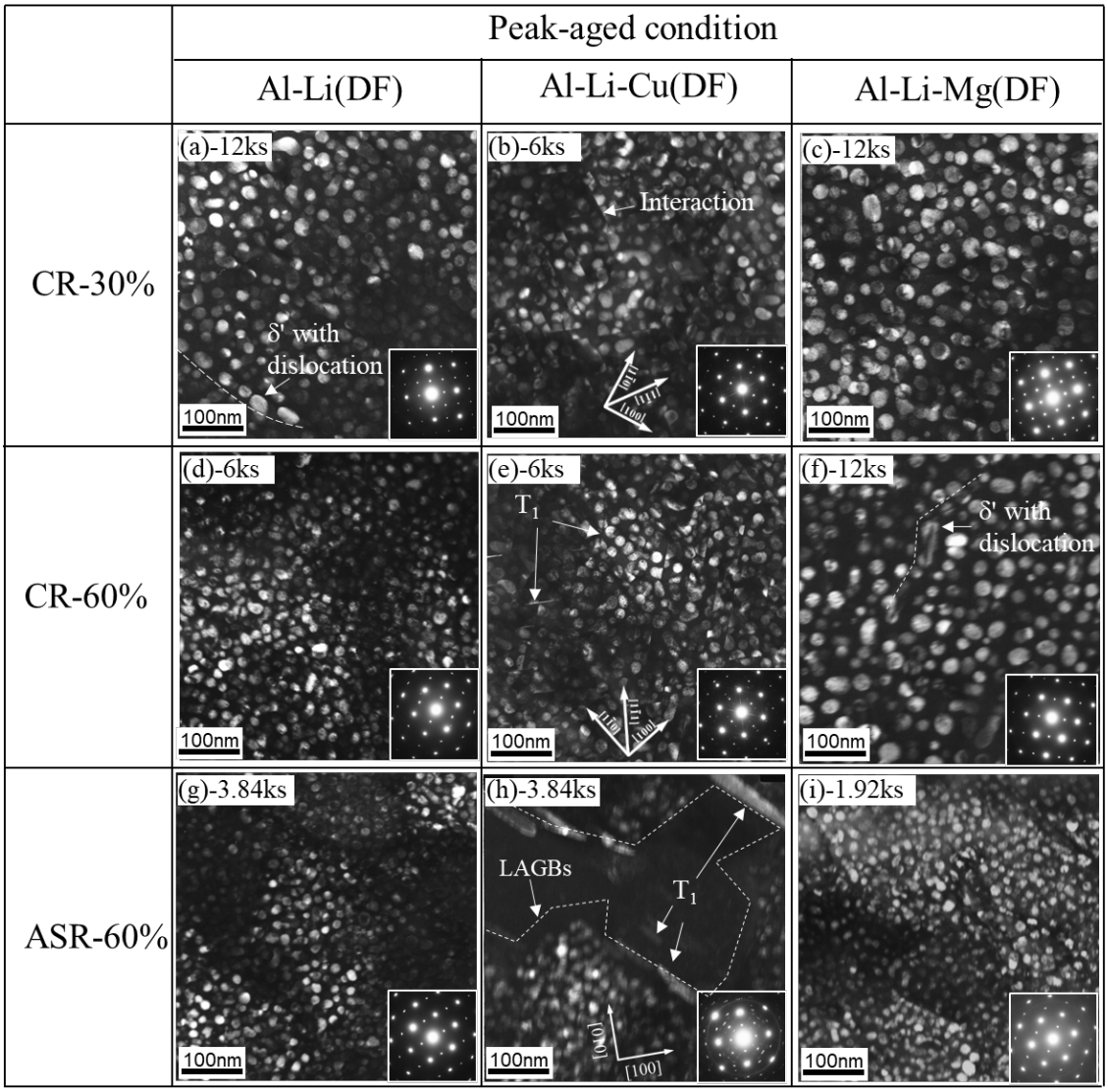

Fig. 41 TEM dark filed images of the peak-aged samples. The corresponding SAED patterns were shown in the insets in the lower right. Aging temperature for all the samples was 200°C.

condition, the average size of the δ' phase decreased with increasing the ε. Obvious growth of the δ' phase was confirmed in the CR processed alloys because of the prolonged aging time. As shown in Fig. 41(a), (c) and (d), (f), under the same aging condition, the average sizes of the δ' phase in the Al-Li-Mg alloy processed by CR are also larger than that in Al-Li alloy. At the same time, the larger δ' phase is visible along the dislocations. The average size of the δ' phase will be discussed later. For the peak-aged Al-Li-Cu alloy, the T_1 phase formed in the CR and ASR samples, as shown in Fig. 41(b) and (e), severe interactions of the T_1 with the δ' could be easily identified. In the ASR sample, except the finer T_1 phase in the grain interior, the coarsening of the T_1 precipitates adjacent to low angle grain boundaries (LAGBs) during aging was also found, as shown in Fig. 41(h).

The HPT processed samples are shown in Fig. 42. As seen in Fig. 42(a)-(f), the δ' can be detected in the grains of the as-HPT samples. Because of the irregular morphology, the size of the δ' phase in the as-HPT sample is not given here. As shown in Fig. 42(h), the T_1 phase was not detected in the grain interior of the peak-aged HPT sample of Al-Li-Cu. This suggested that only δ' phase contributed to increase the hardness in the Al-Li-Cu and Al-Li-Mg alloys.

Fig. 43 shows the microstructure of the three alloys under over-aged condition. When the aging time increased to 60ks, obvious growth of the δ' phase can be observed in the grains as compared to the peak-aged samples. As seen in Fig. 43(g)-(i), the precipitate formed within grain interiors was only δ' phase in the Al-Li and Al-Li-Mg alloys. For the Al-Li-Cu alloy, as shown in Fig. 43 (b) and (h), the T_1 phase was detected in the grains. With the addition of Mg, as shown in Fig. 42(f), the S_1 phase is found at the grain boundaries and a PFZ zones of δ' phase formed around the S_1 phase, The larger size

of the δ' phase near the PFZ zones due to a lower nucleation density adjacent to the PFZ such that fewer precipitates form and subsequently grow to a larger size during aging. Alternatively, the precipitates bordering the PFZ may draw solute from within the PFZ and grow larger compared to the precipitates deeper within the grains [63].

Fig. 44 shows the grain size as function of aging time. In case of the HPT samples, when the aging time was 0.48 ks, the average grain size of the Al-Li alloy increased slightly, however, the Cu and Mg added alloys was unchanged. For the Al-Li alloy, the average grain size increased from about 210 nm to 400 nm after aging at 150 °C for 600 ks. Under the same aging condition, the average grain size of the Al-Li-Cu and Al-Li-Mg alloys only increased to about 210 nm and 220 nm, respectively. It suggested that the grain growth of the Al-Li-Cu and Al-Li-Mg alloys was suppressed. As shown in the Fig. 44, recrystallized grains and dislocation cell sizes of the Cu and Mg added alloys are also smaller than the Al-Li alloy.

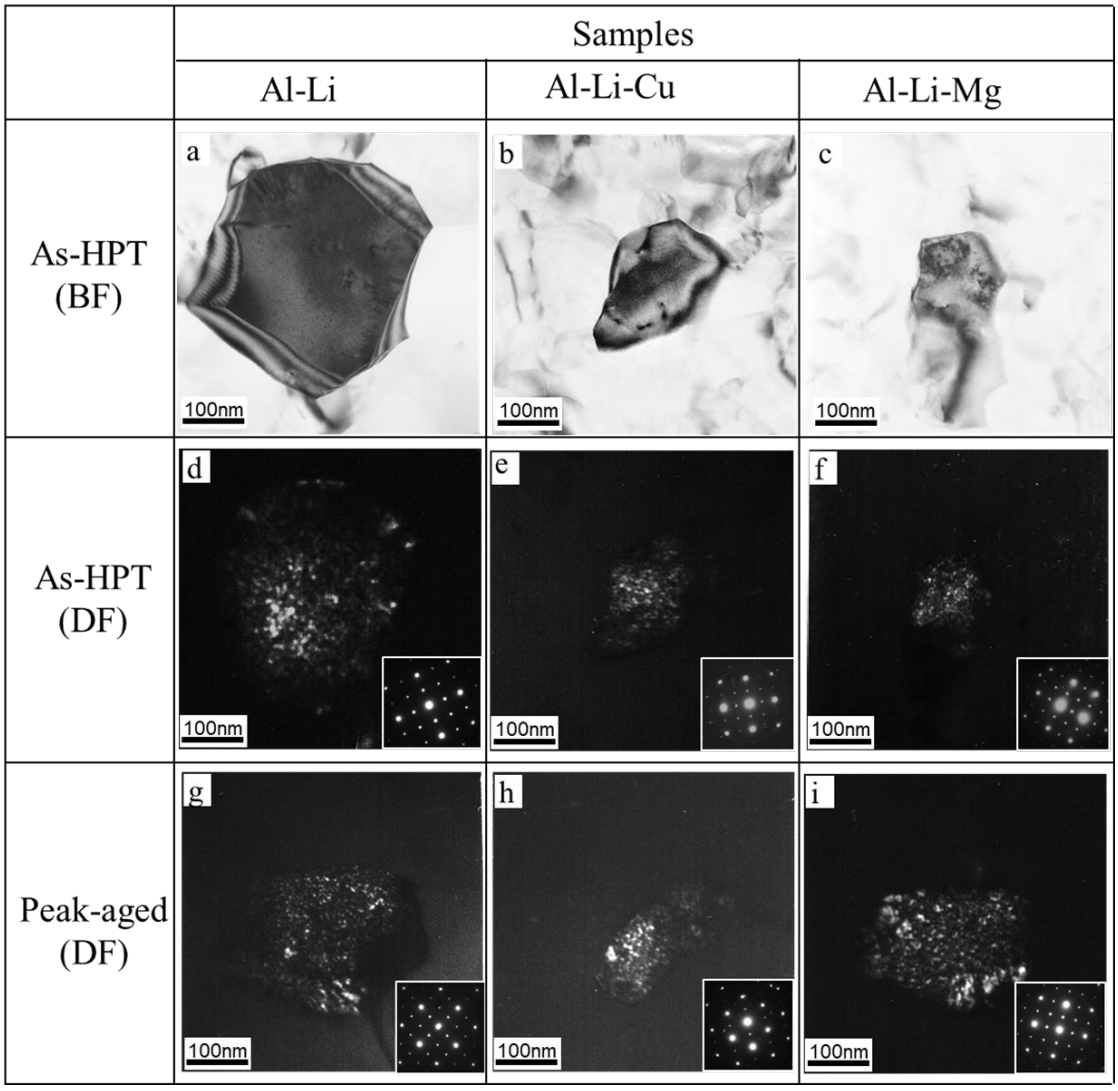

Fig. 42 TEM bright field and dark filed images of the three alloys after (a-f) HPT and (g-i) HPT and aged at 150 ^{o}C for 0.48 ks. The corresponding SAED patterns were shown in the insets in the lower right of the dark filed images.

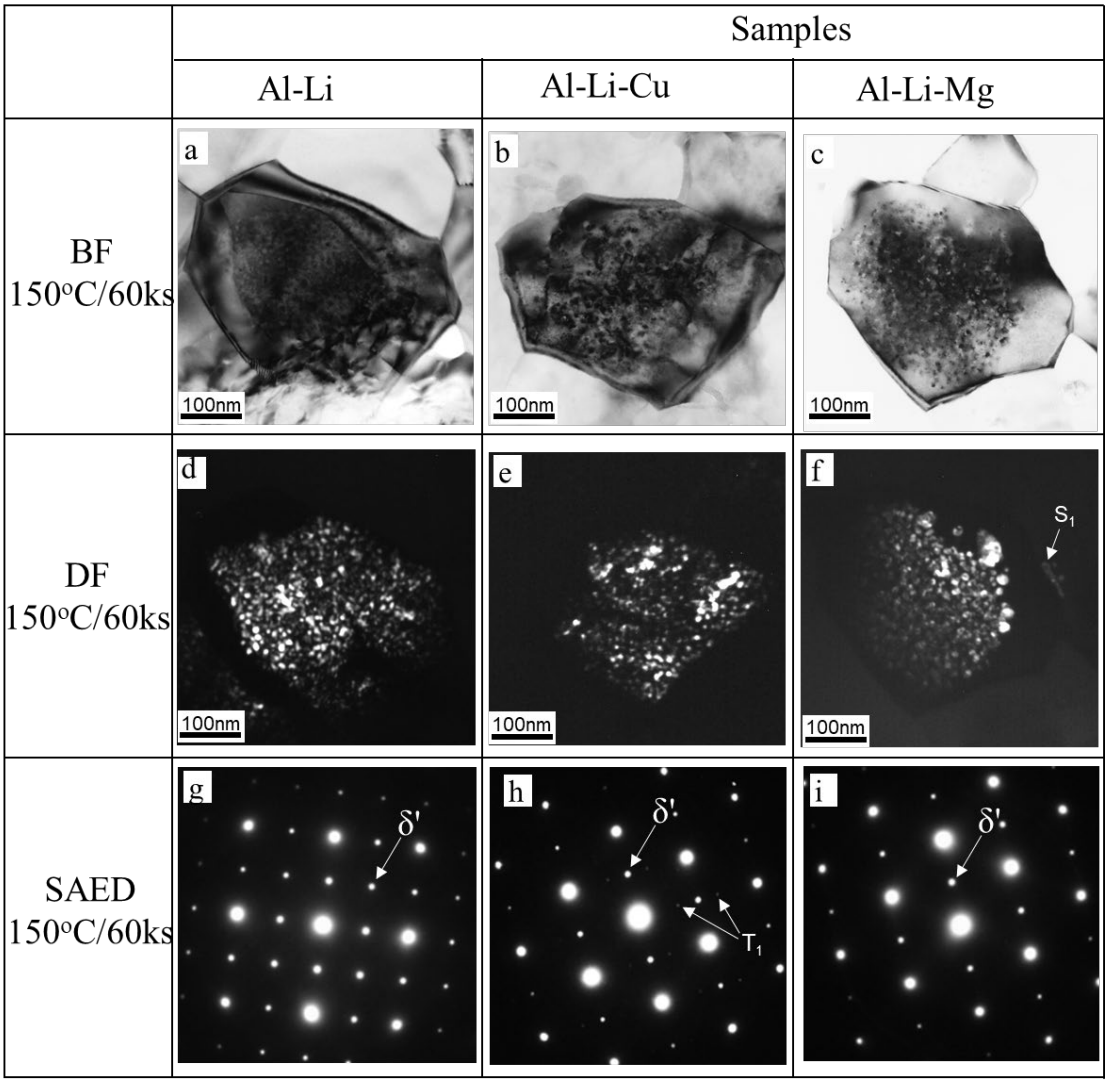

Fig. 43 TEM bright field, dark filed images and SAED patterns of the three alloys after HPT and aged at 150°C for 60 ks (over-aged condition). The SAED patterns were taken from the grain interior.

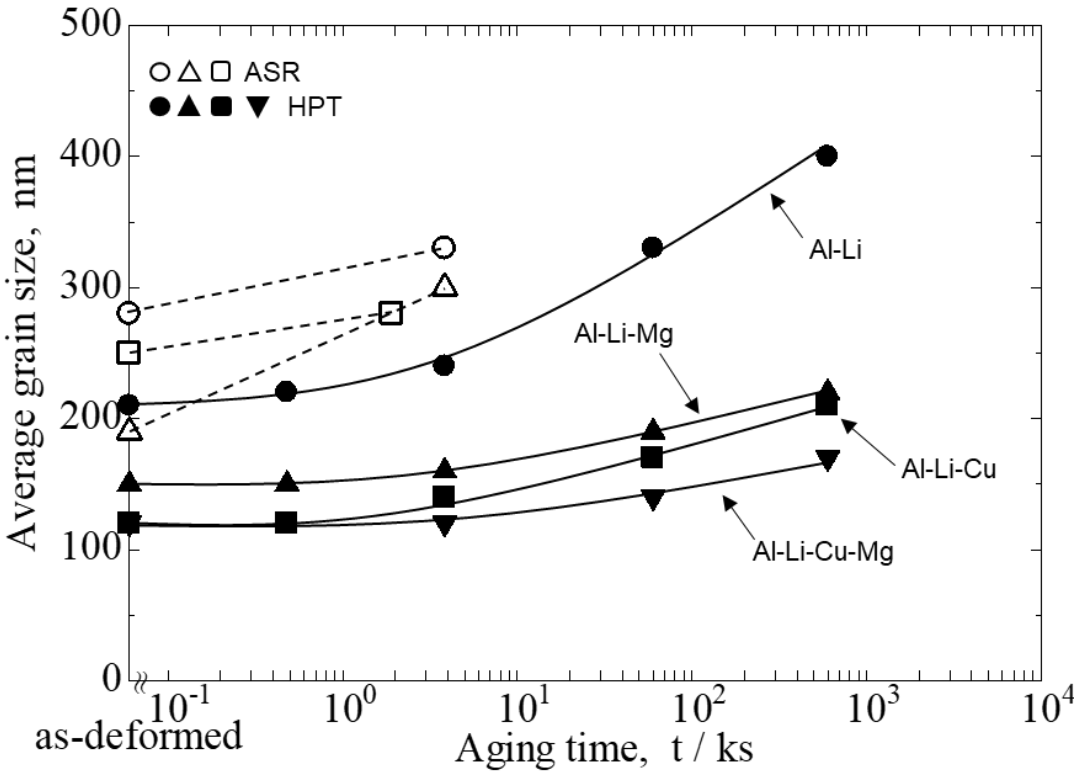

Fig. 44 The grain size of the HPT and ASR processed Al-Li-(Mg, Cu) alloys during aging treatment.

	δ' size (nm)				
	without deformation		CR/60%	ASR	HPT
	AS-Q	Peak-aged	Peak-aged	Peak-aged	Peak-aged
Al-Li	~4.6	~28	~17	~12	~4.5
Al-Li-Cu	~4.6	~28	~18	~14	~4.6
Al-Li-Mg	~5.4	~31	~22	~12	~4.5

Table 4 The average size of δ' phase

	without deformation			CR			ASR			HPT		
	AS-Q	Peak-aged	ΔHV	AS-CR 10 / 30 / 60%	Peak-aged 10 / 30 / 60%	ΔHV 10 / 30 / 60%	AS-ASR	Peak-aged	ΔHV	AS-HPT	Peak-aged	ΔHV
Al-Li	48	117	69	65/67/79	119/125/131	54/60/52	103	140	37	127	127	0
Al-Li-Cu	63	151	88	84/103/115	163/179/175	79/76/60	131	180	49	191	213	22
Al-Li-Mg	64	121	57	85/91/105	125/132/141	40/41/36	125	150	25	179	197	18

Table 5 Summary of hardness variations (HV)

4. Discussion

4.1 Heterogeneous precipitation mechanism in air-cooled Al-Mg-Si alloys

According to the observations above, the different heterogenous precipitation behavior of the Al-Mg-Si alloys between homogenization air-cooling and aging treatment are due to the presence of dislocations. As shown in Fig. 44, the illustration of the precipitates formation mechanism during air-cooling was supposed, as shown in Fig. 44(a), before homogenization, there are many particles exist in the as-cast billets. During homogenization treatment, these particles are dissolved into the matrix. Before or during cooling, many dislocations formed within the grains. As the temperature decreases to near the solvus line, the precipitates nucleate preferentially at the dislocations due to the dislocations can act as heterogeneous nucleation site for the precipitates.

When dislocations form in stages 1 to 3 or the dislocations remained from as-cast matrix, it is easy for the dislocations to glide or climb under the elevated temperature. Thus, these dislocations exhibit a wave shape, as shown in Fig. 16(d). At the same time, due to the glide of the dislocations, the precipitates will along different directions. As the temperature continuous to decrease, when the dislocations form at lower temperatures, for examples, stage 4, the new formed dislocations cannot glide or slide any more, this will cause the change of the distribution of the precipitates, the precipitates will parallel to each other in one direction. The precipitation behaviour is similar to that during aging treatment at this temperature.

Unlike the dislocations induced by deformation before aging treatment, the dislocations form during cooling is more stable and difficult to annihilation, thus, at the end of the cooling stage, the under aged string-like precipitates can form along the

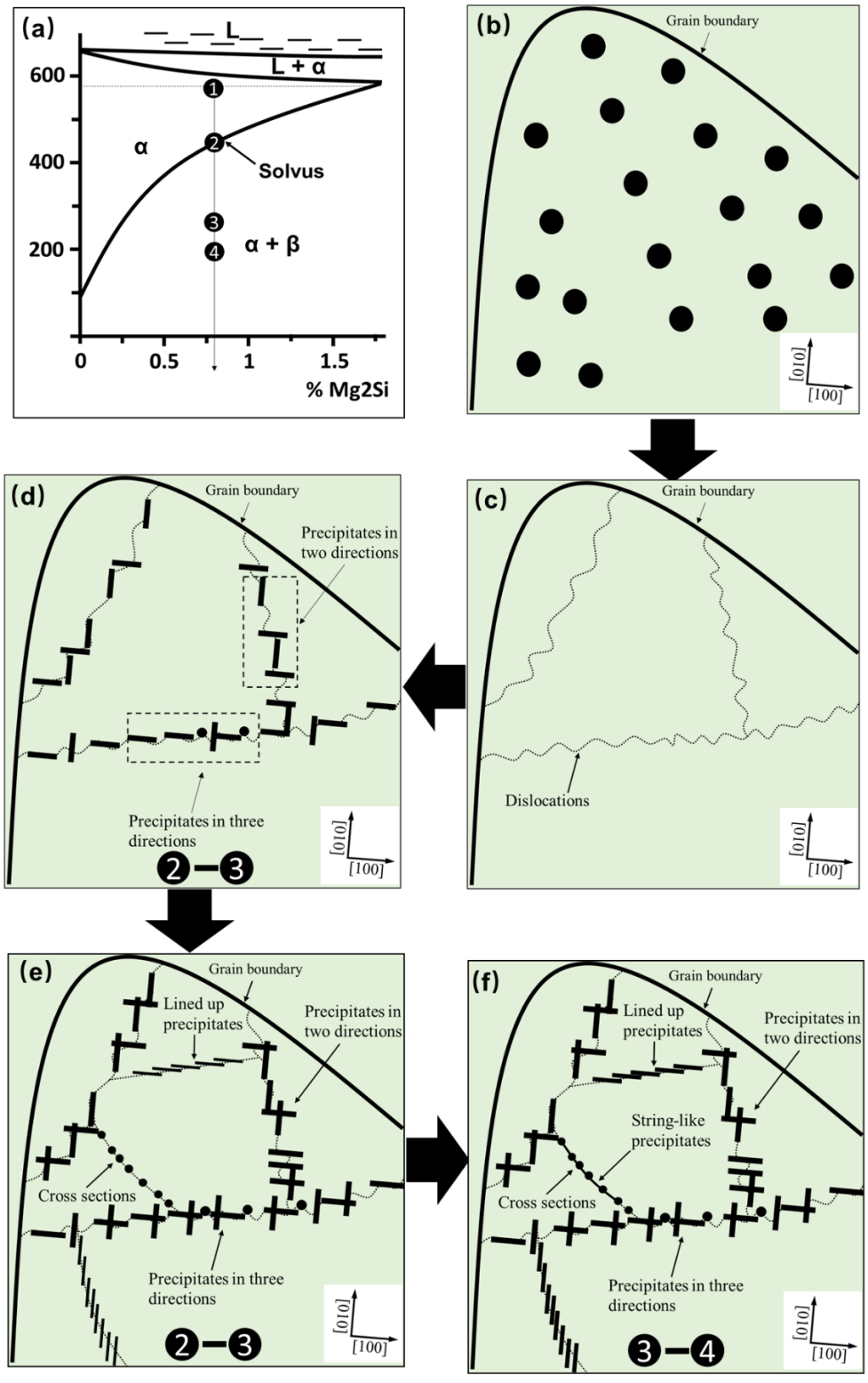

Fig. 45 Schematic quasi-binary phase diagram and schematic illustration of the evolution of the microstructure during homogenization air-cooling in the Al-Mg-Si alloys.

dislocations between the precipitates. When the temperature decreases to near 200 °C, the string-like precipitates will form along the dislocations between the precipitates. Thus, after homogenization air-cooling, the microstructure is like Fig. 45(f). Both the under aged and over aged precipitates can be found together in the matrix after homogenization along the dislocations.

Before or during cooling, the climb (and slide) of the dislocations occurred, as shown in Fig. 16(d), for the Al-Mg-Si alloys, $<100>_{Al}$ directions are usually during the cooling stage, the precipitates firstly nucleated on the most favored condition, as reported previously, take the Q (Type-C) phase for an example, the most favorable condition for nucleation on dislocations corresponds to the situation where the maximum misfit vector of the precipitates is parallel or nearly parallel to the burger vector, also the dislocations line lie in direction lies in the habit plane of the precipitates [63]. Obviously, some segments of the dislocations are along the $<100>_{Al}$ directions, they are the favorable sites for the nucleation of the precipitates.

4.2 Effect of homogenization on subsequent processing

Fig. 46 shows the schematic illustration of the effect of homogenization on subsequent processing in the excess Si alloys. For the samples without homogenization, as seen in Fig. 46(g) and (f)-(h), when the as-cast samples subjected to hot extrusion and rolling, many as-cast particles remained, the as-cast particles were broken and distributed along the extrusion/rolling direction. After solution treatment, when the samples quenched in cold water, the Si particles can be detected from the matrix of the samples without homogenization, the relatively low peak hardness during aging treatment probably was caused by the remained Si particles, because the remained Si particles

decreased the solute atoms of Si in the matrix, it has been confirmed that Si atoms can enhance the precipitation during aging treatment. Meanwhile, as shown in Fig. 25, the rod/lath like precipitates formed near the Si particles along the extrusion direction, this indicates that the distribution of the Si atoms in the matrix of the samples is not uniform, as shown in Fig. 46(g), during solution treatment, the Si solute atoms diffused into the aluminum matrix from the Si particles, however, the diffusion process was not finished before quenching, thus, a solute atoms rich zones formed after quenching, there is no doubt that the distribution of precipitates between different regions is different. During aging treatment, more Si can be available in solid solution of the solute atom rich regions, and a region of fine microstructure can appear during aging. At the same time, in the solute atom poor regions, the precipitates are much coarser, which has been confirmed in Fig. 28.

For the samples with homogenization and cooled in the furnace, as shown in Fig. 46(b)-(e), after homogenization, the lath/rod-like precipitates uniformly distribute within the grains, during extrusion/rolling, these lath-shaped precipitates were broken. Although some Si rich particles remained after solution treatment, and some solute atom rich regions may form due to the diffusion, however, the inhomogeneous distribution of precipitates were not be observed in the aged samples of this work, this suggests that the precipitates in the furnace cooled samples are more homogeneous than the No-homogenization samples.

When the samples homogenized at 575 ºC for 2 H and cooled in the air, as shown in Fig. 46(i)-(l), all the Si particles dissolved due to Si atoms diffuse into the matrix from the Si particle. however, the concentration of the solute atoms is still uneven, which has

been observed in Fig. 13, many precipitates formed near the original as-cast particles. After homogenization, there are many solute atom rich regions in the air-cooled samples. When the air-cooled samples subjected to extrusion and rolling, the inhomogeneity is still remained, even after solution treatment, some small regions with low content of solute atoms exist. Thus, during aging treatment, the precipitates in some regions are coarser and the number density is lower due to the fewer nucleation sites.

In addition, as seen from Fig .19 and Fig .20, homogenization can affect the grain size after extrusion and solution heat treatment, all the excess Si and balance alloys with homogenization air-cooling exhibit the largest grain size, this is due to in the air-cooled samples, there are no large particles for inhibiting the recrystallization and grain growth. For the samples without homogenization, large amounts of as-cast particles remained, the as-cast particles can act as obstacle for the grain growth [64]. For the samples cooled in the furnace, since the cooling rate after homogenization was very slow, the coarse Mg-Si or Si particles formed during cooling.

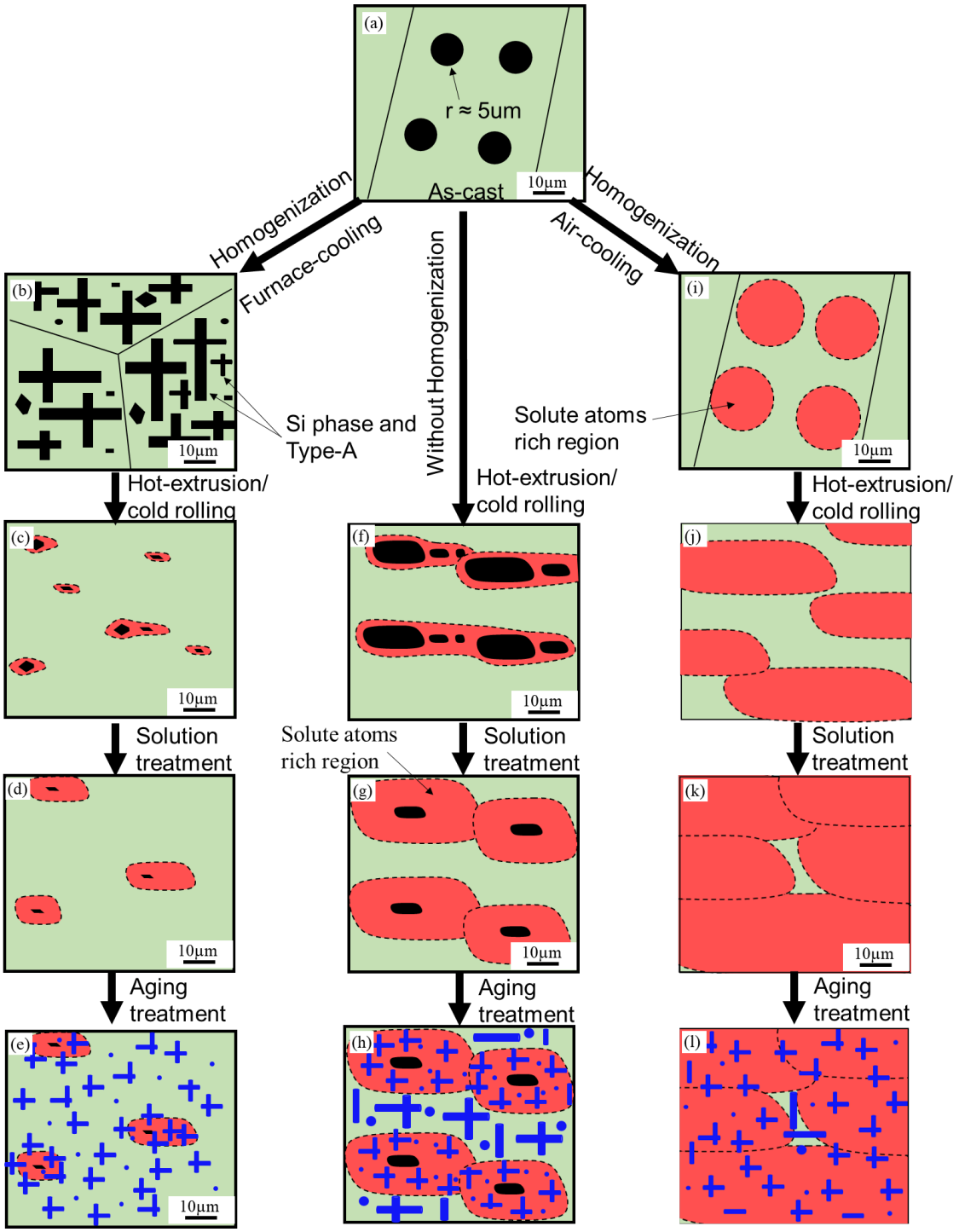

Fig. 46 Schematic illustration of the effect of homogenization on the subsequent processing in the excess Si alloys

4.3 Effect of deformation on microstructure and aging behaviors in Al-Mg-Si and Al-Li-(Cu, Mg) alloys

When the Al-Mg-Si and Al-Li-(Cu, Mg) alloys processed by ASR, the introduced strains were not high enough to form high angles boundaries, as shown in Fig. 32 and Fig. 38, low angles boundaries and tangled dislocations formed in the matrix.

For the Al-Li-(Cu, Mg) alloys, Ultrafine grains with high angle boundaries formed after HPT as a result of the high ε introduced. As seen in Fig. 39, the average grain size of Al-Li alloys is 210 nm, addition of Cu and Mg enhanced the HPT induced refinement of the microstructure of Al-Li alloy. Cu addition is more effective than Mg in refining the grain size. The average grain size of the Al-Li-Cu and Al-Li-Mg alloy is 120 nm and 150 nm, respectively. The fine grain refinement with the addition of Cu or Mg is owing to the effect of atomic-size and modulus mismatch on the mobility of the dislocations [65]. The presence of Mg or Cu atoms increases the localized stress needed for dislocation motion, thus reduce the dislocation recovery, dynamic recrystallization and grain boundary migration during HPT processing. Cu is more effective than Mg in inhibiting dynamic recovery [66]. This also explains why the Al-Li-Cu alloys always exhibit the highest hardness under different ε. Recently, many studies have confirmed the deformation induced solute segregation at grain boundaries [67-71], for instance, Xu found that Cu atoms segregate at grain boundaries during plastic deformation due to dynamic interaction between Cu atoms with gliding dislocations, segregation of Cu atoms at grain boundaries play a crucial role in stabilizing the nanostructures [67]. Segregation of Mg has also been investigated in Al-Mg alloys [70,71], it shows that the HPT processed Al-Mg alloys exhibit higher strength than the Hall-petch relationship predicts, the enhanced

strength is attributed to segregation of Mg at the grain boundaries, it is concluded that the addition of Mg can amplify the Hall-Petch type GB strengthening. Thus, the Cu and Mg addition influences SPD-processed materials not only through a more enhanced grain refinement but also through grain boundary segregation of Cu and Mg atoms.

For the ASR samples, recrystallized grains and dislocation cell size of the Cu and Mg added alloys was also smaller than the Al-Li alloy. These boundaries are less effectively in promoting grain boundary strengthening, because low angle boundaries are weaker obstacles for dislocation movements [72].

Aging treatment after deformation can increase the hardness of the as-deformed Al-Mg-Si and Al-Li-(Cu, Mg) alloys, however, for the Al-Mg-Si alloys, the increase of hardness is lower than that in Al-Li-(Cu, Mg) alloys. Take ASR as an example, when aged at the same temperature (200 ^{o}C), under the similar equivalent strains, the hardness increase for Al-Mg-Si alloy is 14 HV, however, for the Al-Li alloy, the hardness increase is 37 HV, there are two reasons: (1) the overaged precipitates in Al-Mg-Si alloys can easily nucleate on the dislocations during aging treatment, while the dislocations enhances the nucleation and precipitation of the strengthening phase of δ' in the Al-Li alloys; (2) the content of the solute atoms in Al-Mg-Si alloys is lower than that in Al-Li-(Cu, Mg) alloys.

For the Al-Li-(Cu, Mg) alloys, in comparison to the Al-Li alloy, the average size of the δ' phase in Al-Li-Mg alloys was always larger than the Al-Li alloy from as-quenched state, as shown in Table 4. However, the number density of the Al-Li-Mg alloy was lower, it suggested that Mg addition increases the average size of the δ' phase from as-quenched state as compared to binary Al-Li alloy. In spite of the initial hardness of Mg added alloy

was higher than the Al-Li alloy, the two alloys exhibited a similar peak hardness when aged at 200 °C, as seen in Fig. 36. These results indicated that the precipitation of the incoherent S_1 phase combined with the formation of δ'-PFZs leads to material softening in the Al-Li-Mg alloy. With the addition of Cu, except the δ' phase, the T_1 and θ' phase also formed in the matrix, especially the T_1 phase, which orientation relationship with the matrix is $\{0001\}_{T1}//\{111\}_{Al}$ and $<1010>_{T1}//<110>_{Al}$ [73]. It impedes the dislocation glide along the $\{111\}_{Al}$ plane and therefore contribute more to strengthening than precipitates like δ' and θ' phase [74]. This is the reason that the ΔHV of the Al-Li-Cu alloy was higher than the Al-Li and Al-Li-Mg alloys.

As seen in Table 4, with increasing the ε, the average size of the δ' phase decreased under the peak-aged condition. For the Al-Li and Al-Li-Mg alloys after CR and ASR, the hardness increase of the Al-Li and Al-Li-Mg alloys resulted from the precipitation and growth of δ' phase. As shown in Fig. 37(a), the CR processed samples exhibited a higher initial age-hardening rate than the as-quenched samples, indicating that the presence of dislocations facilitated the growth of δ' phase [75]. When the $\varepsilon < 2$, the age-hardenability of the Al-Li alloy was always higher than the Al-Li-Mg alloy, however, under the SPD condition ($\varepsilon > 30$), the Al-Li alloy lost the age-hardenability, even the alloy was aged at 70 °C, the highest hardness increment was only 2.6 HV, as shown in Fig. 35. The similar results were also reported in the reference [76], the Al-0.7wt%Li and Al-1.6wt%Li alloys were processed by hydrostatic extrusion (HE) and equal channel angular extrusion (ECAP), even the as-deformed alloys annealed at the lowest temperature (70 °C), the hardness decreased due to recovery. As shown in Fig. 44, compare to Al-Li-Cu and Al-Li-Mg alloys, there was a small increase in the average grain size of the Al-Li alloy when aged at 150 °C for 0.48 ks. Apparently, the precipitation and growth of δ' phase cannot

compensate the reduced grain boundary and dislocation strengthening in the Al-Li alloy. The grain growth of the HPT processed Cu and Mg added alloys was suppressed during aging. It is well known that the presence of solute or impurity segregation in grain boundary regions imposes a drag force on the GB and reduces the driven force for grain growth due to the decrease in grain boundary energy [77,78]. The precipitates formed at the grain boundaries during aging can also pin the grain boundaries. Therefore, the grain growth rate of the Cu and Mg added alloys is suppressed. Although the hardness of the HPT processed Al-Li alloy decreased upon aging, with the addition of Cu and Mg, the hardness of the HPT processed samples increased and reached the peak rapidly(0.48 ks). As shown in Fig. 42, the T_1 phase was not found in the grain interior of the peak-aged HPT processed Al-Li-Cu alloy, there is no doubt that the precipitation and growth of δ' phase contributes to the hardness during aging. In addition, the annealing (aging) induced hardening has been confirmed in Al-Cu and Al-Mg alloys after SPD [79,80], it was shown that the hardening of ECAP processed Al-5wt%Cu alloy was due to aging-induced relaxation of non-equilibrium HAGBs with enhanced grain boundary segregations of Cu. In the present work, this may also contribute to increase the hardness in the initial stage of aging.

Above all, through combination of deformation and aging treatment, hardness of all the alloys were improved except HPT processed Al-Li alloy. It is suggested that concurrent strengthening by grain refinement and precipitation hardening is hardly activated in the binary Al-Li alloy. Severe plastic deformation will make the binary Al-Li alloy lose age-hardenability, the combination of ASR with medium ε and aging treatment is better for strengthening the binary Al-Li alloy. However, according to Fig. 34, with the addition of Mg or Cu, since the peak-aged hardness increases with increasing the ε before

reaching the stead-state, a highly introduced ε is helpful to strengthen the alloys. Moreover, for the Al-Li-Cu alloy, a lowly introduced ε effectively increased the peak-hardness as compare to the Al-Li-Mg alloy, due to dislocation enhances the precipitation of T_1 phase [81], however, in the case of ASR, the hardness increase between ASR and CR samples was smaller than that in Al-Li-Mg alloy. As shown in Fig. 41(h), T_1 phase coarsened at the low angle boundaries, this suggests that the introduced ε during deformation should avoid forming low angle boundaries, coarsening of T_1 phase along the low angle boundaries may affect the properties of Al-Li-Cu alloy [82,83].

5. Conclusions

The present work investigated the effect of different processes on the microstructure and precipitation in age-hardenable Al-Mg-Si and Al-Li-(Cu, Mg) alloys. The major findings and contributions have been summarized as follows:

(1) Homogenization at 575°C for 2H can remove the as-cast particles in the Al-0.31Mg-0.68Si wt.% and Al-0.64Mg-0.32Si wt.% alloys. During homogenization furnace-cooling (20 °C/H), for the Al-0.31Mg-0.68Si wt.% alloy, predominately the rod/lath-like precipitates formed in the matrix are Si phase and Type-A, most of the Si phases exhibit a lath shaped morphology. For the Al-0.64Mg-0.32Si wt.% alloy, in addition to the homogeneous precipitation of the Mg_2Si phase, heterogeneous precipitation of the β′ and β′/Type-B precipitates was observed along the dislocations.

(2) During homogenization air-cooling (830 °C/H), few precipitates can be observed in both of the Al-0.31Mg-0.68Si wt.% and Al-0.64Mg-0.32Si wt.% alloys, however, many “boundaries” formed inside the grains due to the heterogeneous nucleation of precipitates on the dislocations. Among the “boundaries”, the rod-like precipitates

only lying along $[100]_{Al}$ and $[010]_{Al}$ directions was observed, also the precipitates along three equivalent $<100>_{Al}$ directions were also confirmed. At the same time, as the temperature decreases during cooling, the rod-like precipitates nucleated on the dislocations are lined up and parallel to each other. The over-aged precipitates together with the string-like precipitates, were observed along the dislocations in the homogenization air-cooled samples.

(3) Homogenization can affect the grain size after hot extrusion, the grain size is more smaller and uniform in the samples without homogenization due to the presence of as-cast particles. However, in the excess Si alloys without homogenization, the heterogeneous distribution of the Mg-Si and Si particles were confirmed.

(4) Homogenization affects the grain size and solute atoms distribution after solution treatment. The homogenization air-cooled samples always exhibiting the biggest grain size after solution treatment, regardless of the alloy composition. For the excess Si alloy without homogenization, solution treatment at 575^{o}C for 1H cannot dissolve all the Si particles, the concentration of Si atoms near the Si particles along the extrusion/rolling direction is higher than the other areas.

(5) Processed by ASR, the dislocation cells and recrystallized grains formed in balanced Al-Mg-Si alloy with a thickness reduction of 80%, during aging treatment, the deformed alloy shows accelerated precipitation kinetics in comparison to the undeformed counterpart. When the ASR processed samples at 200^{o}C for 16min, most of the precipitates formed along the low angle grain boundaries, string-like precipitates also were observed along the dislocations within the grains.

(6) For the HPT, ASR and CR processed Al-Li-(Cu, Mg) alloys under different equivalent strains, addition of Mg or Cu increases the as-deformed microhardness of the Al-Li

alloys. Cu is more effective than Mg for increasing the as-deformed hardness. In the case of the ASR, the microstructure after deformation formed the dislocation cell (or tangled dislocation) and recrystallized grains. After processed by HPT, an ultrafine-grained structure with a grain size of 210nm, 120nm and 150nm was achieved in the Al-Li, Al-Li-Cu and Al-Li-Mg alloys, respectively. Addition of Cu or Mg enhances the grain refinement and suppresses the grain growth of the ultrafine Al-Li alloys during aging.

(7) With different amount of introduced ε, aging times for reaching peak aging are different. Higher ε causes shorter time for reaching peak aging. For the Al-Li alloy, severe plastic deformation ($\varepsilon > 30$) made it lose age-hardenability, however, the aging of the asymmetric rolled Al-Li alloys increased the hardness further and the highest hardness was obtained in this alloy. With the addition of Cu or Mg, the as-deformed hardness can be further increased by aging treatment, regardless of the strains. During aging treatment, the peak hardness increases with increasing the equivalent strains.

(8) In the Al-Li-Mg alloy, S_1 phase appeared in the peak-aged condition of preciously non-deformed samples. In the Al-Li-Cu alloy, T_1 phase formed in the grain interior of peak-aged ASR, CR and undeformed samples. Coarsening of T_1 phase was also confirmed along the low angle boundaries in the ASR processed samples. However, T_1 phase was not found in the grain interior of peak-aged HPT samples.

6. References

1. Polmear, I.J. Light Alloys from Traditional Alloys to Nanocrystals, 4th ed.; Elsevier Butterworth-Heinemann:Amsterdam, The Netherlands, 2006; ISBN 0750663715.
2. B. Milkereit, M.J. Starink, P. A. Rometsch, C. Schick, O. Kessler, Review of the Quench Sensitivity of Aluminium Alloys: Analysis of the Kinetics and Nature of Quench-Induced Precipitation, Materials, 12 (2019) 4083.
3. Hornbogen, E. Hundred years of precipitation hardening. J. Light Met. 2001, 1, 127–132.
4. Neikov OD, Naboychenko S, Gopienko VG, Frishberg IV, Lotsko DV (2009) Handbook of non-ferrous metal powders: technology and applications. Elsevier, Amsterdam.
5. Wanhill, R.J.H. Aerospace applications of aluminum-lithium alloys. In Aluminum-Lithium Alloys, Processing, Properties and Applications; Prasad, N.E., Gokhale, A.A., Wanhill, R.J.H., Eds.; Butterworth-Heinemann, Elsevier Inc.: Oxford, UK.
6. A. Serizawa, S. Hirosawa, T. Sato, Three-dimensional atom probe characterization of nanocluster responsible for multistep aging behavior of an Al-Mg-Si alloy, Met. Mater. Trans. A. 39 (2008) 243-251.
7. K.Matsuda, H. Gamada, K. Fuji, Y. Uetani, T. Sato, A. Kamio, S. Ikeno, High-Resolution electron microscopy on the structure of Guinier-Preston Zones in an Al-1.6Mass Pct Mg_2Si alloy, Metall. Mater. Trans. A. 29 (1998) 1161-1167.
8. C.D. Marioara, S.J. Andersen, J. Jansen, H.W. Zandbergen, Atomic model for GP-zones in a 6082 Al–Mg–Si system, Acta Mater. 2001, 49, 321–328.
9. S.J. Anderson, H.W. Zandbergen, J. Jansen, C. Traeholt, U. Tundal, O. Reiso, The crystal structure of the β″ phase in the Al-Mg-Si alloys, Acta Mater. 46 (1998) 3283-

3298.

10. M.H. Jacobs, The structure of the metastable precipitates formed during aging of an Al-Mg-Si alloy, Philos. Mag. 26 (1972) 1-13.
11. R. Vissers, M.A. van Huis, J. Jansen, H.W. Zandbergen, C.D. Marioara, S.J. Andersen, The crystal structure of the β′ phase in Al–Mg–Si alloys, Acta Mater. 2007, 55, 3815–3823.
12. K. Matsuda, Y. Sakaguchi, Y. Miyata, Y. Uetani, T. Sato, A. Kamio, S. Ikeno, Precipitation sequence of various kinds of metastable phase in Al-1.0mass%Mg_2Si-0.4mass%Si alloy, J Mater Sci. 35 (2000) 179–189.
13. K. Matsuda, S. Tada, S. Ikeno, T. Sato, A. Kamio, Crystal system of rod-shaped precipitates in an Al-1.0mass%Mg_2Si-0.4mass%Si alloy, Scripta Metall. Mater. 32 (1995) 1175-1180.
14. K. Matsuda, T. Kawabata, Y. Uetani, T. Sato, S. Ikeno, High-resolution elemental maps for three directions of Mg_2Si phase in Al-Mg-Si alloy, J Mater Sci. 37 (2002) 3369–3375.
15. C.D. Marioara, S.J. Anderson, A. Birkeland, R. Holmestad, Orientation of silicon particles in a binary Al-Si alloy, J Mater Sci. 43 (2008) 4962–4971.
16. B. Noble, G.E. Thompson, Precipitation characteristics of aluminium-lithium alloys, Met. Sci. J. 5 (1971) 114–120.
17. A. Deschamps, C. Sigli, T. Mourey, F. de Geuser, W. Lefebvre, B. Davo, Experimental and modelling assessment of precipitation kinetics in an Al–Li–Mg alloy, Acta Mater. 60 (2012) 1917-1928.
18. S.F. Baumann, D.B. Williams, A new method for the determination of the precipitate-matrix interfacial energy, Scr. Metall., 18 (1984), pp. 611–616.

19. V.G. Davydov, L.B. Ber, E.Ya. Kaputkin, V.I. Komov, O.G. Ukolova, E.A. Lukina TTP and TTT diagrams for quench sensitivity and ageing of 1424 alloy, Mater. Sci. Eng. A., 280 (2000), 76-82.
20. J. Dutkiewicz, O.Simmich, R.Scholz, R.Ciach, Evolution of precipitates in AlLiCu and AlLiCuSc alloys after age-hardening treatment, Mater. Sci. Eng. A., 234 (1997), 253-257.
21. H. K Hardy, JM. Silcock, J. Inst. Met. 84 (1955–56) 423.
22. O. Reiso, Extrusion of AlMgSi alloys, Mater. Forum. 28 (2004) 32–46.
23. Zhu H, Couper MJ, Dahle AK, Effect of process variables on Mg-Si particles and extrudability of 6xxx series aluminum extrusions, JOM, 63, (2011), 66–71.
24. B. Milkereit, N. Wanderka, C. Schick, O. Kessler, continuous cooling precipitation diagrams of Al-Mg-Si alloys, Mater. Sci. Eng. A 550 (2012) 87-96.
25. S. Zajac, B. Bengtsson, C. Jonsson, influence of cooling after homogenization and reheating to extrusion on extrudability and final properties of AA6063 and AA6082 alloys, Materials science forum. 396-402 (2002) 399-404.
26. Y. Birol, Effect of cooling rate on precipitation during homogenization cooling in an excess silicon AlMgSi alloy, Mater. Charact. 73 (2012) 37-42.
27. Y. Birol, The effect of homogenization practice on the microstructure of AA6063 billets, J. Mater. Process. Technol. 148 (2004) 250–258.
28. Y. Birol, Effect of cooling rate on precipitation during homogenization cooling in an excess silicon AlMgSi alloy, Mater. Charact. 73 (2012) 37–42.
29. Q. Du, L. Jia, K. Tang, B. Holmedal, Modelling and experimental validation of microstructure evolution during the cooling stage of homogenization heat treatment of Al–Mg–Si alloys, Materialia. 4 (2018) 70–80.

30. Y. Ito, Z. Horita, Microstructural evolution in pure aluminum processed by high-pressure torsion, Mater. Sci. Eng. A 503 (2009) 32-36.
31. K. Matsuda, H. Gamada, Y. Uetani, S. Rengakuji, F. Shinagawa, S. Ikeno, Specific precipitates in Al-Mg2Si alloys aged after deformation, J. J. I. L. M, 48 (1998) 471-475. https://doi.org/10.2464/jilm.48.471.
32. K. Matsuda, S. Shimizu, H. Gamada, Y. Uetani, F. Shinagawa, S. Ikeno, Effect of deformation on the precipitates in Al-Mg2Si alloys containing silicon in excess, J. Soc. Mater. Sci. 48 (1999) 10-15.
33. R.S. Yassar, D.P. Field, H. Weiland, The effect of predeformation on the β″ and β′ precipitates and the role of Q′ phase in an Al–Mg–Si alloy; AA6022, Scripta Mater., 53 (2005), 299-303
34. K. Teichmann, C.D. Marioara, S.J. Andersen, K. Marthinsem, The effect of preaging deformation on the precipitation behavior of an Al-Mg-Si alloy, Metall. Mater. Trans. A. 43 (2012) 4006-4014.
35. Y.X. Lai, W. Fan, M.J. Yin, C.L. Wu, J.H. Chen, Structures and formation mechanisms of dislocation-induced precipitates in relation to the age-hardening responses of Al-Mg-Si alloys, J. Mater. Process. Technol. 41 (2020) 127-138.
36. S. Hirosawa, T. Hamaoka, Z. Horita, S. Lee, K. Matsuda, D. Terada, Methods for designing concurrently strengthened severely deformed Age-hardenable Aluminum alloys by ultrafine-grained and precipitation hardenings, Metallurgical and Materials Transactions A, 44A (2013) 3921-3933.
37. B. Adamczyk, J. Mizera, K. J. Kurzydlowski, thermal stability of model Al-Li alloys after severe plastic deformation-effect of the solute Li atoms, Mater. Sci. Eng. A. 527 (2010) 4716-4722.

38. J.M. Howe, J. Lee, A.K. Vasudévan, Structure and deformation behavior of T1 precipitate plates in an Al–2Li–1Cu alloy, Metall. Trans. A, 19A (1988), 2911-2920.
39. S. Lee, Z. Horita, S. Hirosawa, K. Matsuda, Age-hardening of an Al–Li–Cu–Mg alloy (2091) processed by high-pressure torsion, Mater. Sci. Eng. A. 546 (2012) 82-89.
40. S. A. E. Buxton, S. C. Browning, Turn-Up and Turn-Down in Hot Rolling: A Study on a Model Mill Using Plasticine, J. Mech. Eng. Sci. 14 (1972) 245-254.
41. P. Fajfar, A. Š. Lah, J. Kraner, G. Kugler, Asymmetric rolling process, Materials and Geoenvironment, Vol. 64 (2017) 151-159.
42. P.W. Bridgman, Effects of high shearing stress combined with high hydrostatic pressure, Phys. Rev. 48 (1935) 825-847.
43. R.Z. Valiev, O.A. Kaibyshev, R.I. Kuznetsov, R.S. Musalimov, N.K. Tsenev, Low-temperature superplasticity of metallic materials, Dokl. Akad. Nauk. SSSR 301 (1988) 864-866.
44. K. Edalati, Z. Horita, A review on high-pressure torsion (HPT) from 1935 to 1988 Mater. Sci. Eng. A, 652 (2016) 325-352.
45. S. Lee, K. Edalati, Z. Horita, Microstructures and Mechanical Properties of Pure V and MoProcessed by High-Pressure Torsion, Mater. Trans. 51 (2010) 1072-1079.
46. S. Lee, Z. Horita, High-Pressure Torsion for Pure Chromium and Niobium, Mater. Trans. 53 (2012) 38-45.
47. Q. Wei, H.T. Zhang, B.E. Schuster, K.T. Ramesh, R.Z. Valiev, L.J. Kecskes, R.J. Dowding, L. Magness, K. Cho, Microstructure and mechanical properties of super-strong nanocrystalline tungsten processed by high-pressure torsion, Acta Mater. 54 (2006) 4079-4089.
48. R.Z. Valiev, R.S. Mishra, J. Groza, A.K. Mukherjee, Processing of nanostructured

nickel by severe plastic deformation consolidation of ball-milled powder, Scripta Mater. 34 (1996) 1443-1448.

49. K. Edalati, Z. Horita, Application of high-pressure torsion for consolidation of ceramic powders, Scripta Mater. 63 (2010) 174-177.
50. J. Sort, D.C. Ile, A.P. Zhilyaev, A. Concustell, T. Czeppe, M. Stoica, S. Surinach, J. Eckert, M.D. Baro, Cold-consolidation of ball-milled Fe-based amorphous ribbons by high pressure torsion, Scripta Mater. 50 (2004) 1221-1225.
51. S.B. Kang, B.K. Min, H.W. Kim, D.S. Wilkinson, J. Kang, Effect of asymmetric rolling on the texture and mechanical properties of AA6111-aluminum sheet, Metall. Mater. Trans. A. 36 (2005) 3141-3149.
52. J. Sidor, A. Miroux, R. Petrov, L. Kestens, Microstructural and crystallographic aspects of conventional and asymmetric rolling processes, Acta Mater. 56 (2008).
53. B.B. Straumal, O. Kogtenkova, Acta Mater. 56 (2008) 925-933.
54. B.B. Straumal, O. Kogtenkova, A.B. Straumal, Yu.O. Kunchyeyev, B. Baretzky, J Mater Sci. 45 (2010) 4271-4275.
55. B.B. Straumal, B.S. Bokshtein, A.B. Straumal, A.L. Petelin, JETP Letters. 88 (2008) 537-542.
56. S.J. Andersen, C.D. Marioara, A. Frøseth, R. Vissers, The structural relation between precipitates in Al–Mg–Si alloys, the Al-matrix and diamond silicon, with emphasis on the trigonal phase U1-MgAl2Si2, Mater. Sci. Eng. A, 444 (2007), 157-169.
57. C.D. Marioara, H. Nordmark, S.J. Andersen, R. Holmestad, Post-β″ phases and their influence on microstructure and hardness in 6xxx Al-Mg-Si alloys, J. Mater. Sci., 41 (2006), 471-478.
58. K. Matsuda, S. Ikeno, H. Matsui, T. Sato, K. Terayama, Y. Uetani, Comparison of

precipitates between excess Si-type and balanced-type Al-Mg-Si alloys during continuous heating, Metall. Mater. Trans. A, 36A (2005), 2007-2012.

59. S.J. Andersen, C.D. Marioara, A. Frøseth, R. Vissers, H.W. Zandbergen, Crystal structure of the orthorhombic U2-Al4Mg4Si4 precipitate in the Al–Mg–Si alloy system and its relation to the β′ and β″ phases, Mater. Sci. Eng. A., 390 (2005), 127-138
60. K. Teichmann, C.D. Marioara, S.J. Andersen, K. Marthinsem, The Effect of Preaging Deformation on the Precipitation Behavior of an Al-Mg-Si Alloy, Metall. Mater. Trans. A. **43** (2012) 4006-4014.
61. M. Kolar, K.O. Pedersen, S.G. Dahl, K. Teichmann, K. Marthinsen: Mater. Trans. **52** (2011) 1356-1362.
62. T. Ogura, K. Horikawa, Y. Kitani, M. Miara, S. Kim, E. Kobayashi, T. Sato, H. Kobayashi: Mater. Trans. **57** (2016) 1282-1286.
63. Weatherly GC, Perovic A, Mukhopadhyay NK, Lloyd DJ, Perovic DD (2001) The precipitation of the Q phase in an AA6111 alloy, Metall. Mater. Trans. A 32: 213-218.
64. Y. Lin, H. Wen, Y. Li, B. Wen, W. Liu, E.J. Lavernia, An analytical model for stress-induced grain growth in the presence of both second-phase particles and solute segregation at grain boundaries, Acta Mater., 82 (2015), 304-315.
65. K. Edalati, D. Akama, A. Nishio, S. Lee, Y. Yonenaga, Jorge M. Cubero-Sesin, Z. Horita, Influence of dislocation–solute atom interactions and stacking fault energy on grain size of single-phase alloys after severe plastic deformation using high-pressure torsion, Acta Mater. 69(2014) 68-77.
66. Y. Huang, J.D. Robson, P.B. Prangnell, The formation of nanograin structures and accelerated room-temperature theta precipitation in a severely deformed Al–4 wt.%

Cu alloy, Acta Mater. 58 (2010) 1643-1657.

67. W. Xu, X. C. Liu, X. Y. Li, K. Lu, Deformation induced grain boundary segregation in nanolaminated Al–Cu alloy, Acta Mater., 182 (2020), 207-214.
68. T. Masuda, X. Sauvage, S. Hirosawa, Z. Horita, Achieving highly strengthened Al–Cu–Mg alloy by grain refinement and grain boundary segregation, Mater. Sci. Eng. A., 793 (2020), 139668.
69. S.V. Bobylev, N.A. Enikeev, A.G. Sheinerman, R.Z. Valiev, Strength enhancement induced by grain boundary solute segregations in ultrafine-grained alloys, Int. J. Plast., 123 (2019), 133-144.
70. Y. Liu, M.P. Liu, X.F. Chen, Y. Cao, H. Roven, M. Murashkin, R.Z. Valief, H. Zhou, Effect of Mg on microstructure and mechanical properties of Al-Mg alloys produced by high pressure torsion, Scr. Mater., 159 (2019), 137-141,
71. R.Z. Valiev, N.A. Enikeev, M.Yu. Murashkin, V.U. Kazykhanov, X. Sauvage, On the origin of the extremely high strength of ultrafine-grained Al alloys produced by severe plastic deformation, Scr. Mater., 63 (2010), 949-952,
72. N.Hansen, Hall-petch relation and boundary strengthening, Scr. Mater., 51 (2004), 801-806.
73. P. Donnadieu, Y. Shao, F. Geuser, G. Botton, S. Lazar, M. Cheynet, M. Boissieu, A. Deschamps, Atomic structure of T_1 precipitates in AL-Li-Cu alloys revised with HAADF -STEM imaging and small-angle X-ray scattering, Acta Mater., 59 (2011), 462-472,
74. S. Zhang, W. Zeng, W. Yang, C. Shi, H. Wang, Ageing response of a Al–Cu–Li 2198 alloy**,** Mater. Des., 63 (2014), 368–374.
75. Z.M. Wang, G.J. Shiflet, Growth of δ' on Dislocations in a Dilute Al-Li Alloy, Metall.

Mater. Trans. A., 29 (1998), 2073-2085.

76. B. Adamczyk, J. Mizera, K. J. Kurzydlowski, Thermal stability of model Al-Li alloys after severe plastic deformation-effect of the solute Li atoms, Mater. Sci. Eng. A., 527 (2010), 4716-4722.
77. C. C. Koch, A R. O. Scattergood, K. A. Darling, J. E. Semones, Stabilization of nanocrystalline grain sizes by solute additions, J Mater Sci., 43 (2008), 7264–7272.
78. J. Li, J. Wang, G. Yang, On the stagnation of grain growth in nanocrystalline materials, Scr. Mater., 6 (2009), 945-948.
79. H. Jia, R. Bjorge, L. Cao, H. Song, K. Marthinsen, Y. Li, Quantifying the grain boundary segregation strengthening induced by Post-ECAP aging in an Al-5Cu alloy, Acta Mater., 155 (2018), 199-213.
80. R.Z.Valiev, F.Chmelik, F.Bordeaux, G.Kapelski, B.Baudelet, The Hall-Petch relation in submicro-grained Al-1.5% Mg alloy, Scr. Metall. Mater., 27 (1992), 855-860.
81. Noble B, Thompson GE, T_1 (Al_2CuLi) precipitation in aluminum–copper–lithium alloys, Met Sci., 6 (1972), 167–174.
82. N. Nayan, S. Murty, A. Jha, B. Pant, S.C. Sharma, K. George, G. Sastry, Processing and characterization of Al–Cu–Li alloy AA2195 undergoing scale up production through the vacuum induction melting technique, Mater. Sci. Eng. A., 576 (2013), 21–28.
83. Y. Yan, L. Peguet, O. Gharbi, A. Deschamps, C. R. Hutchinson, S.K. Kairy, N. Birbilis, On the corrosion, electrochemistry and microstructure of Al–Cu–Li alloy AA2050 as a function of ageing, Materialia, 1 (2018), 25–36.

7. Acknowledgements

Upon the completion of the thesis, I would like to take this opportunity to express my sincerely gratitude to my supervisor, Prof. Kenji Matsuda, who has given me important guidance on the thesis. Without his guidance and suggestions, my thesis would have been impossible. I am grateful to Assoc. Prof. Seungwon Lee and Dr. Taiki Tsuchiya for their support and insightful comments. They helped me to make necessary preparations about equipment and critical comments for improving thesis quality. They resolved most of the critical situation during my work.

Beside, I would like to thank Mr. Yasutaka Kuroda, Mr. Tatsuya Hiragi, Mr. Bendo Artenis, Mr. Uhei Haizuka, Mr. Yosuke Hasaigawa and all my lab-mate, who helped me a lot in the experiment or throughout the difficult times. I would also like to thank the staffs of Department of Materials Design and Engineering, Graduate School of Science and Engineering for Research, University of Toyama for supporting about technique and equipment for this study.

Last but not least, I would like to express my gratitude to all the friends and family members who have offered me help. Without their help, I could not have finished my study.